UNIVERSITY OF OKLAHOMA

GRADUATE COLLEGE

CARBON-WATER COUPLING OF TERRESTRIAL ECOSYSTEMS IN RESPONSE TO CLIMATE CHANGE AND CLIMATE VARIABILITY

A DISSERTATION

SUBMITTED TO THE GRADUATE FACULTY

in partial fulfillment of the requirements for the

Degree of

DOCTOR OF PHILOSOPHY

By

LING DU
Norman, Oklahoma
2019

CARBON-WATER COUPLING OF TERRESTRIAL ECOSYSTEMS IN RESPONSE TO CLIMATE CHANGE AND CLIMATE VARIABILITY

A DISSERTATION APPROVED FOR THE
DEPARTMENT OF MICROBIOLOGY AND PLANT BIOLOGY

BY

Dr. Xiangming Xiao, Chair

Dr. Michael Richman

Dr. Heather McCarthy

Dr. Lara Souza

Dr. Jean Steiner

This dissertation is dedicated to my families for their unconditional love and support, to my advisors for their guide and corporation, and to the efforts I have put in past years.

Acknowledgements

I really appreciate my current advisor, Prof. Xiangming Xiao, who let me study in EOMF Lab and provided me support to complete my study in last two years. I appreciate the space and trust he gave to me. Without his continuous instruction and support, it is impossible for me to finish my research on time.

I also would like to express my gratitude to Prof. Yiqi Luo, who supported and guided me in Ecolab in the first two years. He is the person who opened the door of terrestrial ecology for me. I admire his academic achievements in our community.

I would also like to thank the other members in my doctoral committee, Prof. Michael Richman, Prof. Heather McCarthy, Prof. Jean Steiner, and Prof. Lara Souza for their substantial instructions in my research and kindness showered over me in daily working interactions.

I would like to thank the crew in EOMF and Ecolab for their company and help in last four years. I really enjoy the time we hang out for dinner, and discuss research questions freely.

I would express my heartfelt thanks to my beloved families for their consistent loving and trust all through these years. I love and miss them all the time.

Last, I acknowledge research grants for the support to my Ph.D. study and appreciate the staffs from Department of Microbiology and Plant Biology and Center for Spatial Analysis for their assistance.

Table of Contents

List of Figures

List of Tables

Abstract

Carbon and water cycles are two fundamental biophysical processes in terrestrial ecosystems. Rain use efficiency (RUE), defined as the ratio of ecosystem productivity to precipitation (PPT), and water use efficiency (WUE), defined as the ratio of ecosystem productivity to evapotranspiration (ET), are critical metrics of ecosystem function linking ecosystem carbon and water cycles. Under the context of global climate change and climate variability, much attention has been paid to the variation in RUE or WUE across biomes or species, and its responses to drought, elevated atmospheric CO_2 concentration, and other environmental changes. However, due to differences in research method, study areas, and complexity in definitions, there is a lack of consensus on the coupling of carbon and water fluxes across different ecosystems and it's responses to climate change and climate variability.

Chapter 1 reviews the current status of carbon-water coupling studies and raises the major scientific questions that will be addressed in the dissertation.

Chapter 2 examined the spatiotemporal variations in coupling of gross primary production (GPP) to PPT, and water fluxes (ET and T (transpiration)) at site and global scales. In-situ climate, and carbon and water fluxes datasets from 111 FLUXNET sites, global climate data, and remote sensing based GPP and ET data were combined to explore the relationships of GPP to PPT, ET, and T across different ecosystems and under different hydroclimatic conditions. Generally, GPP had a saturating relationship with PPT, and was linearly coupled with ET and T. This strong carbon-water flux coupling could be further improved by the incorporation of vapor pressure deficit (VPD) at site level. The sensitivity of GPP to PPT increased in severe drought years and decreased in

pluvial years. There was no obvious change in the sensitivity of GPP to ET or T under altered climate conditions.

Chapter 3 identified extreme drought events globally based on rain-use efficiency [RUE; GPP/PPT]. Ecosystem RUE is expected to increase with decreasing precipitation to a maximum (RUE_{max}) during moderate drought and will likely decline when water shortage is beyond the tolerance of vegetation, leading to a loss of ecosystem function. In this chapter, the PPT at the RUE_{max} was identified as a threshold of extreme drought condition, and the deviation of the RUE in drought condition from the norms in non-drought condition was further tested to determine if it exceeds the normal variability. Well-known extreme drought events were detected, e.g. 2003 drought in Europe, 2002 and 2011 drought in the U.S., and 2010 drought in Russia. Moreover, the reduced carbon uptake caused by extreme droughts (0.14±0.03 PgC/yr) could explain >70% of the GPP anomaly in drought-affected areas.

Chapter 4 investigated the responses of WUE to environmental change in forests and grasslands in Northern Hemisphere. On the basis of Chapter 1, underlying water use efficiency (UWUE; $GPP \times VPD^{0.5}/ET$) incorporated the VPD effects on carbon assimilation and transpiration and hence provided an optimal indicator of carbon-water coupling in flux tower dataset. In this chapter, the interannual trend in UWUE and its responses to environmental factors were analyzed across 11 evergreen needleleaf forest (ENF) sites, 7 deciduous broadleaf forest (DBF) sites, and 9 grassland (GRA) sites. Results showed that, there was an obvious increase in UWUE in forests which was triggered by CO_2 fertilization, increasing VPD, as well as the decreasing soil moisture in DBF. In GRA, the positive effect of CO_2 fertilization on UWUE was offset by the

negative effect of increasing soil moisture on UWUE, leading to no obvious trend in UWUE.

Chapter 5 estimated the global ET at 8-day, 0.05° resolution from 2003 to 2015 based on GPP from Vegetation Photosynthesis Model (VPM), VPD estimated from Atmospheric Infrared Sounder (AIRS), and biome-level UWUE parameters. Biome-level UWUE was derived from the FLUXNET2015 dataset at 8-day timescale. The ET was calibrated and validated at the biome level against flux tower ET. The interannual trends in ET, GPP, and VPD were also analyzed at the global scale. There was an increasing trend in global ET over the study period (1.47 mm/yr). This ET product on the basis of carbon-water coupling showed better performance than a traditional approach, i.e. Penman-Monteith equation.

Chapter 6 briefly summarizes the conclusions and perspectives from this dissertation.

Chapter 1: Introduction

1.1 Research background

Two main cycles of an ecosystem are the carbon cycle and the water cycle. In terrestrial ecosystems, gross primary productivity (GPP), the total vegetation photosynthesis, is the first step of carbon input from the atmosphere to the biosphere (Figure 1.1). Overall, more than half of GPP is respired, while the rest part is kept in the ecosystem (Chapin et al. 2011). In past years, terrestrial ecosystems have absorbed more than 30% of anthropogenic CO_2 emissions (Le Quéré et al. 2015). Water is the limiting factor that strongly constrains the productivity of the plants in most ecosystems and plays a central role in the dynamics of ecosystem carbon cycle (Seddon et al. 2016). The water cycle of an ecosystem usually begins with precipitation (PPT). PPT can be transpired to the atmosphere by plants, evaporated directly back to the atmosphere from soil surface and canopy interception, or lost as runoff and percolation to groundwater (Figure 1.1). For most vegetated terrestrial ecosystems, the total evapotranspiration (ET) is dominated by plant transpiration (T), varying from ~50% in shrublands and deserts to ~70% in tropical forests (Zhou et al. 2016). Ecosystem carbon and water cycles are both influenced by the physiological processes affecting plant photosynthesis and the physical processes affecting water loss from the ecosystem.

Since pre-industrial times, the atmospheric CO_2 concentration increased from ~290 ppm to 400 ppm by 2015 and continues to increase (Keenan et al. 2016; Stocker et al. 2013). As a result of increase in greenhouse gases, the globally averaged temperature increased by 0.85 ℃ over the period of 1880~2012 (Stocker et al. 2013). In addition, the precipitation variability is likely becoming larger than ever, leading to more and more

extreme climate events (Allen et al. 2010; Mazdiyasni and AghaKouchak 2015; Stocker et al. 2013). Since the middle of 20th century, the frequency and intensity of heatwaves and droughts have substantially increased. The number of drought occurrences has almost doubled in Europe, Australia and most regions of Asia (Donat et al. 2013). Recent large-scale extreme droughts have occurred in Europe in 2003 (Ciais et al. 2005), central North America around 2002 and 2011 (Breshears et al. 2005; Du et al. 2018), and Amazon in 2005 and 2010 (Doughty et al. 2015). A wide range of ecosystem responses to these extreme droughts have been reported, from little change to major reductions in ecosystem productivity (Ciais et al. 2005; Jentsch et al. 2011; Schwalm et al. 2012; Zhao and Running 2010). On the other hand, in response to the increasing CO_2 concentration in the atmosphere and other influences from climate change, nitrogen deposition, and land cover change, 25%~ 50% of the global vegetated area showed a greening trend caused by enhanced photosynthesis and lengthened growing season, which can increase the carbon sequestration of terrestrial ecosystems (Zhu et al. 2016). Thus, investigating the responses of carbon-water coupling to climate and environmental factors would help us understand future responses of terrestrial carbon and water budgets to climate change and climate variability.

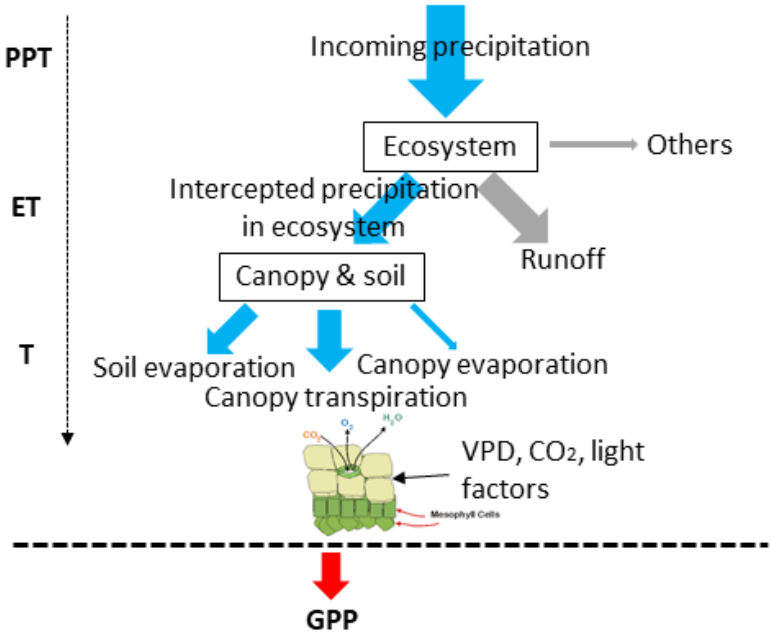

Figure 1.1 Conceptual representation of ecosystem gross primary production (GPP), precipitation (PPT), and water flux components [evapotranspiration (ET) and transpiration (T)] in an ecosystem.

Normally, ecosystems with certain plant communities are adapted to prevailing water conditions, which implies a balance between carbon gain and water availability (Chapin et al. 2011). Two indicators have been widely utilized to describe this tradeoff between carbon uptake and water loss (or water needed) in ecosystems. Rain-use efficiency (RUE, $gC/m^2/mm$), usually defined as the amount of primary productivity per unit of PPT, provides a useful index of the interactions between vegetation and PPT, thus the potential tradeoffs between ecosystem's carbon gain and water use (Hu et al. 2008). RUE was found to increase with decreasing mean annual PPT and Huxman et al. (2004) and Bai et al. (2008) reported a common maximum RUE in dry years across different biomes. However, subsequent studies also found that the maximum RUE varied across sites (Zhongmin et al. 2010). Water-use efficiency (WUE, $gC/kg\ H_2O$), defined as the amount of carbon gained per unit of ET or T, quantifies the tradeoff between carbon gain

and water loss through plant stomatal and provides insight into the ecological functioning of the vegetated land surface (Niu et al. 2011). A large number of studies have concentrated on the impacts of droughts and CO_2 fertilization on WUE at leaf, canopy, and ecosystem scales (Keenan et al. 2013; Knauer et al. 2017; Yang et al. 2016). Generally, WUE has been found through site-level analysis or model simulation to increase with elevated atmospheric CO_2 concentration and during drought (Cheng et al. 2017; Keenan et al. 2013; Peters et al. 2018). However, there are still inconsistent findings on the magnitude of CO_2 and drought impacts on WUE. Additionally, the definition of WUE was developed in several formulations aiming to obtain a stable variable from leaf to ecosystem spatial scale and from short term (i.e. diurnal) to annual temporal scale by considering the effect of VPD on carbon assimilation and transpiration (Beer et al. 2009; Zhou et al. 2014). However, these new formulations have not been broadly evaluated. Thus, the spatiotemporal variation in RUE or WUE and its responses to climate change are still not quantified well.

Great advances have been made in last decades in quantifying and understanding the patterns of terrestrial productivity and hydrological condition with ground and remote sensing observations. Satellite remote sensing provides an opportunity to monitor changes in vegetation cover at regional and global scales, and therefore has provided the capability to observe the long-term responses of critical ecosystem function to climate and environmental change. Currently, global GPP and ET can be obtained from remote sensing estimation (e.g. MODIS and VPM) (Zhang et al. 2017; Zhao and Running 2010), upscaling approaches based on FLUXNET observations (e.g. MPI-BGC) (Jung et al. 2011), or process-based models (e.g. BESS and TRENDY) (Jiang and Ryu 2016; Sitch

et al. 2008). Additionally, satellite measurement of Solar-Induced Chlorophyll Fluorescence (SIF) opens up a new avenue for monitoring terrestrial GPP from space (Sun et al. 2018). Meanwhile, more than 750 eddy flux tower sites have been established worldwide (i.e. FLUXNET) for measurement of CO_2 and H_2O exchanges between the ecosystem and the atmosphere through the eddy covariance technique (http://fluxnet.fluxdata.org/). These advances allow comprehensive quantification of the coupling between carbon and water cycles in ecosystems from site to global scale.

1.2 Research objectives

The goal of this dissertation is to elucidate the responses of carbon-water coupling to climate change and climate variability at multiple spatial and temporal scales in order to improve our understanding of current and future carbon-water coupling in terrestrial ecosystems.

1.3 Organization of the dissertation

This dissertation has an introduction, four thematic chapters, and a summary. The theme 1 manuscript (Dissertation Chapter 2) is in revision following journal review. The theme 2 paper (Dissertation Chapter 3) has been published in Science of the Total Environment. The theme 3 manuscript (Dissertation Chapter 4), and the theme 4 manuscript (Dissertation Chapter 5) are in preparation for later submission.

Chapter 1 Introduction

Chapter 2 explores the spatiotemporal variations in relationships between GPP and PPT, ET, and T across different biome types and under different hydroclimatic conditions. Both site level datasets (i.e. FLUXNET) and global gridded remote sensing datasets including GOME 2, MODIS, VPM, and GLEAM products were used to quantify

those relationships. The discussion focuses on the spatiotemporal variation in responses of the GPP (or SIF) to PPT and water fluxes across biome types and under different hydroclimatic conditions.

Chapter 3 identifies global extreme drought events based on maximum RUE. As discussed in Chapter 2, ecosystem RUE increases with decreasing PPT to a maximum during moderate drought. RUE is assumed to decline with further water shortage. Based on this hypothesis, this chapter identifies the global patterns of extreme drought events during 2001-2011 and 2001-2015. We further explored the drought impacts on GPP anomaly in those drought-affected regions. The discussion focuses on the drought events identified and its role in carbon dynamics.

Chapter 4 evaluates the responses of the UWUE to different environmental factors in forests and grasslands in the Northern Hemisphere. UWUE has been demonstrated to be an optimal indicator of ecosystem carbon-water coupling and has more physiological relevance, which was also discussed in Chapter 2. However, UWUE responses to environmental dynamics have not been evaluated broadly. This chapter investigated the trend in UWUE, as well as the trends in related environmental factors (i.e. temperature, soil moisture, CO_2, radiation, etc.). The variation in UWUE was further attributed to the changes in environmental factors statistically. The discussion focuses on the trend in UWUE detected across sites and its attribution to environmental factors.

Chapter 5 estimates global ET through GPP and UWUE by combing VPD. This chapter generated 8-day, 0.5° resolution global ET from 2003 to 2015. We first characterized biome-level UWUE from FLUXNET sites measurements and then generated ET at the global scale. The ET estimated in this study was calibrated and

validated against eddy flux measurements and other ET products (i.e. MODIS). We further analyzed the interannual trend in GPP, VPD, and ET. The discussion focuses on model evaluation and trend analysis.

Chapter 6 Summary

1.4 List of Publications from the Dissertation

Chapter 2

L. Du, X. Xiao*, Z. Shi, Y. Zhang, X. Wu, Q. Chang, M.R. Heather, J. Steiner, R.B. Doughty, Z. Zou, J. Wang. Examining the coupling of ecosystem carbon and water cycles at eddy flux sites and the global scale. *Environmental Research Letters*, 2019. (In revision)

Chapter 3

L. Du, N. Mikle, Z. Zou, Y. Huang, L. Jiang, J. Liang, Y. Luo*. Global patterns of extreme drought-induced loss in land primary production: identifying ecological extremes from rain-use efficiency. *Science of the Total Environment*, 2018, 628-629: 611-620.

Chapter 4

L. Du, X. Xiao, Y. Zhang, et al., Response of underlying water use efficiency to environmental change in forests and grasslands in the Northern Hemisphere (In preparation).

Chapter 5

L. Du, X. Xiao, Y. Zhang, et al., Global evapotranspiration over the past decade: estimation based on underlying water use efficiency combined with land primary production (In preparation).

Chapter 2: Examining the coupling of ecosystem carbon and water cycles at eddy flux site and global scales

Abstract

Quantifying the relationship between ecosystem carbon and water cycling is important in forecasting the responses of ecosystem structure and function to climate variability. However, there is a lack of consensus on the spatiotemporal coupling of carbon and water cycles across terrestrial ecosystems and under different hydroclimatic conditions. This study aims to quantify the relationships of annual gross primary production (GPP) and solar-induced chlorophyll fluorescence (SIF) to precipitation (PPT), and water flux components [evapotranspiration (ET), and transpiration (T)] across 111 sites using FLUXNET2015 dataset and at the global scale using global climate datasets from Climatic Research Unit (CRU), global GPP datasets from Vegetation Photosynthesis Model (VPM), global SIF datasets from Global Ozone Monitoring Instrument Experiment-2 (GOME-2), and global ET datasets from Moderate Resolution Imaging Spectroradiometer (MODIS) and Global Land Evaporation Amsterdam Model (GLEAM). We further evaluated the sensitivity of GPP and SIF to PPT and water fluxes under different hydroclimatic conditions characterized by severe drought, normal, and pluvial periods at site and global scales. We found that GPP and SIF had a saturating relationship with PPT, with the highest sensitivity of GPP and SIF to PPT occurring in semi-arid regions with mean PPT around 473.0±170.5 mm/yr. GPP and SIF were linearly coupled with ET and T, and this strong carbon-water coupling was further improved by the incorporation of vapor pressure deficit (VPD) for the flux dataset. The sensitivity of GPP and SIF to PPT increased in severe drought years and decreased in pluvial years.

However, there was no obvious change in the sensitivity of GPP and SIF to ET or T in altered hydroclimatic conditions. This study comprehensively evaluated the coupling of the carbon and water cycles from the site level to the global scale, and improves our understanding of ecosystem carbon and water cycling and its response to climate variability.

2.1 Introduction

Quantifying the relationship between ecosystem carbon and water cycling is essential for better understanding of biological and ecological processes in the context of increasing climate variability (Reichstein et al. 2013; Stocker et al. 2013). Gross primary production (GPP), the total amount of carbon fixed by photosynthesis, is the largest sink of carbon from the atmosphere to the biosphere. It is constrained by precipitation (PPT) in many terrestrial ecosystems, and is fully coupled with ecosystem water fluxes [evapotranspiration (ET) and transpiration (T)] (Figure 1.1) (Chapin et al. 2011; Jung et al. 2017). Carbon and water cycling in terrestrial ecosystems are both controlled by plant physiological features that affect leaf photosynthetic rate and stomatal conductance, and environmental factors that affect water availability, radiation and vapor pressure deficit (VPD), etc.(Meyer 2018; Niu et al. 2011; Zhongmin et al. 2010). Thus, a comprehensive understanding of the coupling of GPP and PPT and water fluxes across terrestrial ecosystems and under different hydroclimatic conditions is of great importance for understanding and forecasting the future responses of ecosystems to climate variability.

The relationship between ecosystem net primary production (NPP; ~half of GPP) and PPT and ET has been widely explored using multi-year, multi-site measurements at local to continental scales (Biederman et al. 2016; Huxman et al. 2004; Ponce Campos et

al. 2013; Wilcox et al. 2017). Across sites, ANPP had a saturating relationship to PPT and its sensitivity or rain-use efficiency (RUE) decreased from dry sites to mesic sites (Huxman et al. 2004). Over multiple years at a given site, ANPP was observed to increase with PPT linearly in normal climate conditions and nonlinearly during extreme climate variability (Hsu and Adler 2014; Knapp et al. 2017). Additionally, ANPP was found to have a linear relationship with ET across sites, suggesting a common ecosystem water-use efficiency (WUE) among biomes (Ponce Campos et al. 2013). By taking the slope of the ANPP~ET relationship as WUE, Ponce Campos et al. (2013) found an increase in WUE in the driest years and a decrease in the wettest years across biomes. However, there is a lack of consensus on the spatiotemporal variations of WUE across biomes and under contrasting hydroclimatic conditions, due to different spatial scales and definitions of WUE (Niu et al. 2011; Peters et al. 2018; Sun et al. 2016; Tang et al. 2014; Yang et al. 2016; Yu et al. 2017). Moreover, there have been some efforts to quantify the relationship between GPP and T (or ET when soil evaporation is small) by also incorporating the effect of VPD on carbon assimilation and transpiration using site-level measurements, which is more plant physiologically relevant (Beer et al. 2009; Zhou et al. 2014). In general, the relationship between GPP×VPD and T is stronger than the GPP~T relationship on daily to annual timescales (Beer et al. 2009), and the relationship between $GPP \times VPD^{0.5}$ and T is even less variable across biomes on a daily timescale (Zhou et al. 2015). However, due to the difficulty in partitioning T from ET, the relationship between GPP and T with VPD has not been broadly evaluated across ecosystems. Even less well-known is the GPP~T relationship under different hydroclimatic conditions. Thus, the

spatiotemporal relationships between GPP and PPT, ET, and T across terrestrial ecosystems and their responses to climate have not been well evaluated.

Substantial advances have been made in the last decade in estimating global patterns of the terrestrial carbon and water cycles using ground and remote sensing observations. More than 750 ground-based flux tower stations (i.e. FLUXNET) have been established worldwide to measure the CO_2 and H_2O exchange between terrestrial ecosystems and the atmosphere (http://fluxnet.fluxdata.org/) (Baldocchi et al. 2001). Also, satellite measurements of optical parameters related to vegetation activity and water content on the Earth's surface make it possible to quantify global GPP and water fluxes over a long period and at high spatial resolution, e.g. VPM (Vegetation Photosynthesis Model) GPP and MODIS (Moderate Resolution Imaging Spectroradiometer) ET (Mu et al. 2011; Zhang et al. 2017). Satellite measurement of solar-induced chlorophyll fluorescence (SIF), energy emitted by vegetation during photosynthesis, opens up another avenue for estimating GPP from space (Sun et al. 2017). Satellite SIF is highly correlated with GPP and has been considered to be the most direct, remotely sensed measure of terrestrial photosynthesis at large spatial scales (Frankenberg et al. 2011; Joiner et al. 2014). The combination of highly accurate, ground-based flux tower measurements and global space-borne remote sensing observations can be used to comprehensively quantify the spatiotemporal coupling of the terrestrial carbon and water cycles.

The objective of this study was to examine the relationships between annual GPP, SIF and PPT, ET, and T across all terrestrial ecosystems and under different hydroclimatic conditions using FLUXNET and global datasets. SIF was used as a proxy of GPP in our study to reduce the uncertainty of using a single global GPP product. We

used monthly site-level data from eddy flux tower sites and monthly global gridded data from remote sensing and climate datasets to generate annual GPP, SIF, PPT, ET, and T datasets (Table 2.1). Annual T was partitioned from ET in the flux and global datasets. In our study, we first characterized the spatiotemporal relationships between GPP, SIF and PPT, and water flux components across sites and the globe. Second, we focused on the temporal variations in sensitivity of GPP and SIF to PPT and water fluxes under severe drought, normal, and pluvial periods at the site and global scales. In our analysis, the sensitivity was represented by the slope of a simple linear regression model between GPP (and SIF) and PPT or water fluxes, which might be slightly different from the estimates of WUE or RUE defined by ratios in previous studies when there is a non-zero y-intercept (Veron et al. 2005).

2.2 Materials and methods

2.2.1 Study area

This study focuses on 111 FLUXNET sites and global vegetated land area (~120 million km^2). Figure S2.1 shows the dominant land cover type map in 2001-2016 based on MODIS land cover product (MCD12C1.006) with 0.5° resolution. The dominant land cover type in a pixel is defined as a land cover occupying more than 70% of the grid cell in each year during the period 2001-2016. Pixels with water proportion > 10% were not used in this study.

2.2.2 In-situ climate, carbon, and water flux datasets

We used 2000-2014 monthly eddy flux data from the FLUXNET 2015 (http://fluxnet.fluxdata.org/data/fluxnet2015-dataset/). Out of 166 sites, we identified 111 eddy covariance flux sites that had >=4 years of measurements (mean of 9 years) (Table

S2.1). The major ecosystem types at these sites were shown in Table S2.1. Monthly GPP, PPT, and latent heat flux (LE) data were used to generate annual GPP, PPT, ET, and T for each site. Monthly ET was converted from LE (w/m^2) using the method in Tang et al. (2014). Monthly T was partitioned from ET using the approach developed by Wei et al. (2017) (see following sections). In addition, monthly VPD measurements were used to evaluate VPD effects on carbon-water coupling at the site scale.

2.2.3 Global climate datasets

We used global gridded climate data from Climatic Research Unit (CRU) TS 4.01 for 1987-2016 (https://crudata.uea.ac.uk/cru/data/hrg/cru_ts_4.01/), including PPT, temperature (TMP), minimum temperature (TMN), and vapor pressure (VAP) at monthly, 0.5° resolution. Monthly PPT was summed annually to estimate annual PPT. The mean ± standard deviation (SD) of annual PPT during 1987-2016 (30 years) was selected as the baseline of hydroclimatic conditions for the beginning of the 21st century for each grid. Severe drought years and pluvial years were defined as years with PPT < mean - SD and PPT > mean + SD, respectively. Using the Magus Equation, monthly TMP, TMN, and VAP were used to calculate monthly VPD, in order to evaluate the VPD effects on carbon-water coupling at the global scale.

2.2.4 Global GPP dataset

The global GPP data came from VPM simulations, which is a light-use efficiency model driven by MODIS vegetation indices, land cover maps, and NCEP Reanalysis II climate data (Xiao et al. 2004; Xiao et al. 2005). VPM GPP is available for 2000-2017 with a 500m, 8-day resolution (Zhang et al. 2017). This GPP product showed a strong spatiotemporal consistency with *in situ* GPP estimates across biomes (Ma et al. 2018;

Zhang et al. 2017). For this study, we aggregated the 8-day, 500m VPM product into monthly GPP at 0.5° resolution for 2001-2016 to match the coarse spatial resolution of the SIF data. Annual total GPP was calculated by summing the monthly totals

2.2.5 Global SIF dataset

We used the latest version (v27) SIF data from the Global Ozone Monitoring Instrument 2 (GOME-2) in this study as a proxy for GPP (https://avdc.gsfc.nasa.gov/pub/data/satellite/MetOp/GOME_F/v27/). SIF was retrieved at far-red wavelengths ~ 740 nm based on a principal component analysis approach (Joiner et al. 2013). In this study, we used the level-2 monthly SIF data at 0.5° spatial resolution for 2007-2016. Annual SIF was calculated as an average of all months in a calendar year.

2.2.6 Global ET datasets

The MODIS ET (MOD16A2.006) product is based on the Penman-Monteith algorithm using daily GMAO climate data, MODIS land cover, albedo, LAI and EVI as input (Mu et al. 2011). The MODIS ET data were obtained through NASA LPDAAC with 500m, 8-day resolution (https://lpdaac.usgs.gov). In our study, MODIS ET was aggregated into monthly, 0.5° resolution for the period of 2001-2016. Monthly MODIS T was partitioned from MODIS ET using the approach developed by Wei et al. (2017). All monthly ET and T were summed to annual values for each year during 2001-2016 to match the VPM GPP dataset.

GLEAM (Global Land Evaporation Amsterdam Model) (v3.2a) was designed to maximize the advantages of remote sensing and climate data to estimate the different components of land evaporation (Martens et al. 2017; Miralles et al. 2011). It relies on a modified Priestley and Taylor approach using meteorological data, microwave

Vegetation Optical Depth, and soil moisture as inputs. This product derived land ET, T, and canopy evaporation at daily, 0.25° resolution for 1980-2017. For our study, we aggregated daily ET and T data to monthly, 0.5° resolution for 2007-2016. All monthly ET and T data were summed to annual values for each year from 2007 to 2016 to match the SIF dataset.

2.2.7 Partitioning T from ET datasets

The T/ET ratio is logarithmically related to LAI (Wang et al. 2014; Wei et al. 2017). Given the strong relationship between LAI and T/ET, we used the approach developed by Wei et al. (2017) to partition T from ET at monthly timescale using flux tower ET and MODIS ET data (Equation 2.1).

$$T = \sum_{i=1}^{n} ET \times f_i \times aLAI^b \quad (2.1)$$

where a and b are two coefficients related to specific land cover type *i* (Table S2.2), f_i is the proportion of each land cover type in a site or pixel. For the flux tower dataset, f_i equals 1, as flux towers were located in pure land cover types. For the MODIS ET dataset, f_i equals the yearly proportion of each land cover type in a 0.5° pixel, which was recalculated from the sub-pixel proportion of each land cover type with 0.05°resolution from MODIS land cover (MCD12C1.006) (Table 2.1). LAI in the equation came from the MODIS LAI product (MOD15A2H.006), which has an 8-day, 500m resolution (Table 2.1). For the flux tower dataset, we used the 500m monthly averaged LAI to represent the site-level LAI. For the MODIS ET dataset, we generated the 0.5° monthly averaged LAI to represent the grid-level LAI. In our study, we only focused on those dominant land cover types with water proportion in a pixel <10% (Figure S2.1).

Table 2.1 Datasets used in this study.

Variable	Description	Temporal resolution	Spatial resolution	Reference
GPP_{EC}, PPT_{EC}, LE_{EC}	Gross primary production, precipitation, and latent heat from FLUXNET 2015	Monthly 1999-2014	100~1000m	
PPT_{CRU}, TMP_{CRU}, TMN_{CRU},VAP_{CRU}	Precipitation, temperature, minimum temperature, and vapor pressure from CRU TS 4.01	Monthly 1901-2016	0.5°	(Harris et al. 2014)
GPP_{VPM}	Gross primary production from VPM	8-day 2000-2017	500m	(Zhang et al. 2017)
SIF_{GOME-2}	Sun-induced chlorophyll fluorescence from GOME-2 v27	Monthly 2007-2017	0.5°	(Joiner et al. 2013)
ET_{MODIS}	Evapotranspiration from MODIS (MOD16A2.006)	8-day 2001-2017	500m	(Running et al. 2017)
ET_{GLEAM}, T_{GLEAM}	Evapotranspiration and transpiration from GLEAM 3.2a	Monthly 1980-2017	0.25°	(Martens et al. 2017)
LAI_{MODIS}	Leaf area index from MODIS (MOD15A2H.006)	8-day 2000-2017	500m	(Myneni et al. 2015)
Land cover	Sub-pixel proportions of land cover types from MCD12C1.006	Yearly, 2001-2016	0.05°	(Friedl and Sulla-Menashe 2015)

2.3 Results

2.3.1 Spatial distributions of mean annual GPP, SIF, PPT, and water fluxes

Across 111 FLUXNET sites, there was a general spatial consistency between mean annual GPP_{VPM}, SIF_{GOME-2}, and mean annual GPP_{EC} from flux tower sites (Figure 2.1a-b, Figure S2.2a,d). However, ET and T from MODIS and GLEAM were underestimated

relative to flux tower estimates (Figure S2.3b,c,e,f). According to site- and global-scale results, ET was found to saturate with increasing PPT (Figure S2.3a-c). However, T increased linearly with ET for all datasets (Figure S2.3d-f). The slope of the linear regression between T and ET was stable at ~ 0.8 (Figure S2.3d-f). On average, ET accounted for 64%±1% of PPT, and T accounted for 71%±3% based on all datasets. Across 111 FLUXNET sites during 2000-2014, average annual GPP_{EC} was 1260 $gC/m^2/yr$, and average annual PPT_{EC}, ET_{EC}, and T_{EC} estimates were 767mm/yr, 498mm/yr, and 339 mm/yr, respectively. Across the global vegetated land area (~114 million km^2) during 2001-2016, average annual GPP_{VPM} was 1035 $gC/m^2/yr$; average annual PPT_{CRU} was 847mm/yr; and average annual ET_{MODIS} and T_{MODIS} were 524 mm/yr, and 376mm/yr, respectively. During 2007-2016, average annual SIF_{GOME-2} was 0.5 $mW/m^2/nm/sr$; average annual PPT_{CRU} was 811 mm/yr; and average annual ET_{GLEAM} and T_{GLEAM} were 519 mm/yr, and 379mm/yr, respectively.

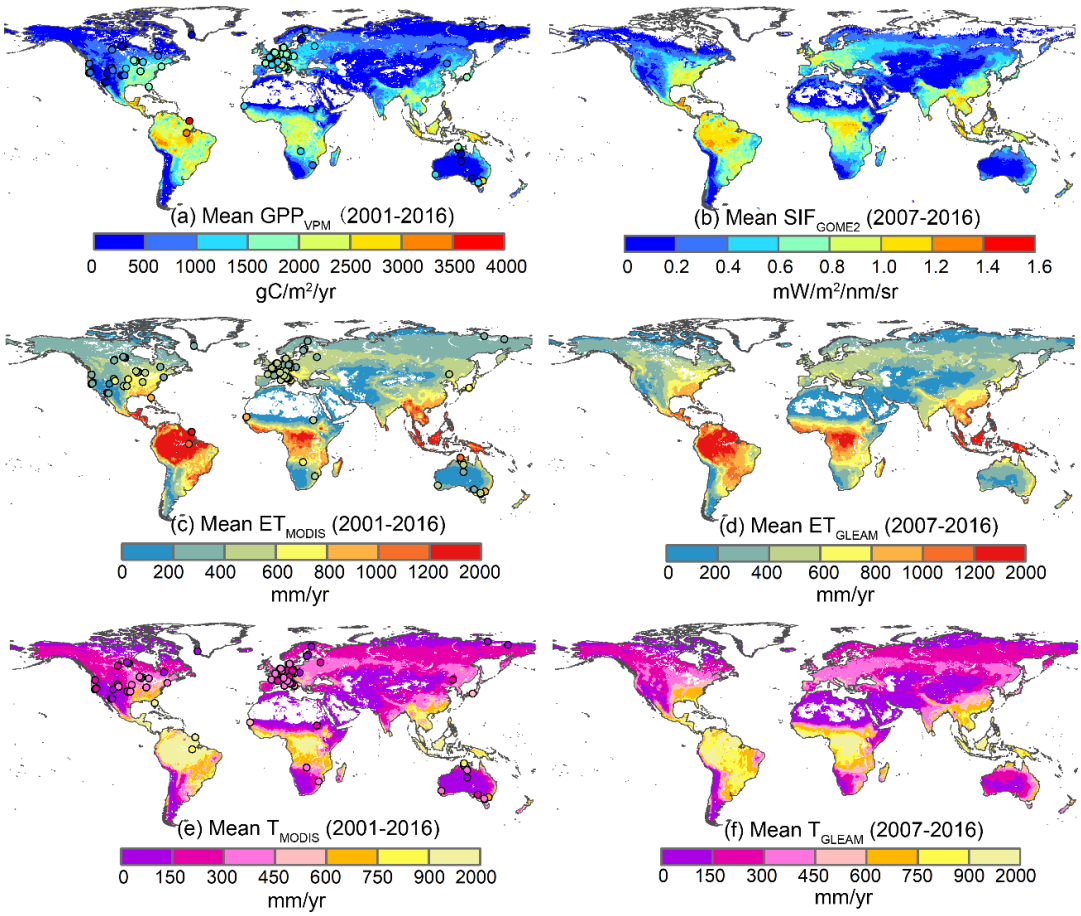

Figure 2.1 Geographical distribution of mean annual GPP, SIF, ET and T at the site and global scales. The left panels are mean estimates of annual GPP_{VPM} (a), ET_{MODIS} (c), and T_{MODIS} (e) for 2001-2016. Black outlined circles represent ground estimates of mean annual GPP_{EC} (a), ET_{EC} (c), and T_{EC} (e) from 111 FLUXNET sites for 2000-2014. The right panels are mean annual estimates of SIF_{GOME-2} (b), ET_{GLEAM} (d), and T_{GLEAM} (f) for 2007-2016.

2.3.2 The relationships between annual GPP, SIF and PPT, ET, and T across terrestrial ecosystems

The relationships between annual GPP, SIF and PPT were nonlinear with different saturating points from the site level to the global scale (Figure 2.2a,d,g). At the site level, GPP_{EC} increased with PPT_{EC} positively and roughly saturated when PPT_{EC} exceeded 1463 mm/yr. At the global scale, GPP_{VPM} and SIF_{GOME-2} became saturated when PPT_{CRU} exceeded 3219 mm/yr and 2299 mm/yr, respectively. Here, the saturation point was

selected at the curvature deviated more than 80% from the initial point (x=0). There was substantial variation in sensitivity of GPP (or SIF) to PPT interannual variability across terrestrial ecosystems (Figure 2.2a,d,g, Figure S2.4a,d). Semi-arid regions where mean PPT was 473.0±170.5 mm/yr, e.g. central North America, Kazakhstan and Mongolia, had the highest sensitivity of GPP (or SIF) to PPT (slope>=1.6 g C/kg H_2O or 1.0 mW/nm/sr/kg H_2O) (Figure S2.4a,d). Also, the mean sensitivity of GPP and SIF to PPT was highly variable across biomes (Figure 2.3). Generally, savannas showed the highest sensitivity of GPP to PPT and forests showed the lowest sensitivity to PPT in the flux tower dataset (Figure 2.3a). Grasslands showed a consistently high sensitivity of GPP and SIF to PPT and forests showed the lowest sensitivity to PPT in global datasets (Figure 2.3d,g).

The relationships between annual GPP, SIF and ET or T were linear across sites and the globe (Figure 2.2b-c,e-f,h-i). Higher coefficients of determination (R^2) were estimated for the relationship between GPP (and SIF) and ET (or T) in comparison with the GPP (and SIF)~PPT relationship. Unlike PPT, the mean sensitivity of GPP and SIF to ET and T showed moderate changes across all ecosystems (Figure 2.2b-c,e-f,h-i). Also, the mean sensitivity of GPP and SIF to ET and T exhibited less variation across biomes as shown by a smaller CV (Figure 2.3). In general, grassland and cropland GPP and SIF was highly sensitive to ET and T, and forest GPP and SIF were least sensitive to ET and T in the global datasets (Figure 2.3e-f, h-i). However, in the flux tower dataset, cropland GPP was least sensitive to ET and T (Figure 2.3b-c).

To assess the impact of VPD on carbon-water coupling, we multiplied GPP and SIF by the square root of VPD (annual sums of monthly $GPP \times VPD^{0.5}$ or $SIF \times VPD^{0.5}$), a

term developed by Zhou et al. (2015) (Figure S2.5j-l). We found that the linear relationship between $GPP \times VPD^{0.5}_{EC}$ and T_{EC} in the flux tower dataset was stronger than the GPP_{EC}~T_{EC} relationship, with the R^2 increasing from 0.46 to 0.62 (Figure S2.5j). However, this stronger carbon-water coupling when incorporating VPD was not shown in the global results (Figure S2.5k,l).

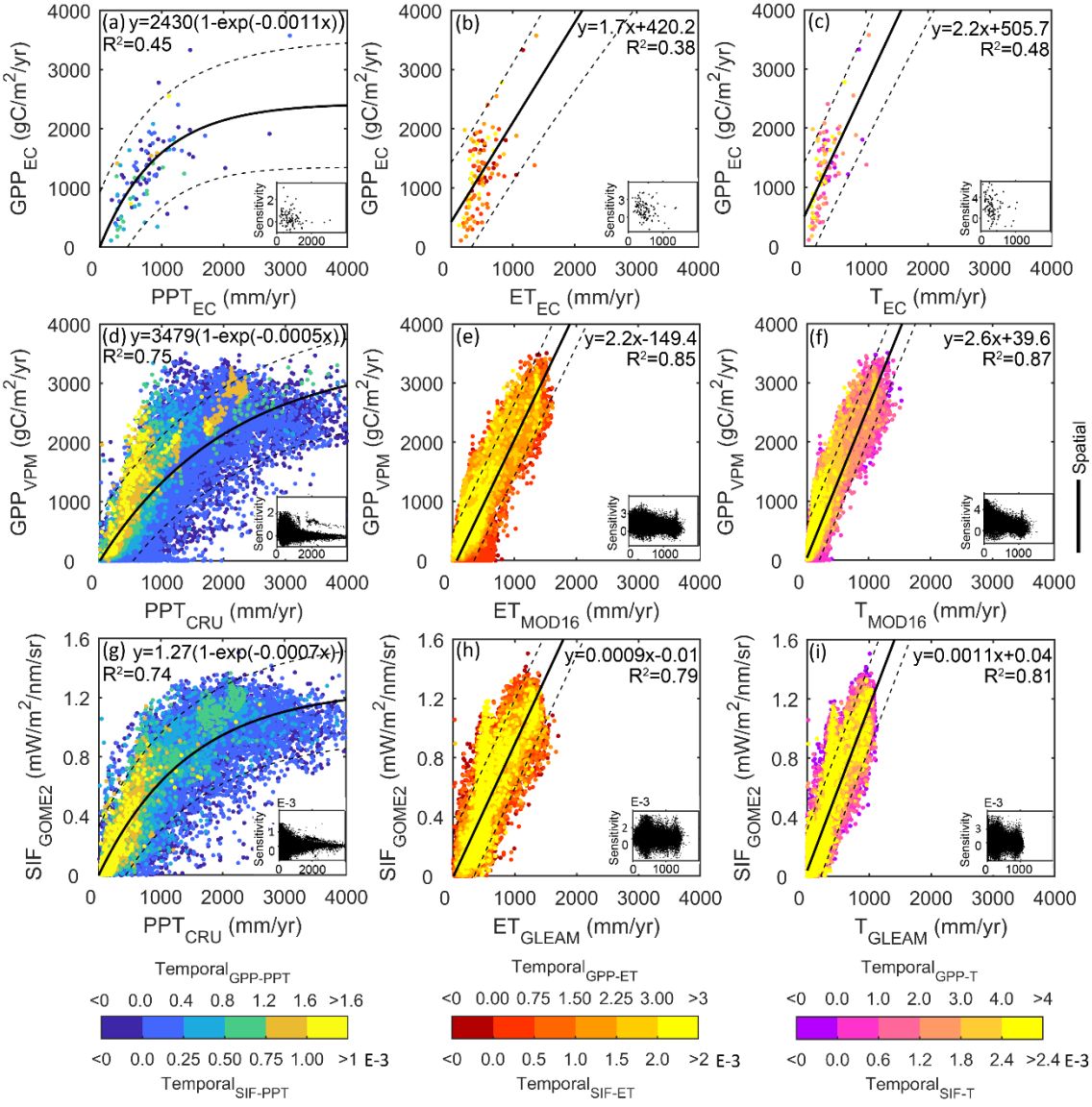

Figure 2.2 Spatiotemporal relationships between annual GPP, SIF and PPT, ET, and T across 111 FLUXNET sites (a-c) and the global vegetated land (d-i). 983 site-year data with >=4 years' measurements in 2000-2014 were used for a-c. All grid-year data during 2001-2016 and 2007-2016 from global datasets were used for d-f

and g-i, respectively. The spatial relationships between mean annual GPP (and SIF) and PPT are described by a negative exponential model, while the spatial relationships between mean annual GPP (and SIF) and ET, and T are linear (black bold lines). Black dashed lines show the 95 percent prediction level. All fitted models are significant (p<0.0001). The temporal (or the interannual) relationship at each site or pixel was fitted linearly and each color shows the sensitivity (slope of the linear regression). The insets show the respective distribution of GPP and SIF sensitivities to PPT, ET, and T (the x-axis represents PPT, ET, or T and the y-axis represents the sensitivity of GPP or SIF to PPT, ET or T).

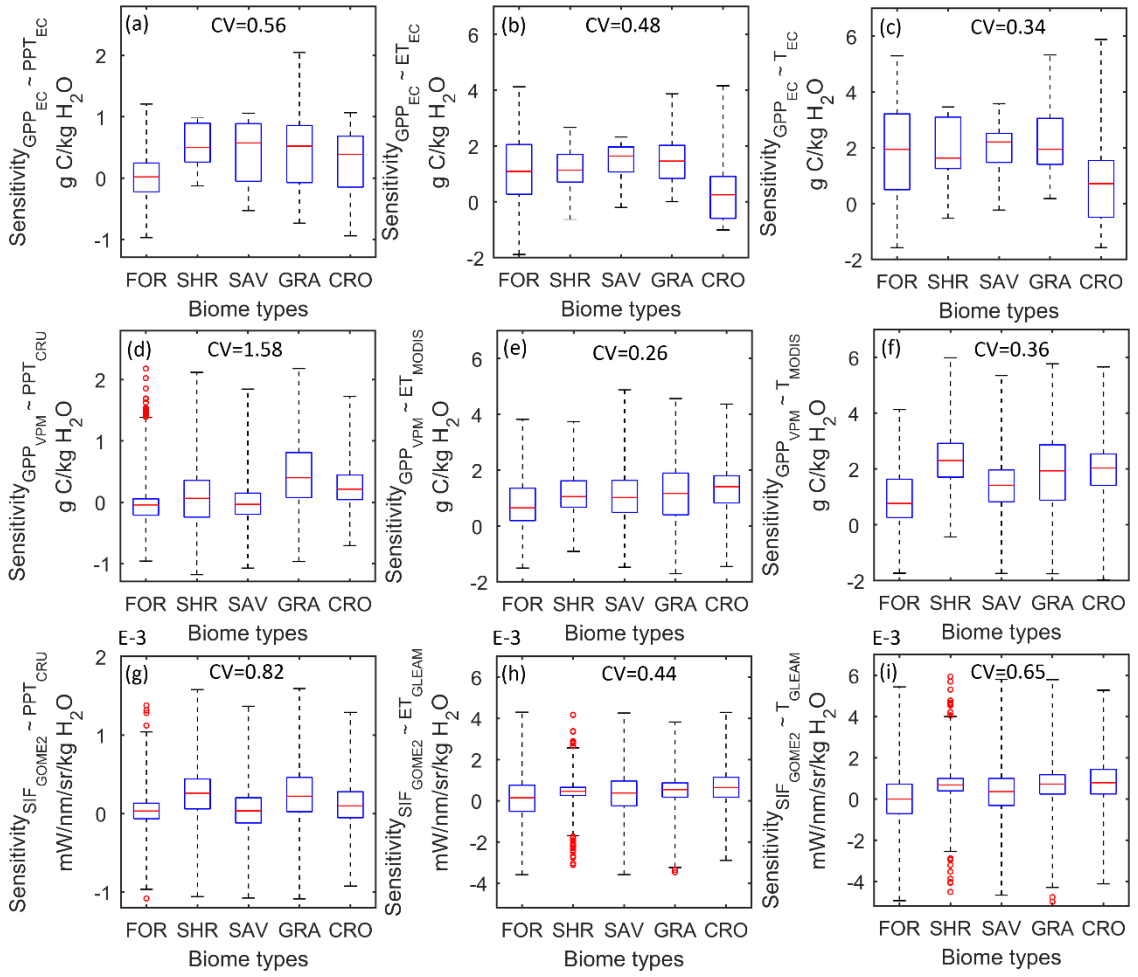

Figure 2.3 Comparison of the sensitivity of GPP and SIF to PPT, ET, and T for different biomes. Sensitivity of GPP_{EC} across 111 FLUXNET sites for 2000-2014 (a-c), global GPP_{VPM} for 2001-2016 (d-f), and global SIF_{GOME2} for 2007-2016 (g-i). CV represents the coefficient of variation of mean GPP or SIF sensitivity to PPT and water fluxes across biomes (FOR=Evergreen Needleleaf forest, Evergreen Broadleaf forest, Deciduous Needleleaf Forest, Deciduous Broadleaf Forest, Mixed Forest, SHR= Open Shrublands, Closed Shrublands, SAV=Woody Savannas, Savannas, GRA=Grasslands, Wetlands, CRO=Croplands).

2.3.3 The relationships between annual GPP, SIF and PPT, ET, and T in severe drought and pluvial years

To explore the responses of GPP and SIF to PPT and water fluxes under different hydroclimatic conditions, we analyzed the relationships between GPP, and SIF and PPT, ET, and T during extreme drought, normal, and pluvial years by evaluating the temporal variation in regression slopes across these years. In total, 57 FLUXNET sites, concentrated in the U.S. and central Europe, experienced all three climate conditions during 2001-2014 (Figure S2.6a). Approximately 89% and 64% of global vegetated land area experienced all three climate conditions during 2001-2016 and 2007-2016, respectively (Figure S2.6b,c).

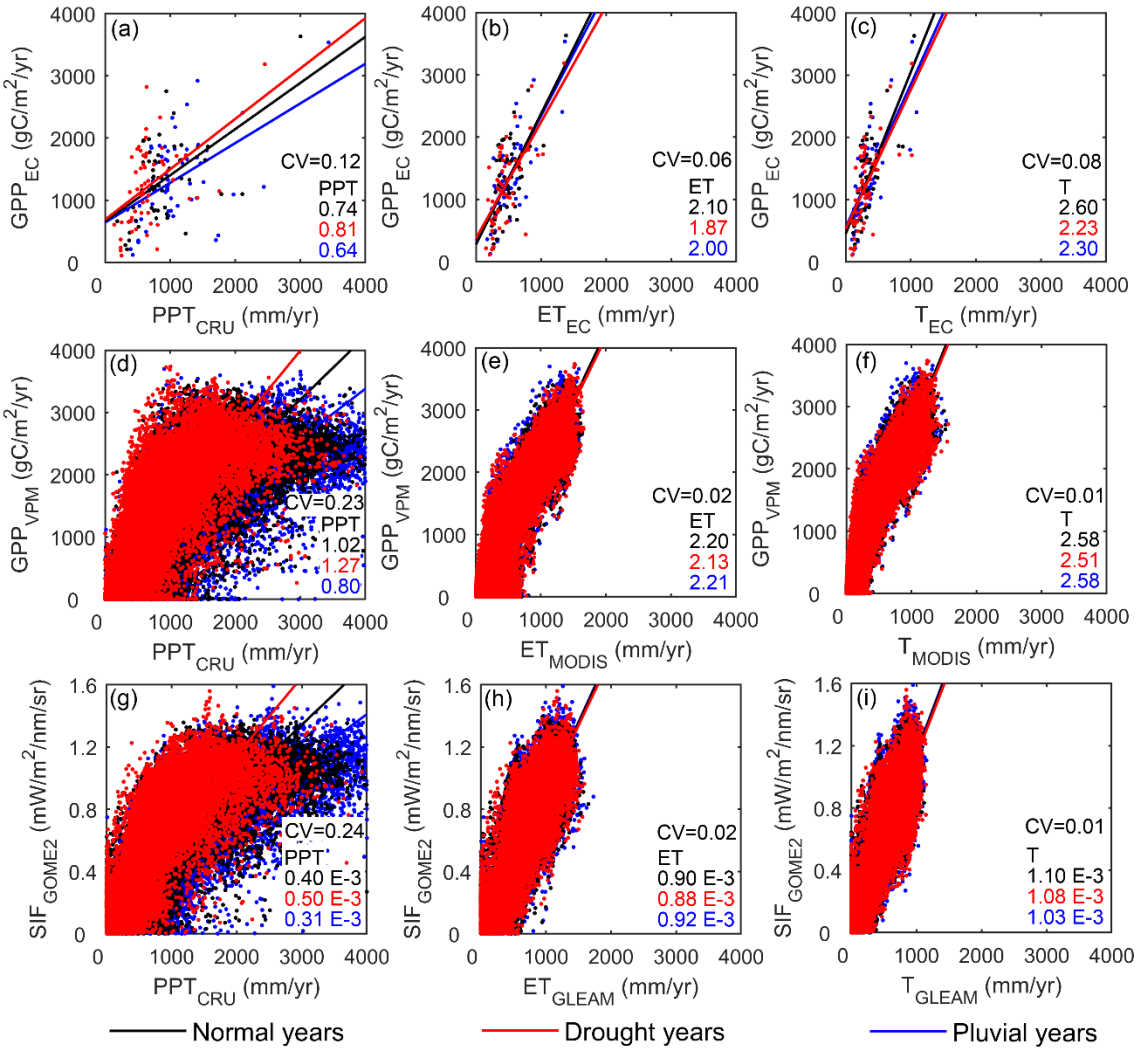

Figure 2.4 Relationships between GPP, and SIF and PPT, ET, and T under different hydroclimatic conditions (severe drought, normal and pluvial years) across 57 FLUXNET sites and the globe. Each point represents multi-year mean annual estimates of a hydroclimatic period. The solid lines represent the linear regressions of GPP and SIF to PPT or water fluxes. The numbers in each subplot are the regression slopes representing the sensitivity of GPP and SIF to PPT and water fluxes in normal (black), drought (red), and pluvial (blue) years.

The sensitivities of GPP and SIF to PPT and water fluxes exhibited less variation across altered hydroclimatic conditions from PPT to ET and T, as presented by smaller coefficients of variation (CV) of regression slopes (Figure 2.4). Specifically, the sensitivities of GPP and SIF to PPT increases noticeably in severe drought years and decreases in pluvial years in all datasets (Figure 2.4a,d,g). However, there was no obvious

change in the sensitivity of GPP and SIF to ET or T in altered hydroclimatic conditions (Figure 2.4b-c, e-f, h-i).

2.4 Discussion

2.4.1 Spatiotemporal relationships between GPP, SIF and PPT, ET, and T

In this study, the spatiotemporal relationships between annual GPP, SIF and PPT, ET, and T were quantified at both the site and global scales by combining FLUXNET2015 dataset with spatially continuous remote sensing and climate datasets. The sensitivities of annual GPP and SIF to PPT and each water flux were further evaluated across biomes and under contrasting hydroclimatic conditions (severe drought to pluvial periods). Thus far, ecosystem carbon-water coupling has been widely studied based on site-level measurements with a limited number of sites and was focused on the responses of NPP to PPT or ET (Huxman et al. 2004; Knapp et al. 2017; Ponce Campos et al. 2013). However, there is no consensus on the spatiotemporal variations in carbon-water coupling across ecosystems and under different levels of water stress (Ponce Campos et al. 2013; Tang et al. 2014; Yang et al. 2016; Yu et al. 2017). In our study, there was a relatively large spatial variation in the sensitivity of GPP and SIF to PPT and a small variation to ET and T across terrestrial ecosystems. Also, there were no obvious changes in the responses of GPP and SIF to ET or T in different hydroclimatic conditions, which might conflict with previous findings. Our study comprehensively evaluated the coupling of the carbon and water cycles from the site to global scale and found a generally common response of carbon uptake to water use among different biomes and in climate extremes.

Across 111 FLUXNET sites and the globe, ecosystem carbon-water coupling is stronger and more linear with ET and T than PPT, reflecting the intrinsic stomatal control

on carbon-water exchange at leaf scale (Figure 2.2). In our results, GPP and SIF increased nonlinearly with PPT, with different saturation values across datasets (Figure 2.2a,d,g). The highest sensitivity of GPP and SIF to PPT occurred around PPT at 473.0±170.5 mm/yr in semi-arid regions and the lowest sensitivity occurred in tropical forests (Figure 2.2a,d,g Figure S2.4a,d), matching the previous findings that ecosystem RUE peaks when mean annual PPT is ~500 mm (Hsu et al. 2012; Paruelo et al. 1999). The varying sensitivity between semi-arid regions and tropical regions reflects the different climatic controls on GPP and PPT (Ahlstrom et al. 2017; Huxman et al. 2004). GPP and SIF were linearly coupled with ET and T and the spatial variation of mean sensitivities among biomes decreased, which indicated that WUE was generally consistent across vegetation types (Figure 2.2b-c,e-f,h-i, Figure 2.3). At the biome level, forest GPP and SIF was the least sensitive to ET and T, and croplands were the most sensitive in the global results, which is in conflict with model simulations that estimate that tropical forests have the highest WUE (Cheng et al. 2017; Sun et al. 2016). However, cropland GPP was the least sensitive to ET and T in flux dataset, which agreed with previous findings from flux tower sites (Tang et al. 2014). The different spatiotemporal scales between flux tower and global datasets could be a major cause for the different results generated from the datasets (Figure 2.3). In addition, results from the flux tower dataset showed an improved relationship between $GPP \times VPD^{0.5}$ and T (Figure S2.5j), suggesting a more convergent physiological response of carbon assimilation to water loss across ecosystems. However, we failed to see a stronger relationship when incorporating $VPD^{0.5}$ in global datasets (Figure S2.5k-l), which was possibly due to the uncertainties in CRU climate data and the failure to capture VPD effects in GPP_{VPM}. Also, SIF has a close relationship with the

amount of photosynthetically active radiation absorbed by chlorophyll (APAR), and might not be as sensitive to VPD as photosynthesis (Yang et al. 2018; Yang et al. 2015).

Under different hydroclimatic conditions, the variation in the carbon-water coupling was also smaller with ET and T than PPT, suggesting a common responses of carbon uptake to plant water use under different levels of water stress (Figure 2.4). GPP and SIF showed an increasing sensitivity to PPT in severe drought years and decreasing sensitivity in pluvial years (Figure 2.4 a,d,g), which is consistent with previous studies that RUE increases with drought due to the reduced water availability and reduction in runoff (Huxman et al. 2004). However, there is no obvious increase or decrease of sensitivity in severe drought or pluvial years, which is contrary to previous site-level findings that ecosystem WUE increases significantly with drought to a maximum across all biomes (Ponce Campos et al. 2013), or that responses of ecosystem WUE to drought varies for different regions on the Earth (Yang et al. 2016). In this study, the large number of sites and spatial scale (i.e. globe) could average the plant community-level responses and result in a common response of GPP and SIF to ET or T in an altered water condition, to some degree. Also, the definitions of severe drought, normal, and pluvial periods were solely based on the distribution of PPT. An extreme drought year with low PPT may still have large ET or T estimates in our datasets, resulting lower sensitivity of GPP and SIF to ET or T in dry years.

2.4.2 Data uncertainties and limitations

This study employed both site-level and global datasets, in order to examine the spatiotemporal relationships of carbon-water cycling, which largely rely on the data quality. We used all the latest version of each data product to reduce the data uncertainty

shown in prior literature. For example, it has been demonstrated that collection 6 MODIS data (i.e. ET and LAI) has a higher accuracy than collection 5 (Yan et al. 2016). And the v27 SIF from GOME-2 provided improved bias corrections and calibration over v26. However, several data issues could still have minor impacts on our results. First, the GOME-2 instruments have exhibited a strong decreasing trend in SIF that is caused by sensor degradation, which would involve large uncertainty in any temporal analysis (Zhang et al. 2018c). In this study, the degradation could influence the absolute estimate of SIF sensitivity to PPT or water fluxes at a single site or a pixel, while the relative spatial variation of the sensitivity across biomes would not be influenced, since the degradation issue occurs in each site and pixel systematically. Second, the GPP_{EC}~ET_{EC} relationship (R^2=0.38) is weak in the flux tower dataset, which could be induced by lack of closure of the energy budget in flux tower dataset. In this study, we used the original LE data without energy balancing approach to estimate ET. Third, partitioning T from ET is still a challenge in hydrological field. In our study, we used the algorithm from Wei et al. (2017) to partition T from ET. In equation 2.1, ET was the sum of E and T in Wei et al. (2017), which doesn't count canopy interception. However, we didn't exclude the interception from ET_{MODIS} and ET_{EC}. In spite of these data issues, the results are generally consistent and robust across all datasets in our study.

2.5 Conclusion

A comprehensive understanding of the carbon-water coupling in ecosystems is important for predicting future ecosystem responses to climate variability. Using observations from flux tower sites and remote sensing estimates, this study quantified the relationships between GPP, SIF and PPT, and water fluxes across all terrestrial ecosystems and under

different hydroclimatic conditions. Our analysis showed that GPP and SIF have a saturating spatial relationship with PPT and have strong, linear relationships with ET and T. In comparison with PPT, there were no substantial changes in the mean sensitivity of GPP and SIF to ET and T across terrestrial ecosystems and different hydroclimatic conditions, which suggested that the response of carbon uptake to water use of vegetation was generally consistent across biomes and climate extremes.

Supplementary materials

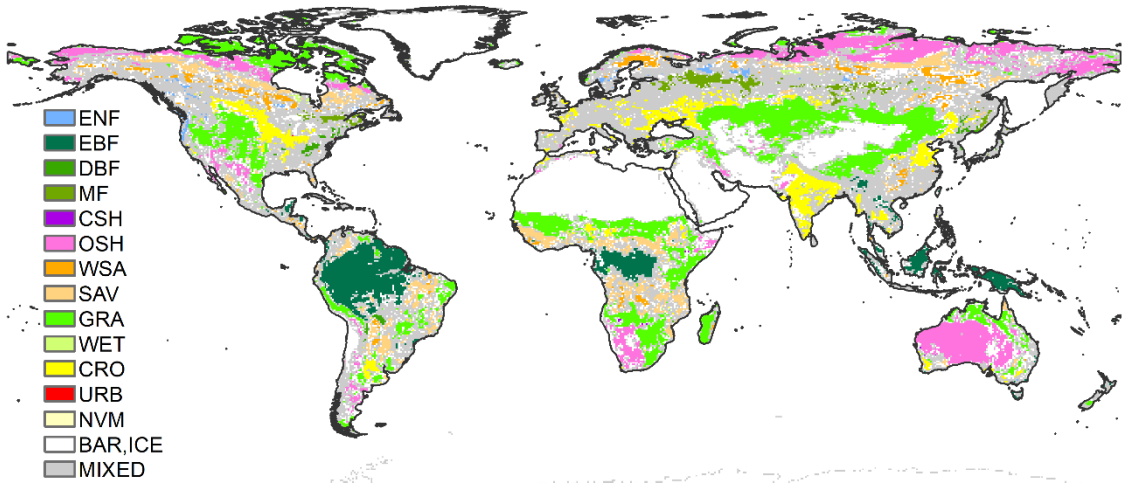

Figure S2.1 Dominant land cover type map in 2001-2016 based on MCD12C1.006 with 0.5° resolution. The dominant land cover type in a pixel is defined as a land cover occupying more than 70% of the grid cell in each year during the period 2001-2016. Pixels with water proportion > 10% were excluded. This map created in ArcMap 10.2.

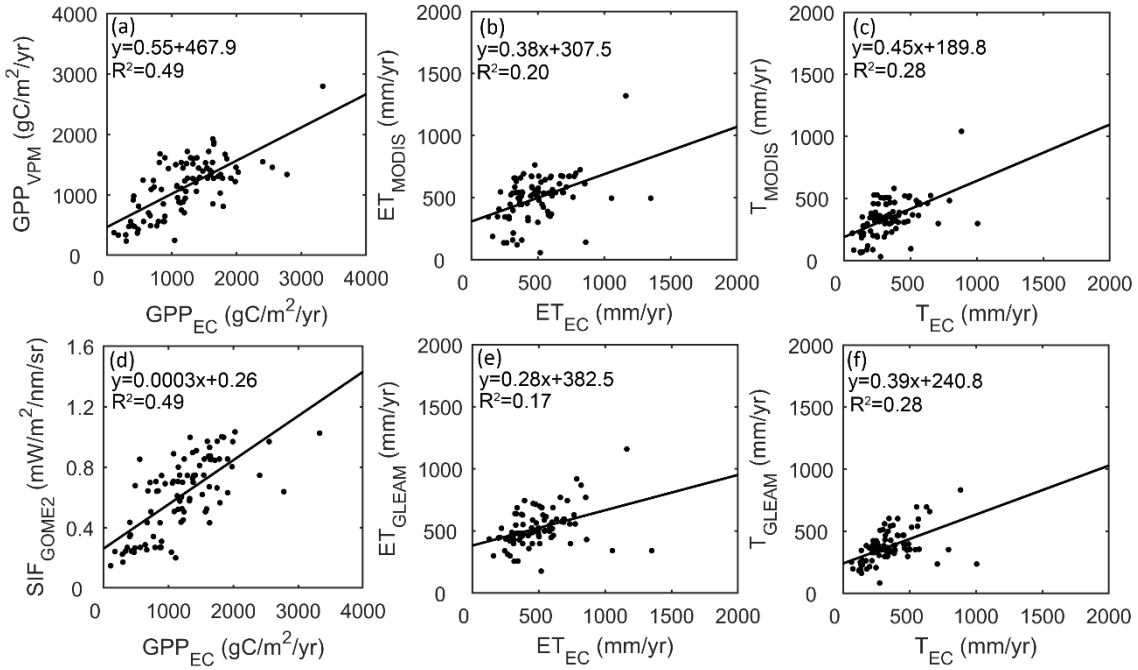

Figure S2.2 Comparison of GPP, SIF, ET, and T estimates from remote sensing datasets (0.5° spatial resolution) with GPP, ET, and T derived from 111 flux tower sites. All linear regression were significant (p<0.0001).

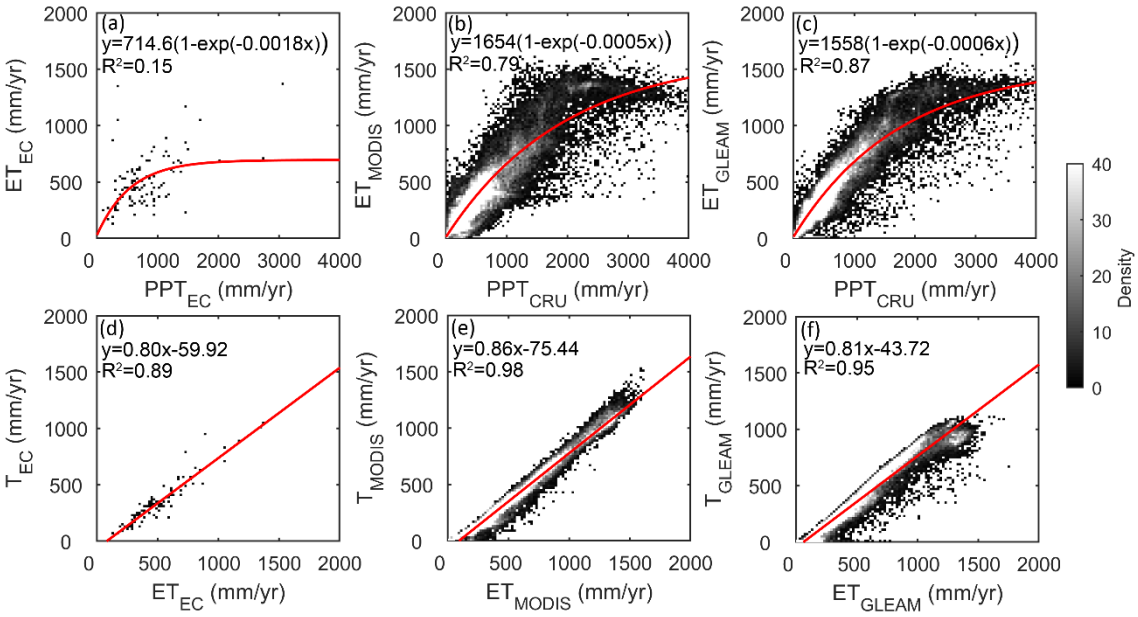

Figure S2.3 Relationships between ET and PPT (a-c), and T and ET (d-f) at eddy flux sites and the global scale. The relationship between ET and PPT is described by a negative exponential model, while the relationship between T and ET is described by a linear regression model. All fitted models are significant (p<0.0001).

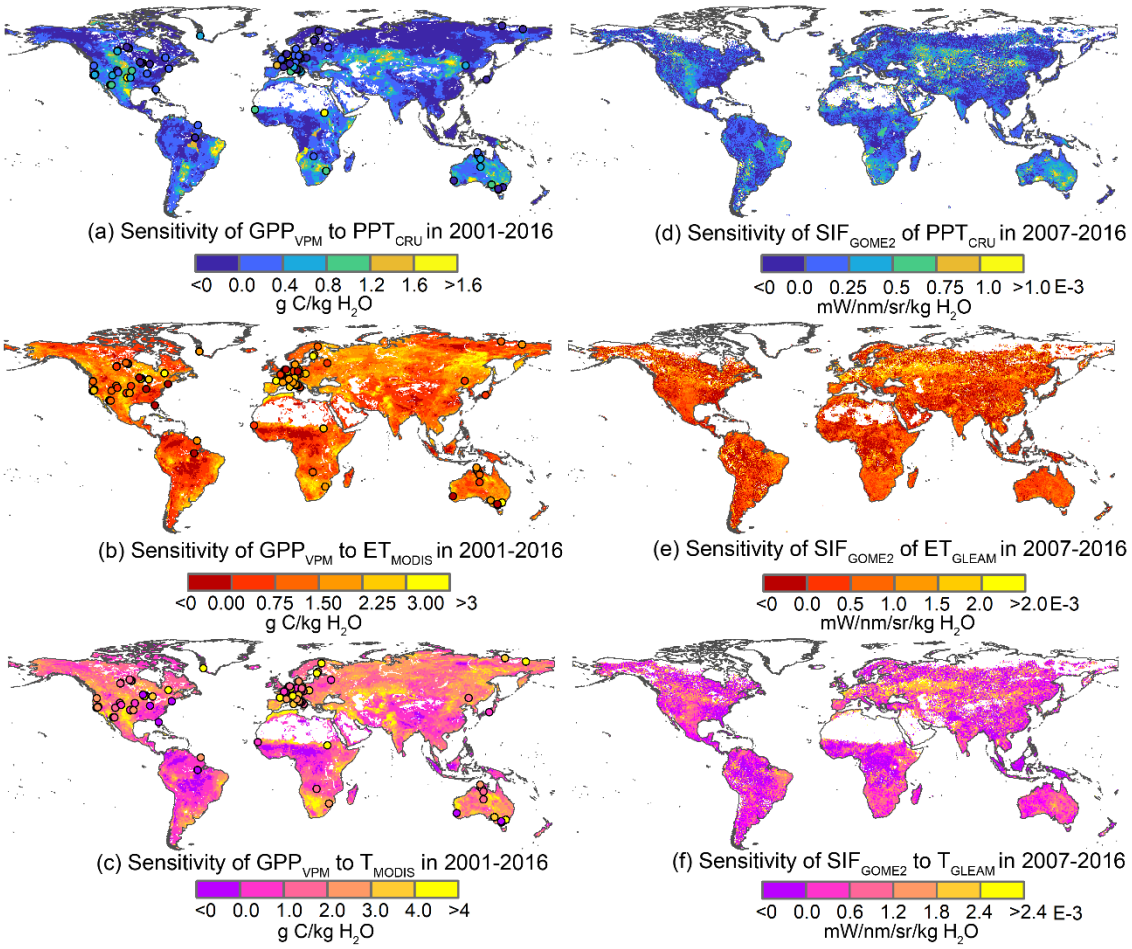

Figure S2.4 Geographical distribution of the sensitivity of GPP and SIF to PPT, ET, and T interannual variability at 111 FLUXNET sites for 2000-2014 (black outlined circles in a-c) and across the globe during 2001-2016 (a-c) and 2007-2016 (d-f).

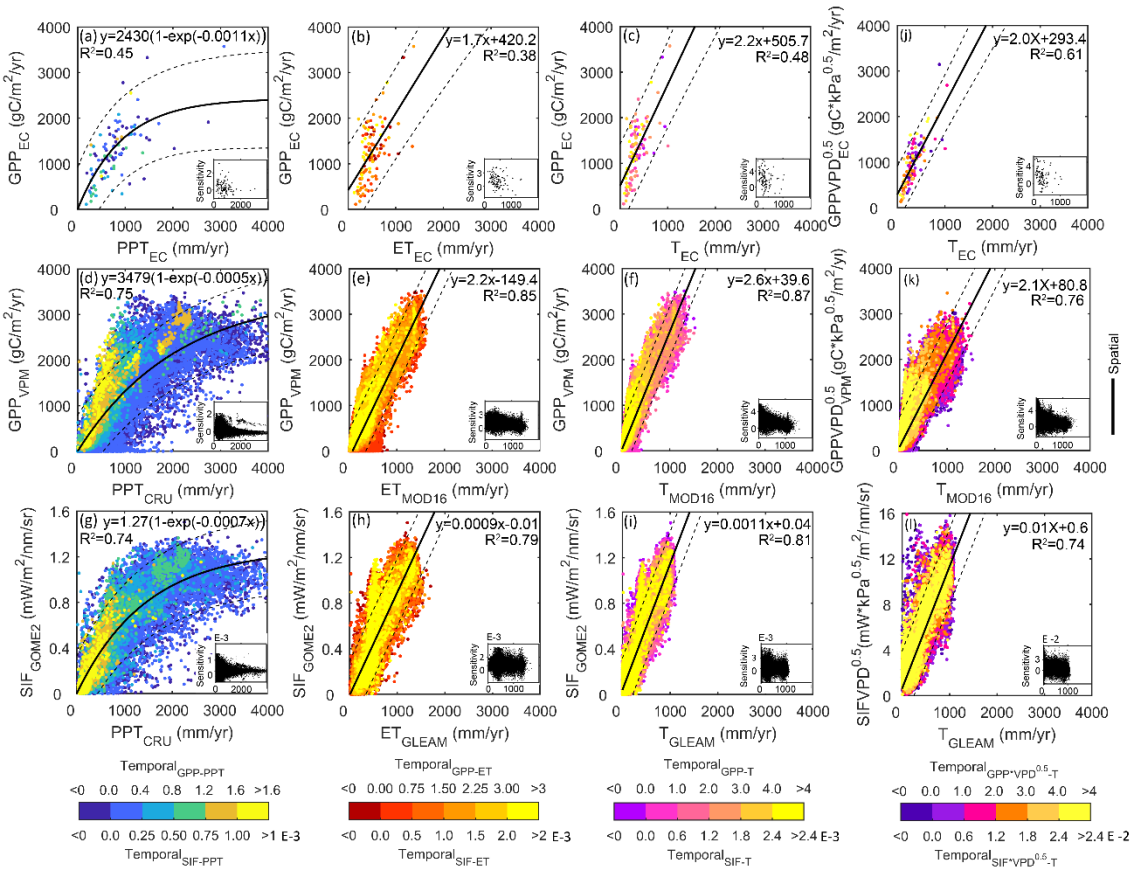

Figure S2.5 Spatiotemporal relationships between annual GPP, SIF and PPT, ET, and T by incorporating the VPD effect across 111 FLUXNET sites (a-c) and the global vegetated land (d-l).

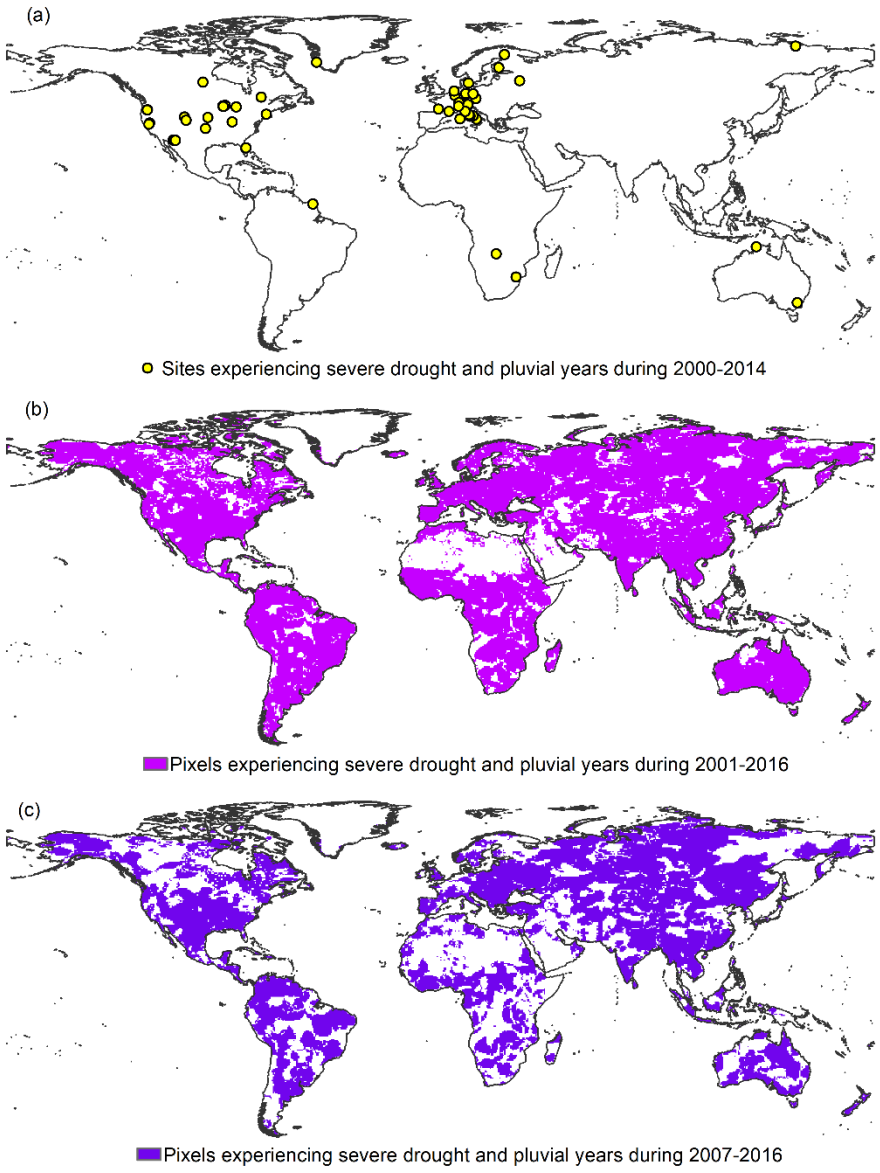

Figure S2.6 Sites or pixels experienced severe drought and pluvial years during the period of 2000-2014 (a), 2001-2016 (b), and 2007-2016 (c) using PPT_{CRU} in 1987-2016 as baseline.

Table S2.1 111 Flux tower sites and corresponding years used in this study.

ID	Site ID	Latitude	Longitude	IGBP type	Years used	Number of years
1	AT-Neu	47.1167	11.3175	GRA	2002-2012	11
2	AU-ASM	-22.283	133.249	ENF	2010-2013	4
3	AU-Cpr	-34.0021	140.5891	SAV	2010-2014	5
4	AU-DaP	-14.0633	131.3181	GRA	2007-2013	7
5	AU-DaS	-14.1593	131.3881	SAV	2008-2014	7
6	AU-Dry	-15.2588	132.3706	SAV	2008-2014	7
7	AU-Gin	-31.3764	115.7138	WSA	2011-2014	4
8	AU-How	-12.4943	131.1523	WSA	2001-2014	14
9	AU-Rig	-36.6499	145.5759	GRA	2011-2014	4
10	AU-Stp	-17.1507	133.3502	GRA	2008-2014	7
11	AU-Tum	-35.6566	148.1517	EBF	2001-2014	14
12	AU-Wac	-37.4259	145.1878	EBF	2005-2008	4
13	AU-Whr	-36.6732	145.0294	EBF	2011-2014	4
14	BE-Bra	51.3092	4.5206	MF	2000-2014	14
15	BE-Lon	50.5516	4.7461	CRO	2004-2014	11
16	BE-Vie	50.3051	5.9981	MF	2000-2014	15
17	BR-Sa3	-3.018	-54.9714	EBF	2000-2004	5
18	CA-Man	55.8796	-98.4808	ENF	2000-2008	9
19	CA-NS1	55.8792	-98.4839	ENF	2002-2005	4
20	CA-NS2	55.9058	-98.5247	ENF	2001-2005	5
21	CA-NS3	55.9117	-98.3822	ENF	2001-2005	5
22	CA-NS4	55.9144	-98.3806	ENF	2002-2005	4
23	CA-NS5	55.8631	-98.485	ENF	2001-2005	5
24	CA-NS6	55.9167	-98.9644	OSH	2001-2005	5
25	CA-NS7	56.6358	-99.9483	OSH	2002-2005	4
26	CA-Qfo	49.6925	-74.3421	ENF	2003-2010	8
27	CA-SF1	54.485	-105.8176	ENF	2003-2006	4
28	CA-SF2	54.2539	-105.8775	ENF	2001-2005	5
29	CA-SF3	54.0916	-106.0053	OSH	2001-2006	6
30	CH-Cha	47.2102	8.4104	GRA	2005-2014	10
31	CH-Dav	46.8153	9.8559	ENF	2000-2014	15
32	CH-Fru	47.1158	8.5378	GRA	2005-2014	10
33	CH-Lae	47.4781	8.365	MF	2004-2014	11
34	CH-Oe1	47.2858	7.7319	GRA	2002-2008	7
35	CH-Oe2	47.2863	7.7343	CRO	2004-2014	11
36	CN-Cng	44.5934	123.5092	GRA	2007-2010	4
37	CZ-wet	49.0247	14.7704	WET	2006-2014	9
38	CZ-BK1	49.5021	18.5369	ENF	2004-2008	5
39	DE-Geb	51.1001	10.9143	CRO	2001-2014	14
40	DE-Gri	50.9495	13.5125	GRA	2004-2014	11
41	DE-Hai	51.0792	10.453	DBF	2000-2012	13
42	DE-Kli	50.8929	13.5225	CRO	2004-2014	11
43	DE-Lkb	49.0996	13.3047	ENF	2009-2013	5

44	DE-Obe	50.7836	13.7196	ENF	2008-2014	7
45	DE-RuR	50.6219	6.3041	GRA	2011-2014	4
46	DE-Seh	50.8706	6.4497	CRO	2007-2010	4
47	DE-Spw	51.8923	14.0337	WET	2010-2014	5
48	DE-Tha	50.9636	13.5669	ENF	2000-2014	15
49	DK-NuF	64.1308	-51.3861	WET	2008-2014	7
50	DK-Sor	55.4859	11.6446	DBF	2000-2014	15
51	FI-Hyy	61.8475	24.295	ENF	2000-2014	15
52	FI-Jok	60.8986	23.5135	CRO	2000-2003	4
53	FI-Sod	67.3619	26.6378	ENF	2001-2014	14
54	FR-Fon	48.4764	2.7801	DBF	2005-2014	10
55	FR-Gri	48.8442	1.9519	CRO	2004-2013	10
56	FR-LBr	44.7171	-0.7693	ENF	2000-2001, 2003-2008	8
57	FR-Pue	43.7414	3.5958	EBF	2000-2014	15
58	GF-Guy	5.2788	-52.9249	EBF	2004-2014	11
59	IT-BCi	40.5238	14.9574	CRO	2004-2014	11
60	IT-CA1	42.3804	12.0266	DBF	2011-2014	4
61	IT-CA2	42.3772	12.026	CRO	2011-2014	4
62	IT-CA3	42.38	12.0222	DBF	2011-2014	4
63	IT-Col	41.8494	13.5881	DBF	2000-2014	15
64	IT-Cpz	41.7052	12.3761	EBF	2000-2008	9
65	IT-Lav	45.9562	11.2813	ENF	2003-2014	12
66	IT-MBo	46.0147	11.0458	GRA	2003-2013	11
67	IT-Noe	40.6061	8.1515	CSH	2004-2014	11
68	IT-Ren	46.5869	11.4337	ENF	2000-2013	14
69	IT-Ro2	42.3903	11.9209	DBF	2002-2008, 2010-2012	10
70	IT-SRo	43.7279	10.2844	ENF	2000-2012	13
71	IT-Tor	45.8444	7.5781	GRA	2008-2014	7
72	JP-SMF	35.2617	137.0788	MF	2002-2006	5
73	NL-Hor	52.2404	5.0713	GRA	2004-2011	8
74	NL-Loo	52.1666	5.7436	ENF	2000-2013	14
75	RU-Che	68.613	161.3414	WET	2002-2005	4
76	RU-Cok	70.8291	147.4943	OSH	2003-2013	11
77	RU-Fyo	56.4615	32.9221	ENF	2000-2014	15
78	SD-Dem	13.2829	30.4783	SAV	2005, 2007-2009	4
79	SN-Dhr	15.4028	-15.4322	SAV	2010-2013	4
80	US-AR1	36.4267	-99.42	GRA	2009-2012	4
81	US-AR2	36.6358	-99.5975	GRA	2009-2012	4
82	US-ARM	36.6058	-97.4888	CRO	2003-2012	10
83	US-Blo	38.8953	-120.6328	ENF	2000-2007	8
84	US-Cop	38.09	-109.39	GRA	2001-2003, 2006, 2007	5
85	US-GLE	41.3665	-106.2399	ENF	2005-2014	10

86	US-Ha1	42.5378	-72.1715	DBF	2000-2012	13
87	US-KS2	28.6086	-80.6715	CSH	2003-2006	4
88	US-Los	46.0827	-89.9792	WET	2000-2008, 2010, 2014	11
89	US-Me2	44.4523	-121.5574	ENF	2002-2014	13
90	US-Me6	44.3233	-121.6078	ENF	2010-2014	5
91	US-MMS	39.3232	-86.4131	DBF	2000-2014	15
92	US-Myb	38.0498	-121.7651	WET	2011-2014	4
93	US-Ne1	41.1651	-96.4766	CRO	2001-2013	13
94	US-Ne2	41.1649	-96.4701	CRO	2001-2013	13
95	US-Ne3	41.1797	-96.4397	CRO	2001-2013	13
96	US-NR1	40.0329	-105.5464	ENF	2000-2014	15
97	US-PFa	45.9459	-90.2723	MF	2000-2014	15
98	US-SRG	31.7894	-110.8277	GRA	2008-2014	7
99	US-SRM	31.8214	-110.8661	WSA	2004-2014	11
100	US-Syv	46.242	-89.3477	MF	2001-2008, 2012-2014	11
101	US-Ton	38.4316	-120.966	WSA	2001-2014	14
102	US-Twt	38.1087	-121.653	CRO	2009-2014	6
103	US-UMB	45.5598	-84.7138	DBF	2000-2014	15
104	US-UMd	45.5625	-84.6975	DBF	2007-2014	8
105	US-Var	38.4133	-120.9507	GRA	2000-2014	15
106	US-WCr	45.8059	-90.0799	DBF	2000-2006, 2010-2014	12
107	US-Whs	31.7438	-110.0522	OSH	2007-2014	8
108	US-Wi4	46.7393	-91.1663	ENF	2002-2005	4
109	US-Wkg	31.7365	-109.9419	GRA	2004-2014	11
110	ZA-Kru	-25.0197	31.4969	SAV	2000-2010	11
111	ZM-Mon	-15.4378	23.2528	DBF	2000-2009	4

Table S2.2 Coefficients (a and b) of each IGBP land cover type in Equation 1 adopted from Wei *et al*, 2017. Land cover types in parenthesis are the classes grouped by Wei *et al*, 2017.

Type ID	IGBP land cover types in this study	a	b
1	Evergreen Needleleaf Forest (Needle leave Forests)	0.48	0.32
3	Deciduous Needleleaf Forest (Needle leave Forests)		
2	Evergreen Broadleaf Forest (Broad leave Forests)	0.64	0.15
4	Deciduous Broadleaf Forest (Broad leave Forests)		
5	Mixed Forest (Mixed Forests)	0.52	0.26
6	Closed Shrublands (Shrublands and Grasslands)	0.69	0.28
7	Open Shrublands (Shrublands and Grasslands)		
8	Woody Savannas (Shrublands and Grasslands)		
9	Savannas (Shrublands and Grasslands)		
10	Grasslands (Shrublands and Grasslands)		
16	Barren or Sparsely Vegetated (Shrublands and Grasslands)		
11	Permanent Wetlands (Wetlands)	0.65	0.21
12	Croplands (Croplands)	0.66	0.18
14	Cropland/Natural Vegetation Mosaic (Croplands)		
13	Urban and Built-Up (Others)	-	-
15	Snow and Ice (Others)		
17	Unclassified (Others)		
0	Water surface (Others)		

Chapter 3: Global patterns of extreme drought-induced loss in land primary production: identifying ecological extremes from rain-use efficiency

Abstract

Quantifying the ecological patterns of loss of ecosystem function in extreme drought is important to understand the carbon exchange between the land and atmosphere. Rain-use efficiency [RUE; gross primary production (GPP)/precipitation] acts as a typical indicator of ecosystem function. In this study, a novel method based on maximum rain-use efficiency (RUEmax) was developed to detect losses of ecosystem function globally. Three global GPP datasets from the MODIS remote sensing data (MOD17), ground upscaling FLUXNET observations (MPI-BGC), and process-based model simulations (BESS), and a global gridded precipitation product (CRU) were used to develop annual global RUE datasets for 2001-2011. Large, well-known extreme drought events were detected, e.g. 2003 drought in Europe, 2002 and 2011 drought in the U.S., and 2010 drought in Russia. Our results show that extreme drought-induced loss of ecosystem function could impact 0.9%±0.1% of earth's vegetated land per year and was mainly distributed in semi-arid regions. The reduced carbon uptake caused by functional loss (0.14 ± 0.03 PgC/yr) could explain more than 70% of the interannual variation in GPP in drought-affected areas ($p \leqslant 0.001$). Our results highlight the impact of ecosystem function loss in semi-arid regions with increasing precipitation variability and dry land expansion expected in the future.

3.1 Introduction

Climate change is projected to increase the frequency and intensity of drought in the mid- to late 21st century (Stocker et al. 2013). Droughts can alter the terrestrial carbon cycle by affecting the composition, structure and functioning of ecosystems. Under extreme climate conditions, enhanced droughts and heat waves could fundamentally alter the structure or function of terrestrial ecosystems, outside the bounds of what is typical or normal variability (Reichstein et al. 2013; Smith 2011). Currently, the methods to investigate extreme ecological responses to extreme climate events, as well as the mechanisms and processes determining ecosystem responses are still lacking (Smith 2011). Thus, quantifying the spatiotemporal patterns of ecological responses to extreme drought is critical to predict future drought impacts under climate change.

Ecological responses to droughts has been observed variable ranging from little ecosystem impacts to major alteration of ecosystem structure and function (Smith 2011). The ability of an ecosystem to maintain its normal function during droughts greatly relies on the resistance of the ecosystem to environmental stresses, which is fundamentally determined by processes of drought tolerance and functionality of plant communities and the availability of water in the ecosystem (Mariotte et al. 2013). Extreme drought-induced loss of ecosystem function may occur when drought-resistant measures utilized by plant communities (e.g. closure of stomata, favoring drought-resistant plants) become overwhelmed by plant hydraulic limitations or mortality with further stress (Reyer et al. 2013). Loss of ecosystem function during extreme drought could cause an ecosystem to shift from carbon sink to carbon source, which can strongly influence the carbon exchange between the land and atmosphere (Frank et al. 2015a).

At the beginning of the 21st century, large-scale, extreme droughts have occurred throughout the world, attracting the attention of scientists (Breshears et al. 2005; Ciais et al. 2005; Doughty et al. 2015; Schwalm et al. 2012). Many studies have examined the regional or global impacts of droughts on terrestrial ecosystems and the carbon cycle by identifying drought events from a meteorological perspective (Ciais et al. 2005; Huang et al. 2016; Schwalm et al. 2012; Zhao and Running 2010). In these studies, droughts were usually identified by climate variables or other environmental drivers (e.g. precipitation, drought indices). There have also been some efforts to quantify the spatiotemporal ecological extremes using statistical techniques (Hoover et al. 2014; Liu et al. 2013; Zscheischler et al. 2014). Extreme ecological responses were identified by classifying the deviation of ecosystem variables (e.g. GPP, NDVI) from the norms derived from long-term datasets. A wide range of ecosystem responses to drought has been identified, from little impact on vegetation function in some instances, to major reductions in primary production in others (Ciais et al. 2005; Jentsch et al. 2011; Zhao and Running 2010; Zscheischler et al. 2014). However, integrating ecological processes of how ecosystems functionally respond to extreme droughts have not been broadly considered in identifying drought impacts. Thus, the patterns of extreme ecological responses to droughts have not been well quantified globally from the ecological perspective.

On a global scale, it is widely reported that severe droughts caused by precipitation reduction can induce extensive plant mortality and an associated reduction in productivity (Allen et al. 2010; Doughty et al. 2015; Peng et al. 2011). How ecosystems respond to greater precipitation variability is a new frontier for ecologists (Knapp et al. 2017; Luo et al. 2017). Generally, ecosystems are composed of plant communities that

have adapted to current water conditions to be fully functional under a wide range of conditions. Thus, ecosystems can withstand the effects of moderate water shortage and sustain productivity by increasing plant water-use efficiency through the closure of stomata or favoring high water-use efficiency species, and less water is lost through runoff and evaporation (Mariotte et al. 2013; Ponce Campos et al. 2013). However, when water shortage becomes more severe (i.e. extreme drought), more water could be lost through evaporation resulting from increasing ratio between evaporation and carbon uptake or plant mortalities due to carbon starvation or hydraulic failure) (Choat et al. 2012; McDowell et al. 2008). Thus, loss of ecosystem function could occur when the plant communities are not able to use the existing water resources to maintain resistance (e.g. increasing water-use efficiency) during extreme drought. And there must exist thresholds at which ecosystems function turns to decline in extreme drought, which is still largely unknown and has great scientific significance (Estiarte et al. 2016).

Here, we developed a new method to detect the extreme drought-induced loss of ecosystem function globally from an ecological perspective. In this study, rain-use efficiency (RUE; GPP/precipitation) was utilized as the typical indicator of ecosystem function. We assumed that RUE increases with decreasing precipitation to a maximum (RUE_{max}) during moderate drought (Huxman et al. 2004; Ponce Campos et al. 2013), and that RUE will decline when water shortage is beyond the tolerance of current vegetation, leading to loss of ecosystem function. The main objective of this study was to detect the ecological patterns of extreme drought-induced loss of ecosystem function globally for the beginning of this century (2001-2011) and understand its implications for the carbon cycle. Three global GPP datasets were used to establish three RUE datasets and each RUE

dataset was used to detect loss of ecosystem function individually. The spatiotemporal extent of ecosystem function loss and its impact on the terrestrial carbon cycle were further analyzed in this study.

3.2 Materials and methods

3.2.1 Data sources

We used three different GPP datasets and a precipitation dataset to establish three global RUE datasets. All datasets used are listed in Table 3.1.

The MODIS GPP product (MOD17.055) was produced by the Numerical Terradynamic Simulation Group (NTSG)/University of Montana (UMT) (http://www.ntsg.umt.edu/project/mod17). It provides monthly GPP data with a 0.05° spatial resolution for the period 2000-2015 (Zhao and Running 2010). This product was developed from production efficiency model using MODIS vegetation indices and meteorological information as inputs. Its accuracy has been independently assessed for scientific research and it is a primary data source used to evaluate the spatial distribution and long term trend of vegetation productivity (Anav et al. 2015).

The BESS GPP product was generated from a simplified process-based model (Breathing Earth System Simulator) which couples atmosphere and canopy radiative transfers, photosynthesis, evapotranspiration, and energy balance (Jiang and Ryu 2016). It provides monthly GPP data at 0.5° spatial resolution from 2001 to 2015 (http://environment.snu.ac.kr/bess/). This new process model-based GPP product serves as a dataset independent from remote sensing and ground observations.

The MPI-BGC GPP product from the Max Planck Institute for Biogeochemistry were up-scaled from ground FLUXNET observations of CO_2, water, and energy fluxes

to global scale using the model tree ensemble (MTE) technique (Jung et al. 2011). The MTE model was first trained to predict site-level GPP based on remote sensing indices and meteorological data, and then it was applied globally to generate GPP at a 0.5 ° spatial resolution and a monthly temporal resolution from 1982 to 2011 (http://www.bgc-jena.mpg.de/geodb/). As a proxy for FLUXNET observations, this empirically derived GPP product has been commonly considered as the benchmark or reference for calibration and evaluation of other model results (Anav et al. 2015; Piao et al. 2013). Nevertheless, large uncertainties still exist in the regions with few observation stations (e.g. South America, Africa).

The global gridded precipitation dataset used in this study was from Climate Research Unit (CRU), version TS 3.24.01 (Harris et al. 2014). It provides monthly precipitation at 0.5° spatial resolution spanning from 1901 to 2015 (https://crudata.uea.ac.uk/cru/data/hrg/). The global precipitation dataset is based on analysis of more than 4000 individual meteorological station records and spatially interpolated using autocorrelation functions. This precipitation product has been widely evaluated and used in global change studies (de Jong et al. 2013; Wu et al. 2015).

Table 3.1 Datasets used in this study.

Variable	Description	Temporal resolution	Spatial resolution	Reference
MODIS GPP	Gross primary productivity derived from MODIS (MOD17.055) remote sensing observations	Monthly 2000-2015	0.05°	(Zhao and Running 2010)
BESS GPP	Gross primary productivity derived from process-based model	Monthly 2001-2015	0.5°	(Jiang and Ryu 2016)
MPI-BGC GPP	Gross primary productivity derived from ground FLUXNET observations	Monthly 1982-2011	0.5°	(Jung et al. 2011)

CRU PRE	Precipitation from CRU TS 3.24.01 (Climatic Research Unit at the University of East Anglia)	Monthly 1901-2015	0.5°	(Harris et al. 2014)

3.2.2 Rain-use efficiency datasets

In our study, the common time period of the three GPP datasets (2001-2011) was chosen as the study period. The MODIS GPP product were aggregated to a 0.5 ° spatial resolution to match the other two GPP datasets. The monthly data of all three GPP datasets were respectively summed annually to estimate the annual GPP datasets. In order to match the three GPP datasets, monthly precipitation data were also summed annually for 2001-2011.

Based on the definition of rain-use efficiency (productivity per unit of precipitation, $gC/mm/m^2$), three annual GPP datasets were divided by the annual precipitation dataset to generate three global RUE datasets (MODIS RUE, BESS RUE, and MPI-BGC RUE) at 0.5° spatial resolution during 2001-2011. Due to the longer-time data availability of MODIS GPP and BESS GPP, we also generated an annual average RUE dataset (AVE RUE) for 2001-2015 using the average of MODIS GPP and BESS GPP for longer term analysis.

3.2.3 Detecting ecosystem function loss

For each RUE dataset during 2001-2011, the detection of ecosystem function loss was implemented pixel by pixel globally based on the relationship between RUE and precipitation. For each pixel, we assumed that the RUE of an ecosystem increases gradually to a maximum (RUE_{max}) as precipitation decreases, and then declines when the water shortage exceeds the plant community tolerance (ecosystem resistance) to the

extent that ecosystem function declines. To characterize ecosystem responses to extreme drought, we first identified RUE_{max} during the study period. Numerically, we identified the greatest value of the 11-year RUE estimates as the RUE_{max}. Then, the precipitation at RUE_{max} was selected as a threshold at which abrupt changes in ecosystem function could occur with further precipitation reductions. Using this threshold, each RUE dataset was separated into two parts at the pixel level: 1) Data with precipitation at or above the threshold for normal years; and 2) data with precipitation below the threshold for possible drought years. For the data points in normal years, the precipitation and corresponding RUE estimates were used to build a linear regression model (Figure 3.1). The regression model was further extended to data points below the precipitation threshold in drought years with 95% confidence bound. If the data points during drought years were below the lower 95% confidence bound of the regression (the lower limit of ecosystem variability), loss of ecosystem function had occurred (Figure 3.1). This algorithm was applied to obtain the global spatial patterns of ecosystem function loss for 2001-2011 and 2001-2015, respectively.

In this study, only the pixels with more than 6 data points (8 data points for 2001-2015) in normal years were selected to build the linear regression model, since this represents the majority of years in the study period (Figure S3.1). Furthermore, only the pixels with statistically significant regressions between RUE and precipitation ($p < 0.05$) were used to identify ecosystem function loss (Figure S3.1 and Figure S3.2). Overall, more than 85%, 91%, and 82% of the earth vegetated land surface, respectively, in MODIS RUE, BESS RUE, and MPI-BGC RUE datasets showed significant correlations

between RUE and precipitation. Thus, more than 80% of the vegetated land was available to analyze the global patterns of extreme drought-induced ecosystem function loss.

3.2.4 Estimation of GPP reduction and its spatiotemporal variation

In this study, for each pixel, the years with ecosystem function losses were detected and recorded based on the method shown in Figure 3.1. Using the average of GPP values in non-drought years as the baseline, the GPP reduction due to ecosystem function loss in each pixel was calculated as the difference of the GPP value of current drought year and the baseline. Through the spatial integration of GPP reduction pixel by pixel, annual regional and global GPP reductions could be estimated. To evaluate the impact of ecosystem function loss on the terrestrial carbon cycle, the GPP reduction was then compared with the GPP anomaly in drought-affected areas. Additionally, we also estimated the GPP reductions across biomes to analyze the extreme drought impacts on different terrestrial ecosystems.

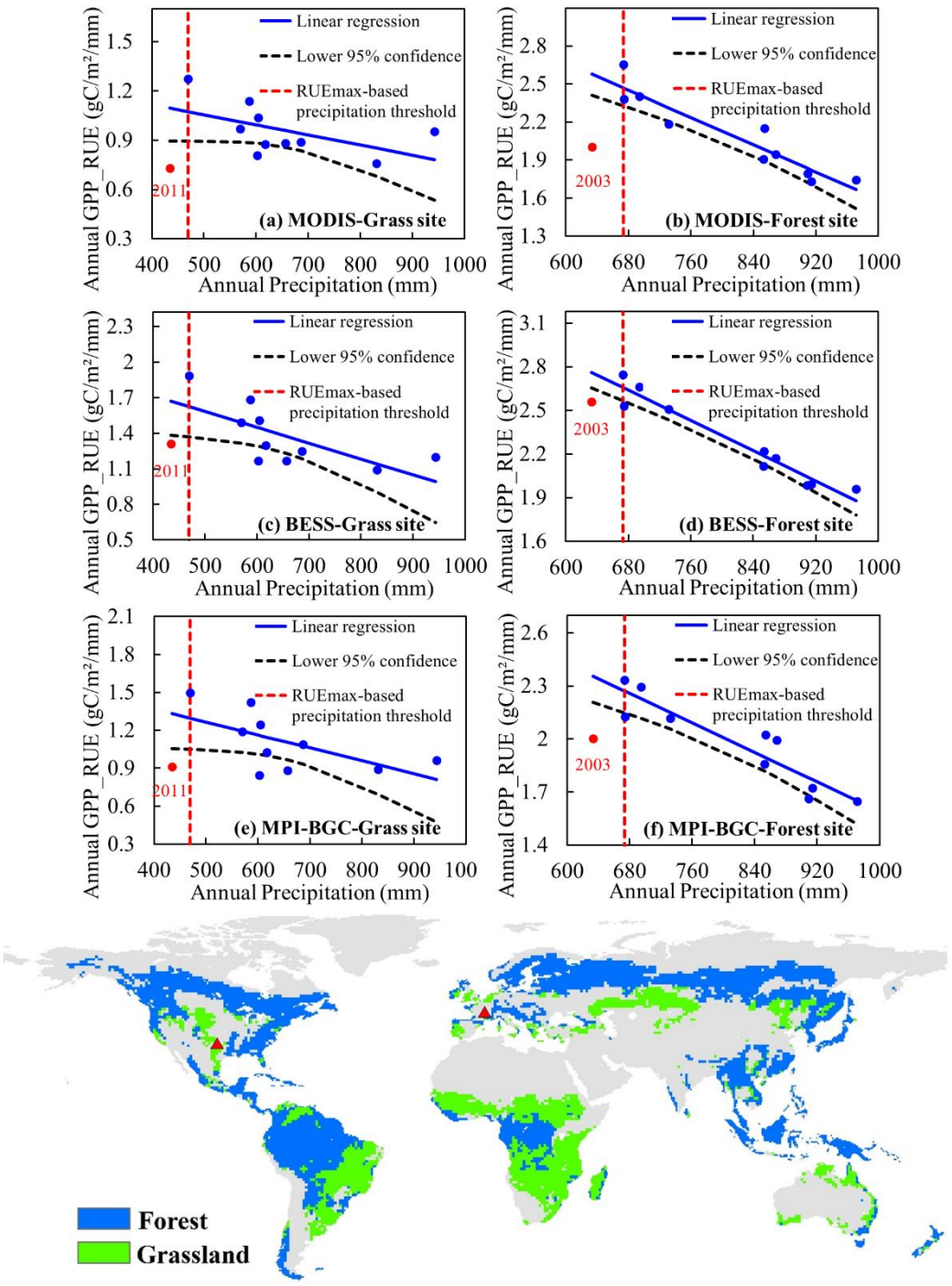

Figure 3.1 Examples of ecosystem function loss at a forest site and a grassland site for 2001-2011 using MODIS RUE (a, and b), BESS RUE (c and d), and MPI-BGC RUE (e and f) datasets respectively. The forest site was in Europe (3.54° N, 46.48°E) while the grassland site was in southern U.S. (36.23°N, 98.74°W) (Red triangles). The distribution of forest and grassland was based on Commonwealth Scientific and Industrial Research Organisation (CSIRO) vegetation types used by Community Atmosphere Biosphere Land Exchange (CABLE) model. Red dashed lines represent the precipitation threshold based on the maximum of RUE (RUE_{max}), blue solid lines

represent the linear regression models built using data points in normal years, black dashed lines represent the lower 95% confidence boundary of the regression, and blue points represent data points in normal years while red points represent data points in possible drought years. The red points that fall below the lower 95% confidence boundary were identified as ecosystem function losses (data points 2011 and 2003).

3.3 Results

3.3.1 Precipitation threshold of ecosystem function loss based on RUE_{max}

The precipitation at RUE_{max} was selected as the threshold at which abrupt alteration of ecosystem function could occur with further water shortage. In each pixel, the greatest value of RUE estimates (RUE_{max}) was first identified during 2001-2011 and then the precipitation at the RUE_{max} was recorded as the threshold. The spatial distributions of the precipitation threshold in 2001-2011 were extracted based on three RUE datasets respectively (Figure 3.2). The general patterns of the precipitation threshold were similar in all three RUE datasets. For example, the precipitation thresholds at the forest site in Europe (3.54° N, 46.48°E) were identified as 673.4 mm in three datasets, and the precipitation thresholds at the grassland site in southern U.S. (36.23°N, 98.74°W) were identified 469.1 mm in three datasets (Figure 3.1).

At the global scale, the distribution of the precipitation threshold follows a latitudinal gradient. It decreases from low latitude to high latitude and from wet areas to dry areas. In addition, the spatial variation of the precipitation threshold largely depends on the distribution of land cover types. Tropical forest areas, e.g. the Amazon, have the highest precipitation threshold, which could be more than 1600 mm/yr. However, the precipitation threshold in semi-arid and arid areas could be as low as 200 mm/yr, e.g. Northwestern China, where shrubland and grassland are largely distributed.

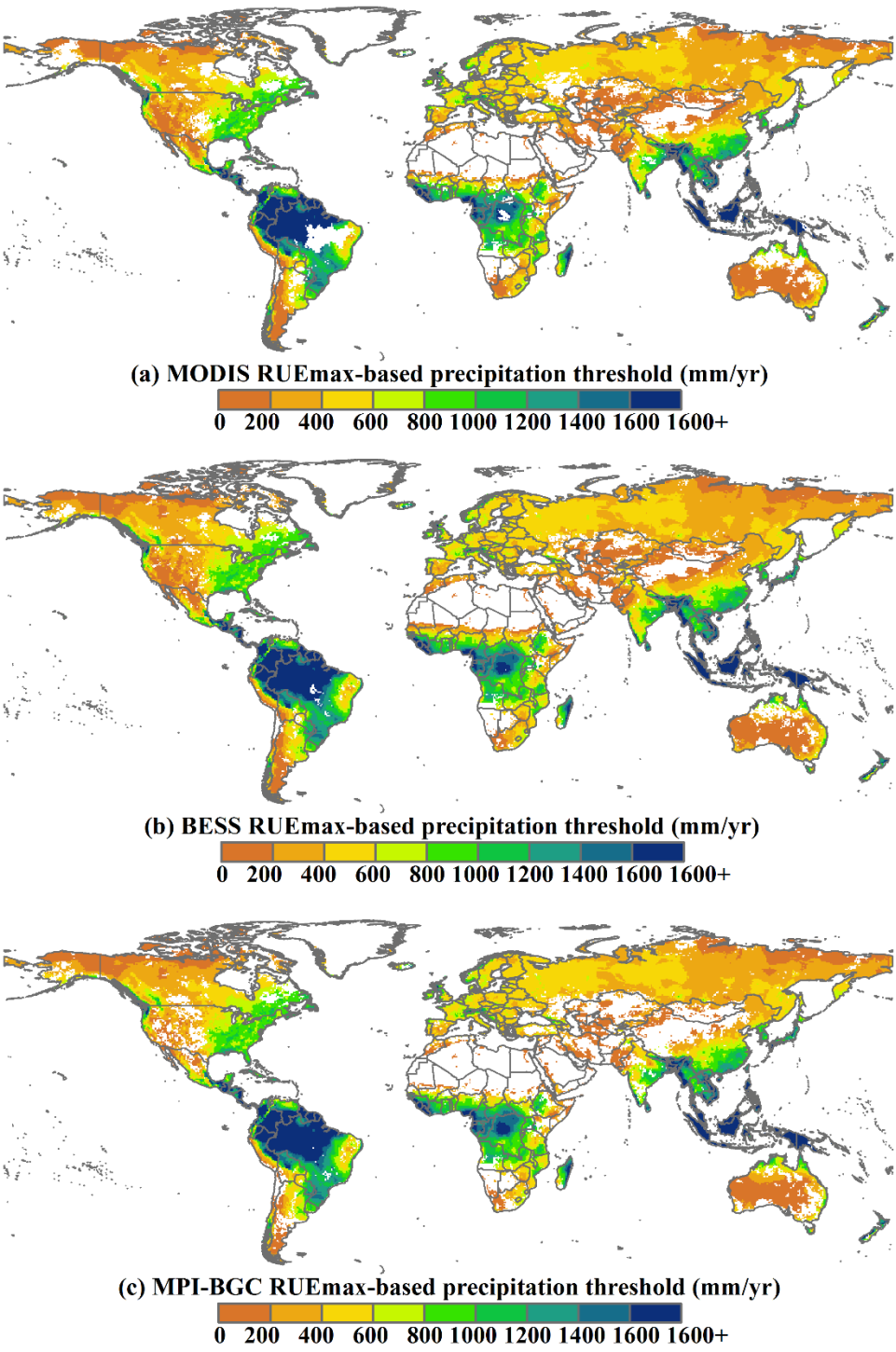

Figure 3.2 Spatial distribution of precipitation thresholds based on maximum rain-use efficiency (RUE_{max}) during 2001-2011 using MODIS dataset (a), BESS dataset (b), and MPI-BGC dataset (c). Extreme drought-induced ecosystem function loss is expected to occur if the precipitation in a given year decreases below the threshold on the map.

3.3.2 Spatial distributions of extreme drought-induced loss of ecosystem function

In this study, annual global distributions of ecosystem function loss due to extreme drought were captured during 2001-2011 based on MODIS, BESS, and MPI-BGC datasets. Additionally, the driest year of ecosystem function loss with the largest deviation from the regression model was also identified in each pixel for each GPP dataset, representing the most extreme loss of ecosystem function (Figure 3.3). Large well-known extreme drought events during 2001-2011 were successfully captured in all three RUE datasets (Figure 3.3). Extreme drought-induced loss of ecosystem function was mainly concentrated in semi-arid regions. For example, the 2001 seasonal drought in North China (Liu et al. 2014), the prolonged droughts around 2002 in central North America (Michaelian et al. 2011; Schwalm et al. 2012), the 2003 Europe drought induced by heat wave (Ciais et al. 2005), the 2010 drought in Russian (Barriopedro et al. 2011), and the 2011 Southern Great Plains drought in the U.S (Tadesse et al. 2015). In particular, the 2010 Russian drought was identified as the largest ecological response to extreme drought in the study period, which caused approximately 520,000 km^2 of area to lose function on average, over 60% of which was cropland. Based on the global patterns of ecosystem function loss for the period of 2001-2015 (Figure S3.3), more recent extreme drought events with ecosystem function loss were also captured, such as the 2012 drought in northern central U.S. following the 2011 drought in southern U.S. (http://www.ncdc.noaa.gov/sotc/briefings/201209.pdf), and the 2015 drought in Europe after the 2003 drought (Ionita et al. 2017).

We quantitatively compared the distribution and years of ecosystem function loss in this study with the drought-induced plant mortality events reviewed in Allen et al.

(2010) before 2010 for validation (Table S1). We overlapped 42 forest mortality cases occurred in 1999-2010 from Allen et al. (2010) with our results (Figure S3.4). Specific latitude and longitude information for each mortality case were collected based on references noted in Allen et al. (2010). For those drought cases without exact latitude and longitude, we located their position by using the specific name of the drought location and Google Earth. Generally, our method matched the extreme droughts very well in Asia (e.g. North China, 2001), Europe (e.g. Central Europe, 2003) and North America (e.g. Central North America, 2002), where the drought year of major ecosystem function loss in this study was within the range of documented years of drought-induced plant mortality events in Allen et al. (2010) (Table S3.1). However, in this study, the tropical forest areas did not show much extreme drought signal, e.g. the Amazon drought in 2005 and 2010 were not well detected.

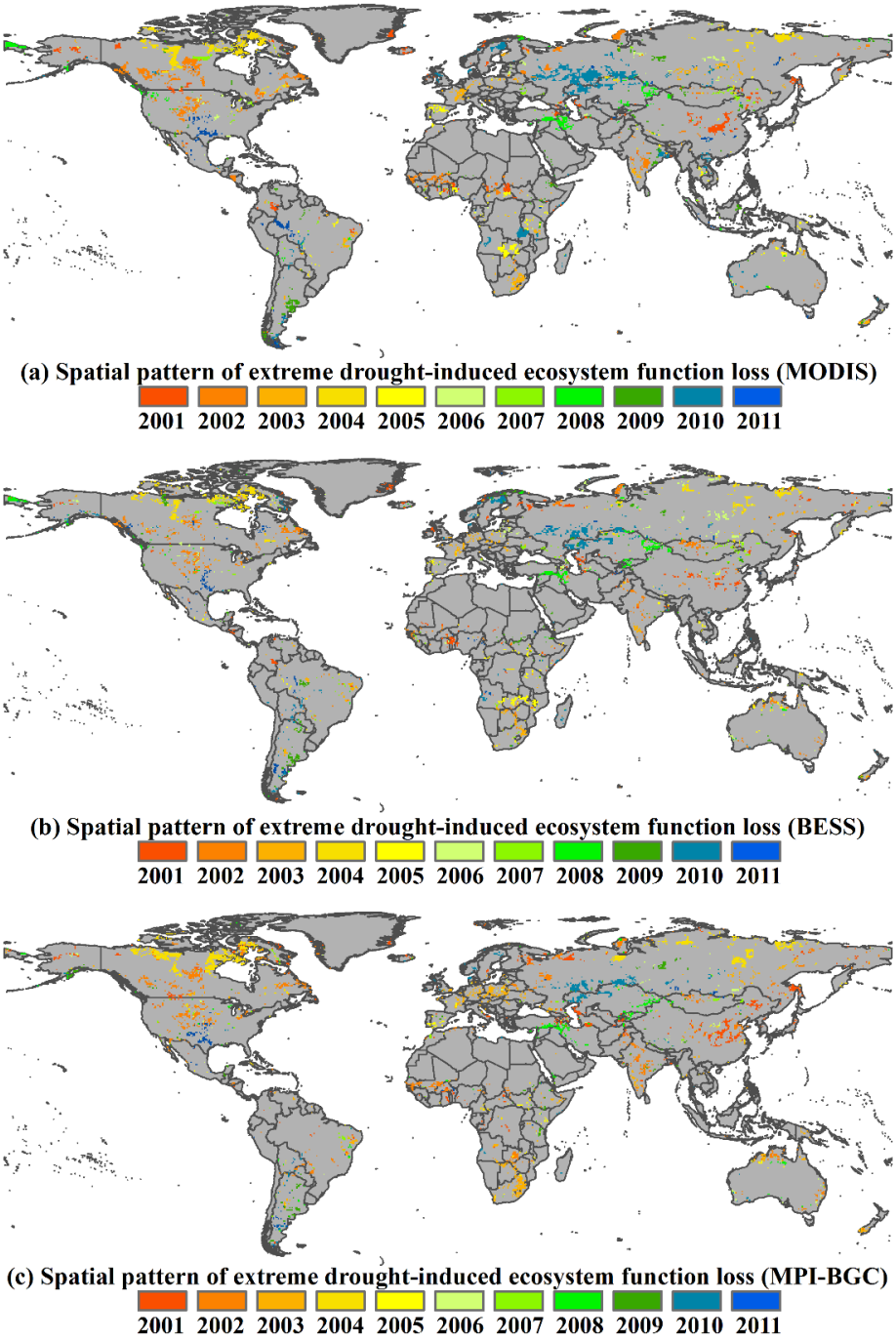

Figure 3.3 Spatiotemporal distribution of extreme drought-induced loss of ecosystem function during 2001-2011. Each color on the maps represents the driest year of ecosystem function loss with the largest deviation from the regression model. Extreme droughts in North China (2001), central North America (2002), central Europe (2003), western Russia (2010), and southern U.S. (2011) stand out as exceptional instances of ecosystem function loss in the MODIS (a), BESS (b), and MPI-BGC (c) datasets.

3.3.3 Spatiotemporal variation of ecosystem function loss and its impact on carbon cycle

In the study period of 2001-2011, extreme drought-induced loss of ecosystem function affected 8%±1% of global vegetated land area (9.28±1.33 million km^2), an area roughly the size of China, which resulted in GPP reduction of 1.5±0.3 PgC in total. Here, the vegetated land area estimated in this study was ~120 million km^2. On average, up to 0.9%±0.1% of earth's vegetated land (1.13±0.17 million km^2) experienced loss of ecosystem function and 0.14±0.03 PgC GPP was reduced per year. Thus, there was an average decrease in carbon uptake of 120.5 ± 9.9 $gC/m^2/yr$. In this study, 2002 and 2010 were shown as the major ecological drought years based on the three RUE datasets (Figure 3.4a-b), which were mainly attributed to the loss of ecosystem function in central North America (2002) and the droughts in Russia (2010) respectively. In addition, we also analyzed the annual drought-affected area and GPP reduction at the biome level (Figure 3.4c-d). Based on the results from the three RUE datasets, cropland and C3 grassland showed relatively high values of affected area and GPP reduction while deciduous needle leaf forest (DNF) and shrubland displayed the lowest values of affected area and GPP reduction.

Ecosystem function loss was distributed mostly in semi-arid regions and exhibited strong interannual variation. We compared the variation in GPP reduction with the variation in GPP anomaly in drought-affected areas (8%±1% of vegetated land area). The GPP reductions estimated from the three GPP datasets all showed significant correlation with their GPP anomalies (R^2=0.70~0.91, $p \leq 0.001$) (Figure 3.5). Additionally, the GPP reduction during 2001-2015 based on the average of MODIS GPP and BESS GPP also

showed significant correlation with its GPP anomaly in drought-affected areas (R^2=0.60, p<0.001).

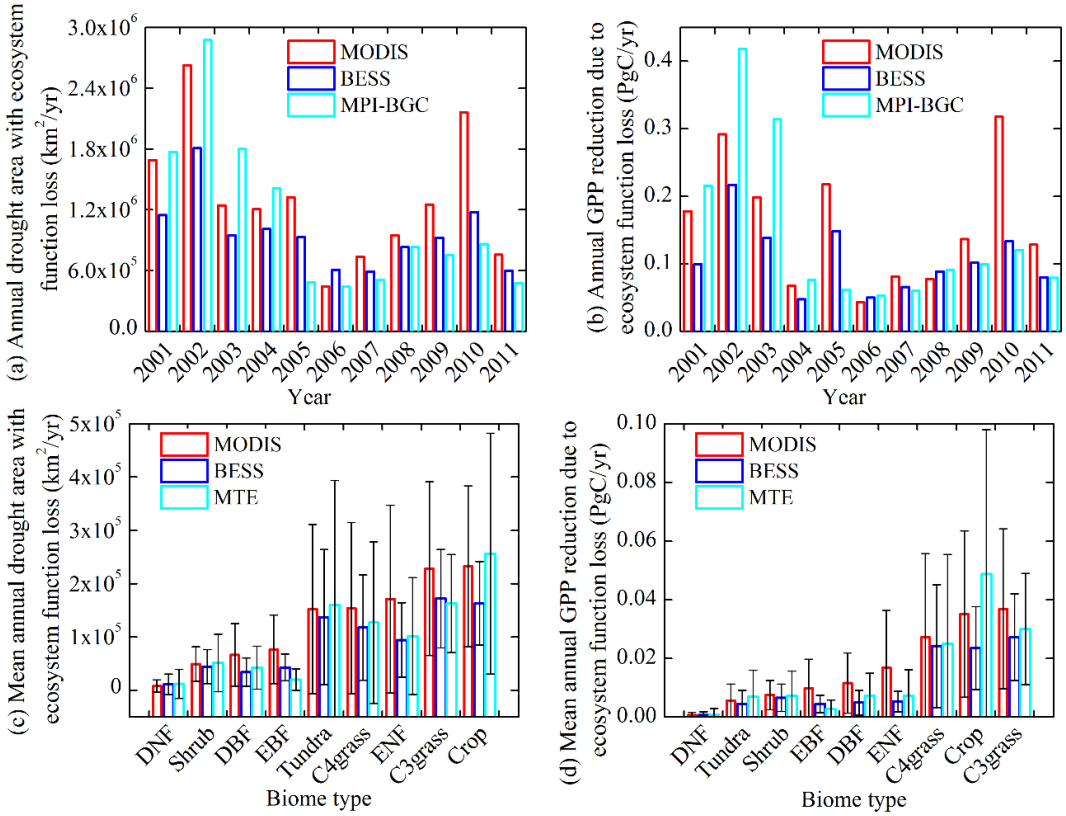

Figure 3.4 Mean drought-affected area and GPP reduction caused by ecosystem function loss at annual global scale (a and b) and biome level (c and d) based on three GPP products.

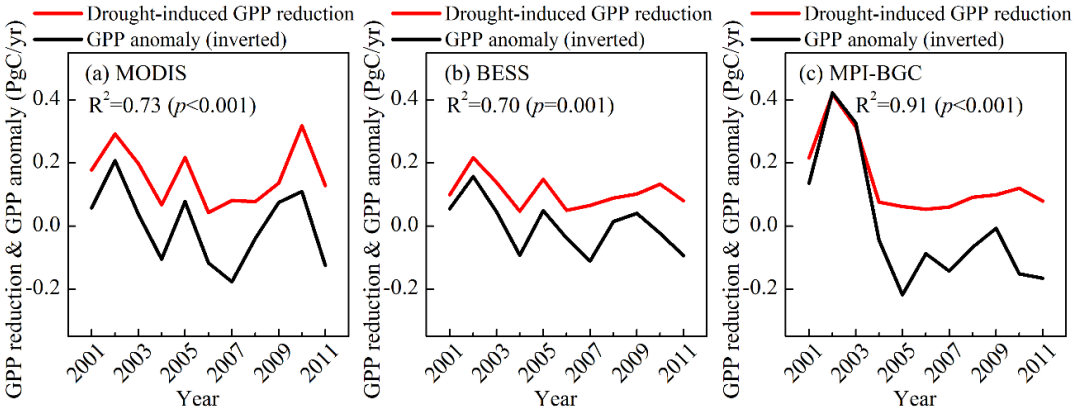

Figure 3.5 Interannual variation in GPP reduction (Red lines) and inverted GPP anomaly (Black lines) in drought-affected areas from 2001 to 2011. GPP reductions and anomalies were estimated from MODIS datasets (a), BESS datasets (b), and MPI-BGC datasets (c) respectively. GPP anomaly in each year was calculated as the

difference of the GPP value of current year and the average of the study period. R^2 is the determination coefficient which represents the percentage of GPP anomaly explained by reduced carbon uptake due to drought.

3.4 Discussion

3.4.1 Advantages and limitations of the method

In this study, the relationship between RUE and precipitation was used to identify the global patterns of extreme drought-induced ecosystem function loss. Based on this, the impacts of ecosystem function loss on carbon uptake were further analyzed. Our detection of losses of ecosystem function was based on the assumption that RUE of an ecosystem increases to a maximum during moderate drought and then declines during extreme drought, which is more ecologically relevant than traditional approaches which rely on meteorological variables and statistical techniques and can further improve our understanding of ecosystem responses to climate extremes (Ciais et al. 2005; Hoover et al. 2014; Liu et al. 2013; Zhao and Running 2010; Zscheischler et al. 2014). Our results showed that semi-arid regions were hot spots of ecosystem function loss. There was an average decrease in carbon uptake of 120.5±9.9 $gC/m^2/yr$, which is comparable with multi-year regional averages of drought impact in western America of 116 $gC/m^2/yr$ (Schwalm et al. 2012) and in Europe of 195 $gC/m^2/yr$ (Ciais et al. 2005). The reduced carbon uptake due to ecosystem function loss could strongly influence the regional carbon cycle. The simplicity of the method and integration of an ecological perspective to identify climate extremes are the primary advantages of this study.

In our method, the lower 95% confidence bound of a regression model estimated during normal conditions was used to identify the ecosystem function loss induced by extreme drought, which fits the definition proposed by Smith (2011) of "an extreme

climatic event is an episode or occurrence in which a statistically rare or unusual climatic period alters ecosystem structure and/or functions well outside the bounds of normal variability" (Smith 2011). In addition, the exploration of precipitation thresholds provides useful information for the setup of field rainfall manipulation experiments (Figure 3.2). For example, at a given location, we provide references for what level of precipitation could be set as the extreme drought condition in a gradient precipitation experiment. While these thresholds are merely starting points with little published literature to compare with, Verbesselt et al. (2016)found a threshold for ecosystem collapse in Amazon forests during drought to be 1500 mm/yr, which is comparable with the precipitation threshold identified in our study (more than 1600mm/yr) (Verbesselt et al. 2016). Using RUE as a metric of ecosystem function, we were also able to connect the estimates derived from remote sensing and model simulations to field experiments where RUE is most commonly used (Huxman et al. 2004; Yan et al. 2014; Yang et al. 2010).

Significant relationships between RUE and precipitation ($p<0.05$) were found in more than 80% of earth's vegetated area, and were further used to analyze ecosystem function loss. Most of the insignificant ($p\geq0.05$) RUE-precipitation relationships were concentrated in semi-arid regions. Irrigation, which is quite common in semi-arid regions (e.g. Central U.S. and Inner Mongolia, China), could be one of the reasons for insignificant regressions. Also, the accuracy of precipitation data in those regions needs to be improved (Schneider et al. 2013). In this study, short-term, seasonal droughts within a year may not be well detected from the relationship between RUE and precipitation since these variables are estimated at the annual scale. Moreover, in Figure 3.1, a spurious pattern could emerge in the correlation between RUE and precipitation if GPP and

precipitation were unrelated in this study (Brett 2004). All global estimates in our results could be conservative due to the limitations in the method and the available analyzed pixels (Figure S3.1).

3.4.2 Well-known extreme drought events in this study

Ecosystem function loss was detected in many well-known extreme drought events, especially in semi-arid areas (e.g. central North America, central Africa, and northwestern China, where cropland and C3 grassland are largely distributed) (Figure 3.3). However, for tropical areas, e.g. Amazon forest, we didn't see much extreme drought signal (e.g. 2005 drought or 2010 drought) from any of the three GPP RUE datasets, which could also result in underestimation of ecosystem function loss in this study. Because of the cloudy weather in tropical areas, optical remote sensing images usually have low quality, which may impact the quality of GPP derived from remote sensing (Anav et al. 2015). For the up-scaled GPP from FLUXNET, due to the few flux towers located in tropical forests, high error exists in the GPP estimates (Kumar et al. 2016). Additionally, process model-based GPP simulations in tropical areas still remains a challenge due to the uncertainty caused by climatic forcing data (Wu et al. 2017). In this study, tundra areas also showed a strong signal of ecosystem function loss, especially in 2004 (Figure 3.3). Due to large amounts of peatland distributed in tundra, fire frequently occurs in the dry season (Mack et al. 2011). The high carbon content of the peatland may largely contribute to the fire occurrence in association with extreme drought (Turetsky et al. 2014). In this study, those fire occurrences were recognized as ecosystem function loss due to extreme droughts, as drought likely initiated higher fire probability. For cropland, human management also has strong influence on the production of plants (i.e. harvest) and may

thus influence drought detection. However, we didn't remove the cropland in this study. Usually, at a cropland site, the timing of seeding, growing and harvesting remains the same, thus the GPP estimates of this site are still comparable at the annual scale.

3.4.3 Implication of ecosystem function loss on carbon cycle

In this study, semi-arid regions were shown to be hot spots of ecosystem function loss, and contributed to more than 70% of the annual GPP variation in drought-affected areas (Figure 3.5). However, the extreme drought-induced ecosystem function loss was found to have little impact on global GPP variability. In semi-arid regions, GPP variability is strongly controlled by precipitation variability, which could be one of the reasons that local ecosystems are more predisposed to loss of ecosystem function. Also, studies have shown that the productivity in semi-arid regions strongly contributes to the interannual variability of global GPP or NPP (Huang et al. 2016; Zhang et al. 2016c). In our results, even though 0.14±0.03 PgC/yr GPP reduction due to ecosystem functional loss didn't show a strong impact on the global carbon cycle (results not shown), it was still a major threat at the regional scale and could potentially influence the global carbon cycle. No increasing trend of GPP reduction was found in this study, and there was even a decreasing trend in ecosystem function loss from 2001 to 2015 (Figure S3.5). The continually increasing atmospheric CO_2 concentration may stimulate higher water-use efficiency of ecosystems despite the warming during the period (Keenan et al. 2013). However, as ecosystem function loss still largely depends on the climate variability, considering the increasing precipitation variability and expansion of dry land (Huang et al. 2015), extreme drought-induced ecosystem function loss may have a larger effect on the future of regional and global carbon cycles.

3.5 Conclusion

Quantifying the ecological patterns of extreme drought-induced ecosystem function loss is an important first step to understand how ecosystems respond to ecological drought against the background of climate change. Here, we developed a novel method based on plant community rain-use efficiency to detect ecosystem function loss globally. We produced spatial patterns of extreme drought-induced ecosystem function loss during 2001-2011 based on three different GPP products. Large well-known extreme drought events with ecosystem function loss were well captured in semi-arid regions. Extreme drought-induced loss of ecosystem function could explain more than 70% of the GPP variability in drought-affected areas. Our study demonstrates the importance of semi-arid regions in terrestrial carbon cycle studies and provides a new simple way to quantify extreme droughts from the ecological perspective.

Supplementary materials

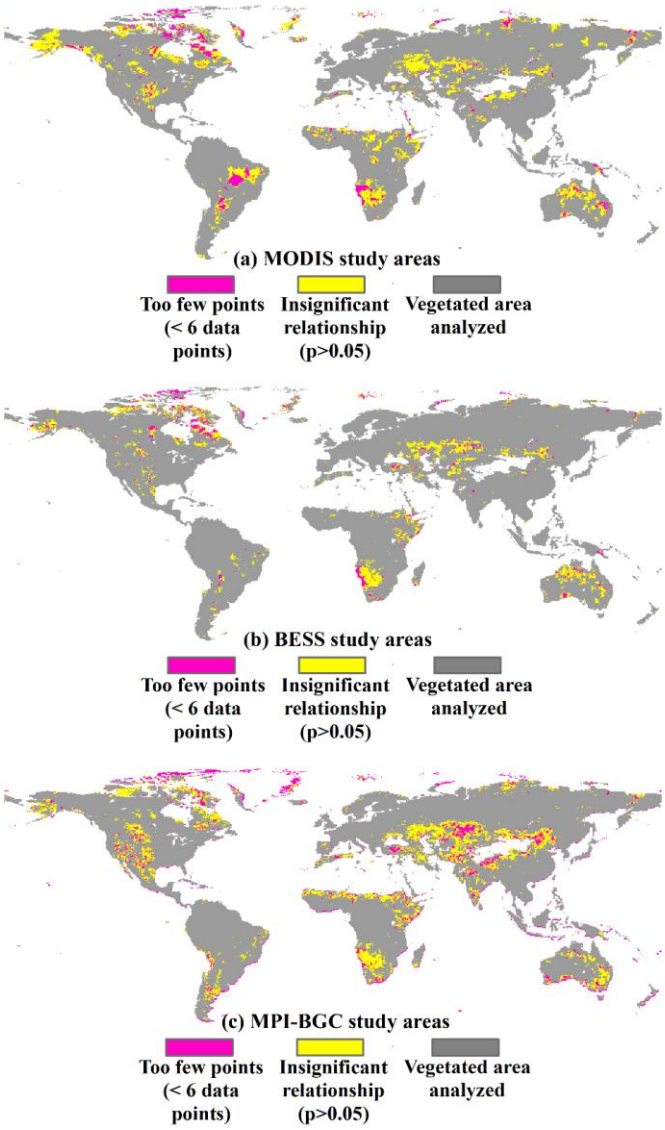

Figure S3.1 Spatial distribution of available analyzed area for each RUE dataset after masking those insignificant areas. (a) 85% of MODIS vegetated area, (b) 91% of BESS vegetated area, and (c) 82% of MPI-BGC vegetated area were analyzed respectively in this study.

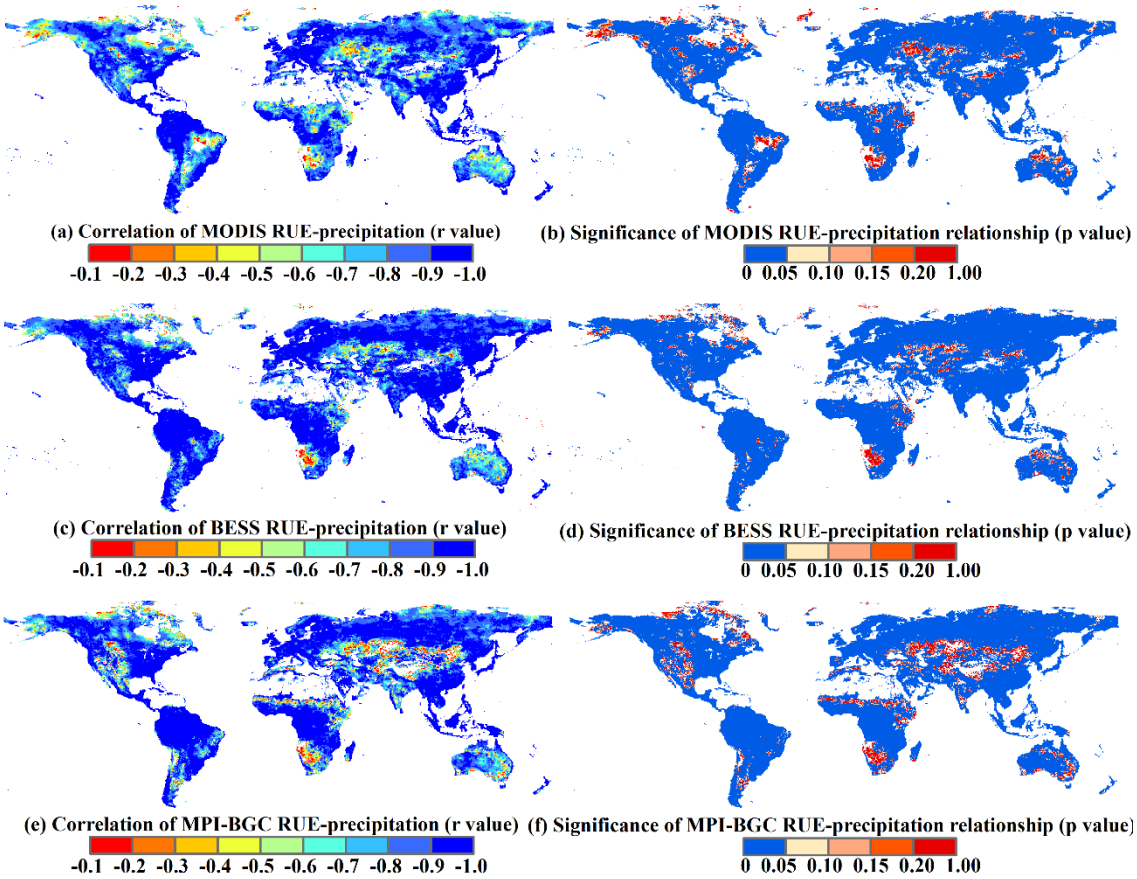

Figure S3.2 The correlation coefficient (r value) and significance level (p value) of the relationship between RUE and precipitation above the RUEmax based precipitation threshold in normal years. The r and p values of MODIS RUE dataset are shown in (a) and (b) respectively. The r and p values of BESS RUE dataset are shown in (c) and (d) respectively. The r and p values of MPI BGC RUE dataset are shown in (e) and (f) respectively.

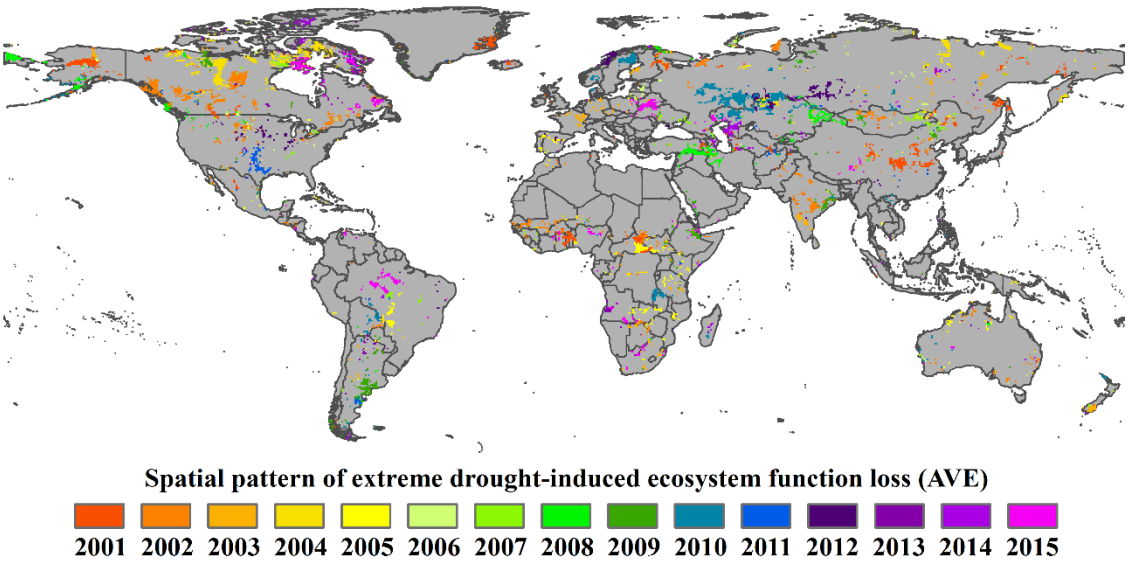

Figure S3.3 Spatiotemporal distribution of extreme drought-induced loss of ecosystem function during 2001-2015 based on average of MODIS and BESS GPP datasets. Each color on the maps represents the driest year in which a loss of ecosystem function occurred.

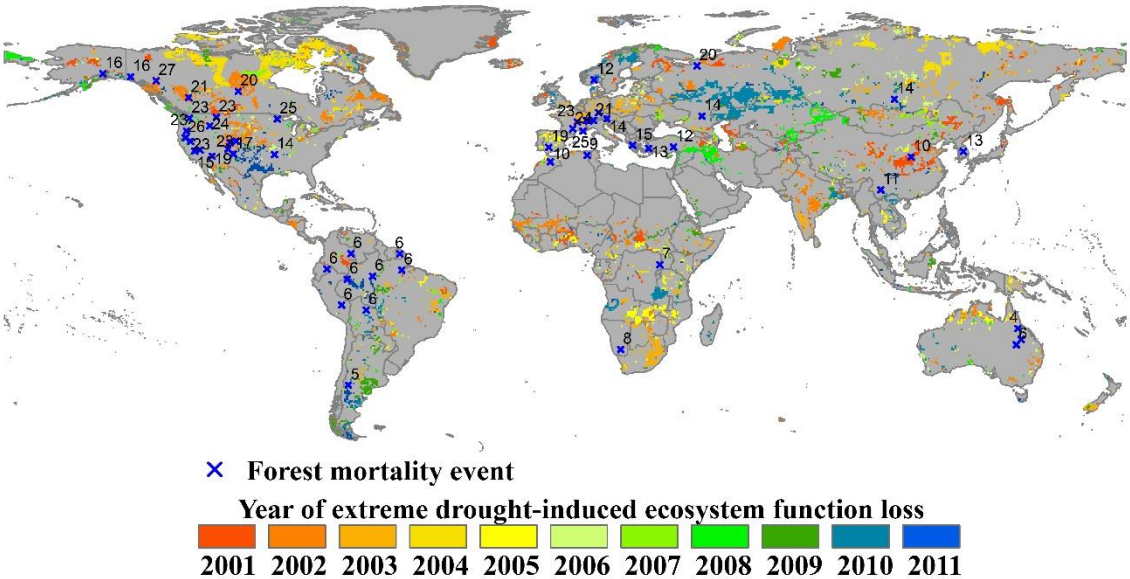

Figure S3.4 Comparison of extreme-drought induced ecosystem function loss with documented drought-induced forest mortality from Allen et al. (2010). Each color on the maps represents the driest year in which a loss of ecosystem function occurred except the blue cross signs.

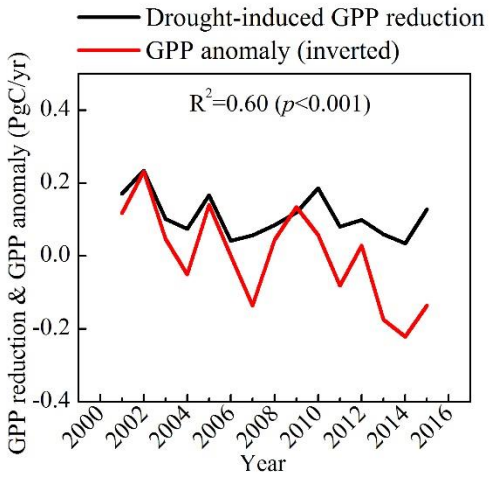

Figure S3.5 Interannual variation in GPP reduction (Red line) and inverted GPP anomaly (Black line) in drought-affected areas from 2001 to 2015. GPP reduction and GPP anomaly were estimated from the average of MODIS GPP and BESS GPP datasets. GPP anomaly in each year was calculated as the difference of the GPP value of current year and the average of the study period (2000-2015). R^2 is the determination coefficient which represents the percentage of GPP anomaly explained by reduced carbon uptake due to drought.

Table S3.1 Literature comparison with Allen et al. (2010). ID numbers refer to locations of drought-induced forest mortality events mapped in Figure S3.4.

Continent	ID	Location	Drought type	Allen et al. (2010)	This study
				Year(s) of mortality	Year of extreme ecosystem function loss
Africa	7	Uganda(Western)	Seasonal drought	1999	-
	8	Namibia, South Africa	Multi-year drought, high temperatures	1904-2002	-
	9	Algeria	Multi-year drought	2000-2008	-
	10	Morocco	Multi-year drought	2002-2008	2003
Asia	10	China(Shanxi,Hebei, Henan)	Seasonal drought	1998-2001	2001
	11	China (Yunnan)	Seasonal drought	2003-2005	2003
	12	Turkey (Central Anatolia)	Drought	2002-2007	2008
	13	South Korea	Warm winters/springs, possibly drought	2003-2008	-
	14	Russia	Drought	2005-2008	2010
Australia	4	Australia (Queensland)	Multi-year drought	1990-2002	-
	5	Australia (Queensland)	Multi-year drought	2004	-
	6	Australia (Queensland)	Multi-year drought	2005	-
Europe	12	Norway	Multi-year summer droughts, high summer temperatures	1992-2000	-
	13	Greece(Samos)	Multi-year drought	2000	-
	14	Austria(Tyrol)	Seasonal droughts	2001	2003
	15	Greece (South, Central)	Multi-year drought	2000-2002	-
	16	Switzerland	Drought, high temperatures	2003	2003
	17	Switzerland (Valais)	Seasonal and multi-year droughts, high temperatures	2000-2004	2003
	18	Germany (Baden-Württemberg)	Drought, high temperatures	2003-2006	2003
	19	Spain	Multi-year drought	2004-2006	2005
	20	Russia(Northwest)	Drought, high temperatures	2004-2006	2002
	21	Swuzerland(Grisons)	Drought, high temperatures	2003-2007	-
	22	France (Provence, Southern Alps)	Multi-year drought, high temperatures	2003-2008	-

	23	France	Spring and summer drought, scorching heat	2003-2008	2003
	24	France (Eastern Pyrénées)	Recurrent drought, high temperatures	2003-2008	2003
	25	France (Provence, Maures Mountains)	Multi-year drought	2006-2008	-
North America	14	USA (Midwest, Southeast)	Multi-year drought	1990-2002	-
	15	USA (California)	Drought, high temperatures	1983-2004	-
	16	USA and Canada (Alaska, Yukon)	Drought, high summer temperatures	1989-2004	2001
	17	USA (Southwest)	Multi-year drought	2000-2004	2002
	18	Southwest, USA (New Mexico, Arizona, Colorado, Utah, Nevada)	Multi-year drought, high spring and summer temperatures	2000-2004	2002
	19	USA (Arizona)	Multi-year drought, high temperatures	2001-2004	2002
	20	Canada (Saskatchewan and Alberta)	Multi-year drought	2002-2004	2002
	21	Canada (British Columbia)	Drought, high spring and summer temperatures	2000-2006	2002
	22	USA (Colorado)	Multi-year drought, high spring and summer temperatures	2005-2006	2002
	23	USA (Western States)	High temperatures	1955-2007	2002
	24	Western North America	Drought, high temperatures	1997-2007	2008
	25	USA (Minnesota)	Drought	2004-2007	2006
	26	USA (California)	Drought preceded by wet, warm episodes	2005-2008	-
	27	Canada and USA (Alaska, British Columbia)	Warmer winters and springs	1880-2008	2002
South America	5	Argentina (western Neuquén, Rio Negro)	Seasonal drought, high temperatures	1998-1999	-
	6	Amazon Basin	Single year drought	2005	-

Chapter 4: Response of underlying water use efficiency to environmental change in forests and grasslands in the Northern Hemisphere

Abstract

Analysis of ecosystem carbon and water coupling often involves a $C:H_2O$ efficiency approach based on ecosystem productivity to represent the C term and evapotranspiration or transpiration to represent the water term. Apparent underlying water use efficiency (UWUE) provides an optimal indicator of ecosystem function by incorporating the vapor pressure deficit (VPD) effect. However, its responses to environmental changes such as the increasing atmospheric CO_2 concentration or drought have not been evaluated broadly. Here, we investigated the long-term trend in annual apparent UWUE (UWUEa) across 18 forest sites and 9 grassland sites in the Northern Hemisphere using the FLUXNET2015 dataset. We attributed the variation in UWUEa to variations in potential UWUE (UWUEp) and the ratio of transpiration to evapotranspiration (T/ET). We found that forests showed increases in UWUEa, which was mostly contributed by increasing UWUEp; whereas grasslands showed no obvious changes in UWUEa or UWUEp. The T/ET of all biomes showed little changes over time. The increase in UWUEp was triggered by CO_2 fertilization and increasing VPD in forests, as well as the decreasing soil water content (SWC) in deciduous broadleaf forests. The positive effect of CO_2 fertilization on UWUEp was offset by the negative effect of increasing SWC in grasslands.

4.1 Introduction

Plants absorb CO_2 from the atmosphere during photosynthesis, at the cost of losing water through leaf stomatal. Water use efficiency (WUE), the ratio of carbon assimilation to transpiration, is a critical metric of plant function that describes the tradeoff between carbon gain and water loss in response to environmental changes (Niu et al. 2011). Plant WUE is jointly controlled by biotic (stoma aperture) and abiotic factors (environment factors) which influence the carbon uptake and transpiration. Since pre-industrial times, the atmospheric CO_2 concentration increased from ~290 ppm to 400 ppm by 2015 and is predicted to be 421-963 ppm by 2100 (Keenan et al. 2016; Stocker et al. 2013). As a result of elevated greenhouse gases, the globally averaged temperature increased by 0.85 ℃ over the period of 1880~2012 (Stocker et al. 2013). In addition, the global precipitation regime changes substantially, leading to more and more extreme drought events (Allen et al. 2010; Stocker et al. 2013). Thus, investigating the responses of WUE to different environmental factors would help understand future terrestrial carbon and water budgets in response to environmental change.

Several formulations of WUE have been established to describe the carbon-water tradeoff from the leaf to ecosystem scale (Beer et al. 2009; Law et al. 2002; Zhou et al. 2014; Zhou et al. 2017). At the leaf scale, WUE is defined as the ratio of carbon assimilation to transpiration (WUE=A/T); and at the ecosystem scale, it is represented as the ratio of gross primary production over evapotranspiration (WUE=GPP/ET) (Law et al. 2002). Given the strong effect of VPD on transpiration, Beer et al. (2009) proposed the inherent WUE (IWUE=GPP×VPD/ET) which is more stable than WUE to describe the ecosystem carbon-water coupling on daily to annual timescales. IWUE also

corresponds to the intrinsic WUE (iWUE), the ratio of carbon assimilation over stomatal conductance, at the leaf scale. However, IWUE and iWUE rely on an assumption that the ratio of inner leaf CO_2 concentration to the ambient CO_2 concentration (c_i/c_a) is relatively constant. Some studies found that the c_i/c_a varies with VPD at diurnal and seasonal timescales and hence has nonlinear effect on IWUE (Lloyd 1994; Zhou et al. 2014). Given the nonlinear effect of VPD on c_i/c_a, Zhou et al. (2014) introduced the underlying water use efficiency ($UWUE=GPP\times VPD^{0.5}/ET$), by combing IWUE and an optimal relationship between c_i/c_a and VPD from Lloyd (1994), which is more stable and physiological relevant than other WUE formulations at sub-daily and daily timescales (Zhou et al. 2015). UWUE assumes that T dominants ET at the ecosystem scale. Hence, the ecosystem UWUE, or apparent UWUE (UWUEa), can be separated into two components: potential WUE ($UWUEp=GPP\times VPD^{0.5}/T$) which is only sensitive to atmospheric CO_2 concentration and plant functional type, and a ratio, T/ET, which is controlled by both physiological (e.g. leaf area index) and environmental factors (Zhou et al. 2017; Zhou et al. 2016).

Many studies have reported the responses of ecosystem WUE or IWUE to elevated atmospheric CO_2 concentration in forests using flux tower measurements, tree ring isotope measurements, or process-based models (Cheng et al. 2017; Frank et al. 2015b; Keenan et al. 2013; Peters et al. 2018; Wang et al. 2018). Less is known about grassland responses of WUE to the atmospheric CO_2 concentration. By regulating the stomatal aperture, plants are expected to benefit from the elevated atmospheric CO_2 concentration by enhancing the photosynthesis at a lower rate of water loss, which leads to an increased WUE or IWUE (Keenan et al. 2013; van der Sleen et al. 2014). In addition

to atmospheric CO_2, WUE is also impacted by other climate or environmental drivers (e.g. water availability, temperature, and nutrients). WUE is expected increase by partial stomatal closure during drought to limit the water loss at the expense of a reduced carbon uptake in photosynthesis, which has been observed using isotope measurements (Peters et al. 2018). However, due to the nonlinear effect of c_i/c_a on carbon assimilation, the results relying on responses of WUE or IWUE to each environmental factor are not well understood. Zhou et al. (2017) investigated the long-term trend in global UWUEa and separately attributed its variation to variations in UWUEp and T/ET using model outputs. They found that the increase in UWUE was mostly attributed to the increasing UWUEp, which was ultimately triggered by increasing atmospheric CO_2, followed by the positive trends in nitrogen deposition and climate. However, the responses of UWUE to environmental change have not been investigated using the eddy covariance (EC) flux tower observations.

The aim of this study is to investigate the responses of UWUEa to environmental changes across forests (deciduous broadleaf forests (DBF) and evergreen needleleaf forests (ENF)) and grasslands (GRA) sites in the Northern Hemisphere using FLUXNET2015 dataset which provides long-term records of CO_2 and H_2O exchanges and environmental factors. We separated the UWUEa into two components: UWUEp and T/ET and analyzed their long-term trends. We further attributed the variations in UWUEp and T/ET to variations in vapor pressure deficit (VPD), atmospheric CO_2 concentration (CO2), incoming shortwave radiation (SW), air temperature (TA), and soil water content (SWC).

4.2 Data and methods

4.2.1 EC flux tower and remote sensing datasets

We used 2000-2014 half hourly/hourly EC flux data from the FLUXNET2015 dataset (http://fluxnet.fluxdata.org/data/fluxnet2015-dataset/), including gross primary production (GPP), latent heat (LE), sensible heat (H), relative humidity (RH), vapor pressure deficit (VPD), atmospheric CO_2 concentration (CO2), incoming shortwave radiation (SW), air temperature (TA), and soil water content (SWC) of the surface soil. Only records labeled with good quality or direct measurement were used in this study.

Data screening were performed to select half hourly/hourly records following similar criteria in previous studies (Li et al. 2019; Medlyn et al. 2017; Wang et al. 2018): 1) only daytime data with incoming shortwave radiation >=50 $W \cdot m^{-2}$ and sensible heat >= 5$W \cdot m^{-2}$ were selected; 2) data during rainfall events and for 24 hours after rainfall event were excluded to minimize canopy interception evaporation; 3) data with relative humidity exceeding 95% were excluded to avoid dew evaporation; 4) negative GPP, LE, and VPD records were excluded. After the variables were selected, all half hourly data were aggregated to hourly data to reduce noise in measurements. Finally, hourly data were aggregated to means over the entire year for each site in each year. Only sites with a continual yearly estimates length ≥7 years were used for further analysis. Number of years used in each site is given in Table S4.1. In total, we identified 11 evergreen needleleaf forest (ENF) sites, 7 deciduous broadleaf forest (DBF) sites, and 9 grassland (GRA) sites from the Northern Hemisphere (Figure 4.1 and Table S4.1).

We used the satellite LAI product (MOD15A2H.006) from Moderate Resolution Imaging Spectroradiometer (MODIS) (https://lpdaacsvc.cr.usgs.gov/), which has an 8-

day, 500m resolution. The daily LAI corresponding to hourly EC flux estimates were obtained using the latest 8-day LAI for a given EC measurement day. Daily LAI obtained for hourly EC records were also averaged to generate yearly LAI for each site.

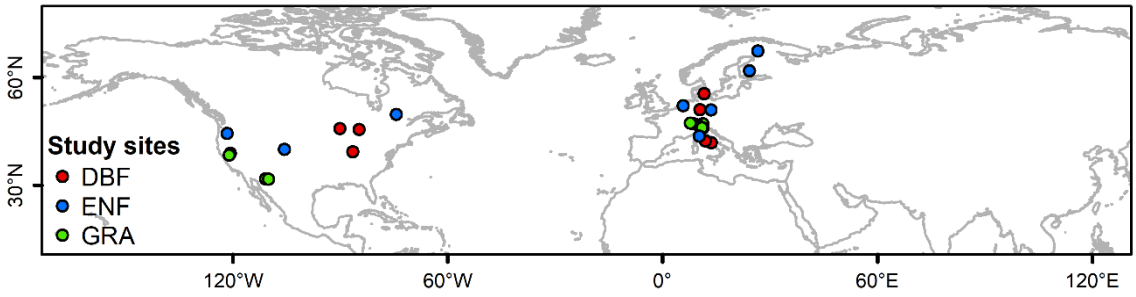

Figure 4.1 Study sites from FLUXNET2015 dataset including 11 evergreen needleleaf forest (ENF) sites, 7 deciduous broadleaf forest (DBF) sites, and 9 grassland (GRA) sites from the Northern Hemisphere.

4.2.2 Underlying water use efficiency

At the ecosystem level, ecosystem UWUE or apparent UWUE (UWUEa) (g C· $kPa^{0.5}$·kg H_2O^{-1}) is defined in equation (4.1) (Zhou et al. 2014).

$$UWUEa = \frac{GPP \times \sqrt{VPD}}{ET} \quad (4.1)$$

where GPP (g C·m^{-2}·$hour^{-1}$) is the gross primary production partitioned from net ecosystem exchange partitioning, VPD (kPa) is vapor pressure deficit, ET (kg H_2O·m^{-2}·$hour^{-1}$) is evapotranspiration derived from LE (W·m^{-2}) using the method in Tang et al. (2014).

Ecosystem potential UWUE (UWUEp) (g C·$kPa^{0.5}$·kg H_2O^{-1}) is defined in equation (4.2). As indicated by Zhou et al. (2016), ecosystem UWUEp corresponds to the UWUE at the leaf scale (UWUEi) under steady conditions (Equation 4.3).

$$UWUEp = \frac{GPP \times \sqrt{VPD}}{T} \quad (4.2)$$

$$UWUEp = UWUEi = \sqrt{\frac{CO2-\Gamma}{1.6\lambda}} \quad (4.3)$$

where T (kg $H_2O \cdot m^{-2} \cdot hour^{-1}$) is transpiration partitioned from ET based on a logarithmical relationship between LAI and T/ET ($T = ET \times aLAI^b$; a, and b are biome specific coefficients obtained from Wei et al. (2017) (Table S2.2)). In equation 4.3, CO2 (umol $CO_2 \cdot mol^{-1}$) represents the atmospheric CO_2 concentration, Γ is the leaf CO_2 compensation point, and λ represents the marginal water loss of carbon gain which is assumed as constant within a given vegetation type.

Thus, at the ecosystem level, UWUEa can be partitioned into UWUEp and T/ET (Equation 4.4).

$$UWUEa = UWUEp \times \frac{T}{ET} \quad (4.4)$$

4.2.3 Trend and attribution analyses

At the site level, we employed the Mann-Kendall test method to detect the upward or downward trends in annual UWUEa, UWUEp, T/ET, GPP, LE, VPD, CO2, SW, TA, SWC, and LAI, with a *p* value output indicating the significance of the trend. We used the Sen's slope estimator on the Mann-Kendall method to estimate the absolute slope of each variable over the period of records in each site. Sen's slope estimator reduces the influences from outliers by choosing the median of all linear slopes. In order to directly compare the trend in different variables, all annual estimates of each variable were transformed to relative changes (%, ratio of anomalies to mean values of each site) before trend analysis as previous studies did (Keenan et al. 2013; Wang et al. 2018). At biome level, the mean trend of each variable across all sites were calculated by the average of slopes over all sites, and the 95% confidence intervals for the mean trend were estimated

using the bootstrap method with 10,000 replications among those slopes following previous studies (Keenan et al. 2013; Wang et al. 2018).

In this study, the annual trend of UWUEa for each biome was partitioned to the trends in UWUEp and T/ET (Equation 4.4). We further attributed the variations in UWUEp and T/ET to variations in different environmental factors using the partial least square regression (PLSR), which has been widely used to establish relations between the response variables and independent variables, especially, when observations are few and large collinearity exists in independent variables (Martens and Næs 1989). However, PLSR can be severely affected by the presence of outliers (Serneels et al. 2005). We excluded those extreme outliers and leverage points which were identified through Minitab 18 statistical software (https://www.minitab.com/en-us/products/minitab/). Records with the absolute value of residual standard error > 2 or leverage > 3m/n (m is the number of components; n is the number of records) were considered as outliers or leverage points. The normalized regression coefficient from PLSR, and the *p* value on the basis of the Jackknife test indicate the contribution of each independent variable on the response variable.

4.3 Results

4.3.1 Annual trend in UWUEa, UWUEp, and T/ET

The ENF and DBF biome sites showed obvious positive mean trends in UWUEa, while GRA sites showed little mean trend in UWUEa (Figure 4.2a-c, Figure 4.3). In ENF, the mean trend (with the 95% confidence interval) across all sites was $0.6\%\cdot yr^{-1}$ (-0.4%~1.7%) (Figure 4.2a and Figure 4.3a). The mean trend (with the 95% confidence interval) in UWUEa across all DBF sites was $1.1\%\cdot yr^{-1}$ (-0.8%~1.7%) (Figure 4.2b and

Figure 4.3b). Two of the 11 ENF sites and three of the 7 DBF sites showed increases in UWUEa with $p<0.15$ over the period of record. There's no significant difference in trends in UWUEa between DBF and ENF sites ($p=0.68$, t test). The mean trend in UWUEa across all GRA sites was 0.0 $\%\cdot yr^{-1}$ with a relatively large 95% confidence interval (-1.2% ~1.9%) (Figure 4.2c and Figure 4.3c).

The magnitude of the mean trend in UWUEp was higher than the mean trend in T/ET in ENF and DBF (Figure 4.2 and Figure 4.3). For example, in DBF, the mean trend in UWUEp was 1.1%$\cdot yr^{-1}$ with a 95% confidence interval from -0.7%to 1.7%, which almost equals the mean trend in UWUEa (Figure 4.2b,e and Figure 4.3b). However, the mean trend in T/ET for DBF was 0.1%$\cdot yr^{-1}$. For GRA, neither UWUEp nor T/ET showed obvious trend over the study period (Figure 4.2f,i and Figure 4.3c).

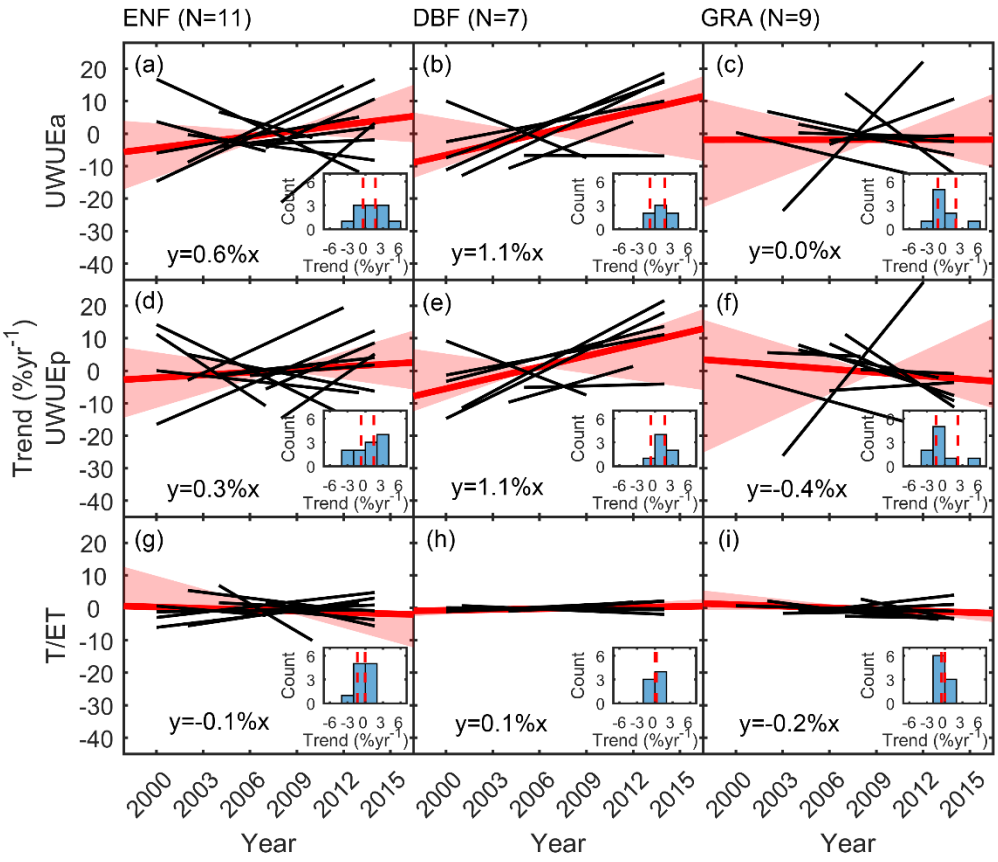

Figure 4.2 Trends in apparent underlying water use efficiency (UWUEa), potential underlying water use efficiency (UWUEp), and the ratio of transpiration to evapotranspiration (T/ET) for evergreen needleleaf forests (ENF; a, d, and g), deciduous broadleaf forests (DBF; b, e, and h), and grasslands (GRA; c, f, i). Short black lines are the annual trends for individual sites. Individual site names, and site years are given in the Table S4.1. Bold red lines are the mean trends across all sites in each biome. The red area shows trends within bootstrapped 95% confidence intervals for the mean trend. The inset shows the distribution of the site-level slopes in each biome. Dashed red lines represent bootstrapped 95% confidence intervals for the mean slope.

4.3.2 Attribution analyses for UWUEp and T/ET variation to environmental factors

The annual trends in UWUEa, UWUEp, T/ET, GPP, LE, and LAI, associated with the trends in environmental variables were shown in Figure 4.3. Generally, SW and TA showed little changes over the study period in each biome from the Northern Hemisphere. However, all sites showed a positive trend in the atmospheric CO_2 concentration with a

mean trend of 0.6%·yr^{-1} in forests and 1.0%·yr^{-1} in grasslands. In addition, ENF and DBF sites showed a great increase in VPD with a mean trend of 0.8%·yr^{-1} in ENF and 2.2%·yr^{-1} in DBF. For SWC, DBF showed a substantial decrease with a mean trend of -2.1%·yr^{-1}, while ENF showed no obvious change and GRA showed an increase (0.8%·yr^{-1}) in the study period. Moreover, only in DBF did LAI showed a slight increase (0.5%·yr^{-1}).

The responses of UWUEp and T/ET to each environmental factor are shown in Figure 4.4. For each biome, the UWUEp showed strong positive correlations with CO2 and VPD with normalized regression coefficient >0.15, and the T/ET was positively correlated with TA and SW (Figure 4.4), although TA and SW showed no trend over the study period (Figure 4.3). In addition, the UWUEp in DBF and GRA showed a negative response to SWC with a normalized regression coefficient at -0.20 (p<0.05) and -0.25 (p<0.01), respectively. The T/ET in DBF and GRA showed a significant negative correlation with CO2 (p<0.05).

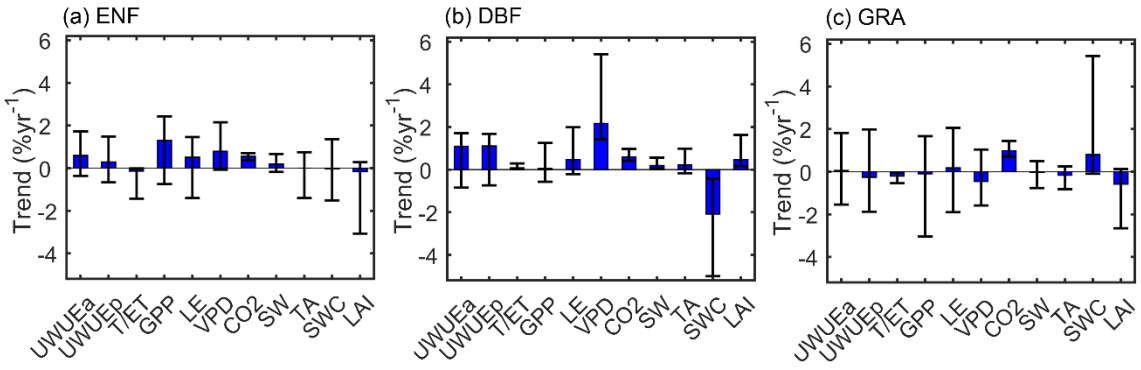

Figure 4.3 Mean trends in underlying water use efficiency (UWUEa, and UWUEp), ratio of transpiration to evapotranspiration (T/ET), gross primary production (GPP), latent heat (LE), vapor pressure deficit (VPD), atmospheric CO_2 concentration (CO2), incoming shortwave radiation (SW), air temperature (TA), soil water content (SWC), and Leaf area index (LAI)) in evergreen needleleaf forests (ENF; a), deciduous broadleaf forests (DBF; b), and grasslands (GRA; c). The error bars represent the bootstrapped 95% confidence intervals for the mean trend.

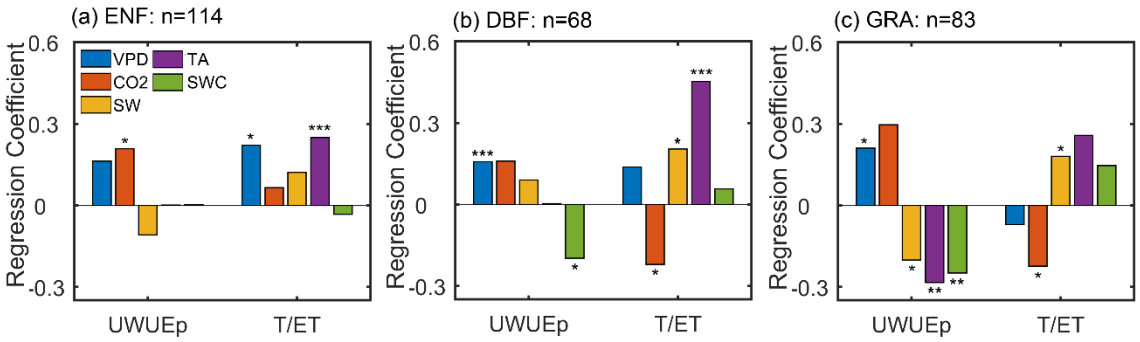

Figure 4.4 Normalized regression coefficients from the partial least squares regression between annual changes in potential underlying water use efficiency (UWUEp) or the ratio of transpiration to evapotranspiration (T/ET) and annual changes in environmental variables. Environmental variables include vapor pressure deficit (VPD), atmospheric CO_2 concentration (CO2), incoming shortwave radiation (SW), air temperature (TA), and soil water content (SWC). The star marks above the bars indicate the significance of the regression: * indicates $p<0.05$, ** indicates $p<0.01$, and * indicates $p<0.001$. n indicates the number of records used in the regression analysis for each biome.**

4.4 Discussion

Our study investigated the responses of UWUE to different environmental factors in forests and grasslands in the Northern Hemisphere. Based on the formulation of UWUE, the trends in UWUEa can be attributed to UWUEp, and T/ET trajectories (Zhou et al. 2017). We further analyzed the responses of UWUEp and T/ET to different environmental factors to evaluate the contribution of environmental changes on carbon-water coupling. Our results showed that ENF and DBF showed an obvious increase in UWUEa, while GRA showed no obvious changes in UWUEa. The increase in UWUEa in forests was mainly contributed by the increasing UWUEp which was triggered by increasing CO2 and VPD, as well as the decreasing SWC in DBF. For GRA, neither UWUEp nor T/ET showed obvious trends. The positive effect of increasing CO2 on UWUEp might be offset by the negative effect of increasing SWC on UWUEp in GRA.

The T/ET which was primarily controlled by SW and TA in all biomes showed little trend in our study. Our study highlights the combined effects of increasing atmospheric CO_2 and water stress (i.e. increasing VPD or decreasing SWC) on UWUE.

In our study, we found an general positive trend in UWUEa in forest sites, which is consistent with previous findings by Keenan et al. (2013) and Wang et al. (2018). The magnitude of the trends in UWUEp in both ENF and DBF are slightly smaller than the trends in intrinsic WUE (iWUE) in Wang et al. (2018). In comparison with UWUEp, iWUE includes the nonlinear VPD effect on c_i/c_a, which leads to a slight overestimate of WUE trends. Also, there were no significant differences in the trends of UWUEa between ENF and DBF sites, which differs from previous studies. The differences in length of study period for each site and the timescale of WUE used between previous studies and our study might influence the absolute magnitude of trends in WUE. However, the causes of the increasing UWUEa were also biome-dependent in our study, which supports previous results in Wang et al. (2018). In our study, among all biomes, the changes in UWUEa could be attributed to changes in UWUEp, since the T/ET was almost constant in the study period (Figure 4.2). The SW and TA showed strong correlations with T/ET but had little trend over time (Figure 4.3-4.4), resulting in a relative constant T/ET over time. In ENF, the increase in VPD and CO2 triggered the increase in UWUEp, which was also reflected by enhanced GPP (Figure 4.3a, and Figure 4.4a). In DBF, the secular increase in CO2 and large increase in VPD, associated with the decreased SWC jointly induced the increase in UWUEp (Figure 4.3b, Figure 4.4b). The positive CO2 fertilization effect on carbon uptake might be offset by negative effect of water stress on carbon uptake in DBF, resulting in no obvious change in GPP though there's a slight increase in LAI

(Figure 4.3b). Fewer studies have examined the responses of WUE to environment changes in GRA. The existence of large proportion of soil evaporation in grassland ET is a large challenge in WUE analyses. In our study, by partitioning T from ET using LAI, we found that there was no obvious change in either UWUEp or T/ET in GRA though the UWUEp was also positively correlated with the CO2 and VPD and negatively correlated with the SWC (Figure 4.3c, and Figure 4.4c). The increasing SWC might has reduced the positive effect of increasing CO2 on UWUEp in GRA. The GPP in GRA was expected to increase with the increase in CO2 and SWC; however, we did not observe an increase in GPP and there was even a decreasing trend in LAI from GRA (Figure 4.3c), which might be regulated by other environmental factors.

According to equation 4.3, ecosystem UWUEp corresponds to the UWUEi at the leaf scale under steady conditions, which has excluded all VPD effects and is only sensitive to the atmospheric CO_2 concentration and plant functional type (λ). In our results, UWUEp was not only positively correlated with CO2 but also positively correlated with VPD (Figure 4.4), which is consistent with results using iWUE from Wang et al. (2018). In addition, UWUEp also showed a negative correlation with SWC in DBF, and GRA in our study. Leaf-level WUE is expected to increase under elevated CO_2 concentration by enhancing the carbon uptake and reducing water loss through partial stomatal closures. The additional VPD or SWC effect on UWUEp might be reflected by changes in λ, which indicates some changes in vegetation composition or structure occur in the study period. A recent study showed that the water stress tends to induce a shift in tree species composition from less drought-tolerant species to species that are more tolerant to drought in eastern U.S. from 1980s to 2000s (Zhang et al. 2018a).

In our results, the increasing VPD in ENF and DBF associated with the decreasing SWC in DBF also represent increased water stress in forests in the Northern Hemisphere. It might be helpful to further explore what happened in forest structure or species composition across those sites.

Some limitations also exist in our study. First, we used a simplified algorithm based on Wei et al. (2017) to partition T from ET using LAI, in order to separate the UWUEp and T/ET components from UWUEa. There are uncertainties in this empirical relationships between T/ET and LAI. Second, nitrogen deposition and land use change have also been found to potentially influence the UWUEp and T/ET (Fleischer et al. 2013; Zhou et al. 2017). Fleischer et al. (2013) found that nitrogen deposition was nonlinearly related to photosynthetic capacity in ENF and exhibited little response to photosynthetic capacity in DBF using GPP data from EC flux sites and nitrogen deposition data from model output. In this study, all sites are from natural ecosystems, hence, we didn't consider land use changes. However, site-level N deposition measurements were not available in this study and its's influence on UWUE was not evaluated.

4.5 Conclusion

Ecosystem UWUE provides an optimal indicator for responses of ecosystem carbon-water coupling to environmental changes. By partitioning ecosystem UWUEa into UWUEp and T/ET, we further attributed the responses of UWUEp and T/ET to different environmental factors. Over past decade, both ENF and DBF showed an obvious increase in UWUEa, while GRA showed little changes in UWUEa. The changes in UWUEa were attributed to the changes in UWUEp, with little trend found in T/ET across all biomes. The increase in UWUEp in ENF was primarily triggered by increasing CO2 and VPD.

The increase in UWUEp in DBF was triggered by increasing CO2 and VPD, as well as decreasing SWC. For GRA, neither UWUEp nor T/ET exhibited a trend. The positive effect of CO_2 fertilization on UWUEa might be offset by the negative effect of increasing SWC in GRA. Our study applied a new way to evaluate the responses of ecosystem WUE to different environment factors using flux tower datasets.

Supplementary materials

Table S4.1 Flux tower sites and corresponding years used in this study.

ID	Site ID	Latitude	Longitude	IGBP type	Years used	Number of years
1	AT-Neu	47.1167	11.3175	GRA	2002-2012	11
2	CA-Qfo	49.6925	-74.342	ENF	2004-2010	7
3	CH-Cha	47.2102	8.4104	GRA	2006-2011, 2013-2014	8
4	CH-Dav	46.8153	9.8559	ENF	2007-2014	8
5	CH-Fru	47.1158	8.5378	GRA	2006-2014	9
6	CH-Oe1	47.2858	7.7319	GRA	2002-2008	7
7	DE-Gri	50.9495	13.5125	GRA	2007-2014	8
8	DE-Hai	51.0792	10.453	DBF	2000-2009	10
9	DE-Tha	50.9636	13.5669	ENF	2000-2014	15
10	DK-Sor	55.4859	11.6446	DBF	2000-2007, 2014	9
11	FI-Hyy	61.8475	24.295	ENF	2000-2013	14
12	FI-Sod	67.3619	26.6378	ENF	2008-2014	7
13	IT-Col	41.8494	13.5881	DBF	2005-2009, 2011-2014	9
14	IT-Lav	45.9562	11.2813	ENF	2004-2014	11
15	IT-MBo	46.0147	11.0458	GRA	2004-2013	10
16	IT-Ro2	42.3903	11.9209	DBF	2004-2008, 2010-2012	8
17	IT-SRo	43.7279	10.2844	ENF	2002-2012	11
18	NL-Loo	52.1666	5.7436	ENF	2000, 2002-2013	13
19	US-Blo	38.8953	-120.63	ENF	2000-2007	8
20	US-Me2	44.4523	-121.56	ENF	2002-2014	13
21	US-MMS	39.3232	-86.413	DBF	2000-2014	15

22	US-NR1	40.0329	-105.55	ENF	2006-2014	9
23	US-SRG	31.7894	-110.83	GRA	2008-2014	7
24	US-UMB	45.5598	-84.714	DBF	2001-2014	14
25	US-Var	38.4133	-120.95	GRA	2000-2014	15
26	US-WCr	45.8059	-90.08	DBF	2000-2006, 2011-2014	11
27	US-Wkg	31.7365	-109.94	GRA	2004-2014	11

Chapter 5: Global evapotranspiration over the past decade: estimation based on underlying water use efficiency combined with land primary production

Abstract

Evapotranspiration (ET) is a major water flux in the land water cycle and is tightly linked to ecosystem primary productivity. Given the strong coupling of ecosystem carbon and water fluxes, knowing one component provides information about the other. At present, ET estimation largely relies on hydroclimatic models, e.g. Penman-Monteith equation, which needs to quantify large sets of driving factors and hence have large uncertainties. However, ecosystem gross primary production (GPP) driven by light-use efficiency model showed better performances against flux tower measurements. In this study, we derived a global 8-day, 0.5° resolution ET product for 2003-2015 using GPP from the vegetation photosynthesis model (VPM), vapor pressure deficit (VPD) data derived from Atmospheric Infrared Sounder (AIRS), and ecosystem underlying water use efficiency (UWUE) derived from the FLUXNET2015 dataset. ET was calibrated and validated at the site level using eddy covariance measurements, and was also compared with MODIS ET product (MOD16A2.006). Our ET estimates explained ~48% of tower-measured ET, while MODIS ET explained ~42% of tower-measured ET. On a global scale, ET showed similar spatial pattern and interannual trend as GPP. There was a significant increase in ET in many regions in the Northern Hemisphere and a significant decrease in ET in amazon regions. This study highlighted the potential and simplicity of estimating ET through carbon-centric approaches based on UWUE.

5.1 Introduction

Evapotranspiration (ET) is one of the most important water fluxes in terrestrial ecosystems. More than 60% of precipitation is evaporated or transpired to the atmosphere from the land surface (Oki and Kanae 2006). The changes in ET indicates the water, energy, and carbon cycle dynamics in terrestrial ecosystems. Evapotranspiration also provides a good indicator of land cover and land use changes (Fisher et al. 2011). Thus, accurately estimating the spatiotemporal dynamics of global ET is critical for better predicting future global carbon, water, and energy budgets and understanding how they respond to climate change.

In an ecosystem, carbon and water cycles are tightly linked (Chapin et al. 2011; Law et al. 2002). Plants uptake carbon from the atmosphere while simultaneously losing water through stomatal (Medlyn et al. 2011). Ecosystem water use efficiency (WUE; GPP/ET), defined as the ratio of gross primary production (GPP) to ET, has been widely used to characterize the tradeoff between carbon gain and water loss at ecosystem scale (Niu et al. 2011). Thus, based on a given WUE, knowing either one of GPP and ET provides information about the other (Beer et al. 2010; Sun et al. 2011b; Zhang et al. 2016b). Mover, recent studies found that VPD has strong effects on carbon-water coupling (Beer et al. 2009; Medlyn et al. 2011; Zhou et al. 2014). By incorporating the linear effect of VPD on transpiration, the inherent WUE (IWUE; GPP×VPD/ET) proposed by Beer et al. (2009) was found to be more stable than WUE on a daily to annual timescales. By further incorporating the nonlinear effect of VPD on carbon assimilation, Zhou et al. (2014) proposed the underlying WUE (UWUE; $GPP \times VPD^{0.5}/ET$), which was

demonstrated as an optimal formulation of carbon-water coupling on sub-daily to daily timescale (Zhou et al. 2014, 2015).

Several studies have used ET to estimate GPP through WUE, a water-centric approach (Beer et al. 2010; Cheng et al. 2017; Sun et al. 2011b). Those studies depended on the assumption that ET could be better determined through hydrological observation or model simulations e.g. Penman-Monteith equation (Mu et al. 2011) and Priestley and Taylor equation (Martens et al. 2017), while GPP was harder to determine in the systems of interest. However, advances have been made in estimating global GPP based on measurements of optical parameters related to vegetation structure or function (e.g. vegetation indices, solar-induced chlorophyll fluorescence (SIF)) (Anav et al. 2015; Sun et al. 2018; Zhang et al. 2018b). There has been a good agreement between GPP derived from remote sensing and flux tower measured GPP (Ma et al. 2018; Zhang et al. 2017). Compared to GPP estimation, ET estimation is less reliable due to challenges in quantifying all parameters that govern energy exchange and corresponding latent heat flux from vegetated land surface (Sun et al. 2011a; Zhang et al. 2016a; Zhang et al. 2016b). Thus, carbon-centric models could be preferable to estimate ET from GPP and may provide better accuracy than water-centric approaches. Based on this, Zhang et al. (2016b) estimated the global monthly ET for the year of 2001 using GPP derived by a light-use efficiency model and UWUE derived from flux tower measurements and found that ET estimated by carbon-centric model matches tower-measured ET well. However, they only generated ET for one single year and the ET dynamics over time were unknown.

The aim of this study is to develop an 8-day, 0.5° resolution ET data product globally for 2003-2015 using the carbon-centric approach relying on UWUE. We utilized

GPP data from VPM and VPD data derived from Atmospheric Infrared Sounder (AIRS) as model input. ET was calibrated and validated against flux tower measured ET, as well as moderate Resolution Imaging Spectroradiometer (MODIS) ET. The interannual trends in ET, GPP, and VPD for 2003-2015 were characterized at the global scale finally.

5.2 Materials and methods

5.2.1 EC flux tower datasets

We used 1991-2014 daily EC flux data from the FLUXNET2015 dataset (http://fluxnet.fluxdata.org/data/fluxnet2015-dataset/), including gross primary production (GPP, hereafter GPP_{EC}), latent heat (LE), and vapor pressure deficit (VPD). Flux tower measured ET (hereafter ET_{EC}) was converted from LE (W/m^2) using the method in Tang et al. (2014). In this study, only daily records labeled with percentage of measured and good quality gap fill data >80% were used in this study. Some extreme records with daily WUE > 6.0 g C/kg H_2O were also removed following Zhang et al. (2016b). Finally, daily records were aggregated to 8-day timescale estimates for each year in each site to correspond the 8-day MODIS product. In total, we identified 161 sites distributed across 11 biomes globally totaling 28784 8-day records (Table 5.1). The major ecosystem types in these sites are evergreen needleleaf forests (ENF), evergreen broadleaf forests (EBF), deciduous broadleaf forest (DBF), mixed forests (MF), closed shrublands (CSH), open shrublands (OSH), woody savannas (WSA), savannas (SAV), grasslands (GRA), wetlands (WET), and croplands (CRO) based on the IGBP classification scheme.

Table 5.1 Data usage in this study.

Biome type	Num. of sites	Total records	Calibration records	Validation records
ENF	37	7868	3934	3934
EBF	12	2530	1265	1265
DBF	19	4042	2021	2021
MF	8	2010	1005	1005
CSH	2	430	215	215
OSH	9	545	273	272
WSA	6	1585	793	792
SAV	7	1118	559	559
GRA	29	4174	2087	2087
WET	16	1557	779	778
CRO	16	2925	1463	1462
ALL	161	28784	14394	14390

5.2.2 VPM GPP dataset

We used global GPP data from VPM simulations (hereafter GPP_{VPM}), which is a light-use efficiency model driven by MODIS vegetation indices, land cover maps, and NCEP Reanalysis II climate data (Xiao et al., 2004, Xiao et al., 2005). GPP_{VPM} is available for 2000-2017 with a 500m, 8-day resolution (Zhang et al., 2017). This GPP product showed a strong spatiotemporal consistency with in situ GPP estimates across biomes (Ma et al., 2018, Zhang et al., 2017). For this study, we used the 8-day, 500m GPP, and the 8-day, 0.5° GPP_{VPM} for 2003-2015.

5.2.3 Global VPD dataset

We used daily meteorological data from Atmospheric Infrared Sounder (AIRS) level 3 (https://airs.jpl.nasa.gov/data/products) to generate VPD at daily temporal resolution and 1° spatial resolution for 2003-2015. The AIRS instrument suite was launched aboard NASA's Aqua Earth Observing System satellite on May 4, 2002. The satellite equatorial crossing local times are 1:30 a.m. in a descending orbit, and 1:30 p.m. in an ascending orbit. We used the average of the VPD estimates from descending and ascending orbits

as the daily VPD. For this study, we aggregated the daily VPD to 8-day timescale and resampled the 1° resolution to 0.5° resolution to match GPP_{VPM} data.

5.2.4 MODIS datasets

We used MODIS GPP data (MOD17A2H.006) (hereafter GPP_{MOD17}) produced by NASA Land Processes Distributed Active Archive Center (https://lpdaac.usgs.gov). It provides 8-day, 500m GPP data from 2000 to present. This product was developed from a light use efficiency model using MODIS vegetation indices and meteorological information as inputs (Zhao and Running 2010).

We used MODIS ET data (MOD16A2.006) product (hereafter ET_{MOD16}) produced by NASA Land Processes Distributed Active Archive Center (https://lpdaac.usgs.gov). It provides 8-day, 500m ET data from 2000 to present. This product was based on the Penman-Monteith algorithm using daily GMAO climate data, MODIS land cover, albedo, LAI and EVI as input (Mu et al. 2011).

We used the IGBP land cover data from MODIS (MCD12C1.006), which is at yearly, 0.05° resolution. It produced the sub-pixel proportions of each land cover type. In our study, we aggregated the product to 0.5° resolution and re-identified the dominant land cover type in each pixel.

5.2.5 ET Calibration and validation

We randomly divided the 28784 records screened from 161 sites into two group, one for calibration (14390 records) and the other for validation (14394 records) (Table 5.1). The calibration dataset was used to estimate the UWUE (Equation 5.1) at the biome level. Then we generated the ET using 500m GPP_{VPM} for each site-8-day record based on the UWUE. To validate the performance of ET estimated through GPP_{VPM}, we compared the

ET estimated through GPP_{VPM} and the ET_{MODIS} against the ET_{EC} in both calibration and validation datasets.

According to the ratio representation of UWUE (Equation 5.1), UWUE was calculated as the slope of linear regression between $GPP \times VPD^{0.5}$ and ET by forcing the intercept to 0 following Zhang et al. (2016b) during calibration (Figure 5.1). Hence, the estimates of UWUE derived from the slope method could also be compared with ratio estimates in other studies. The root mean square error (RMSE) from the linear regression without intercept was used to describe the model performance. For the DNF, as we lack data in flux tower dataset, we used UWUE of MF as a substitute. Because DNF and MF were shown having similar parameters in a model analysis (Zhao and Running 2010).

$$\mathrm{UWUE} = \frac{GPP \times \sqrt{VPD}}{ET} \quad (5.1)$$

5.2.6 Estimating global ET

After we completed the validation of ET at site level. We used the global gridded GPP_{VPM}, VPD, and biome-level UWUE to estimate the global ET at 8-day, 0.5° resolution from 2003 to 2015. The MODIS IGBP land cover data were used to identify the distribution of different biomes.

5.2.7 Trend analysis

To characterize the interannual trend of annual GPP, VPD, and ET, we aggregated the 8-day GPP, VPD, and ET to annual estimates. We employed the Mann-Kendall test method to detect the upward or downward trends in annual GPP, VPD, and ET for each pixel. The Mann-Kendall test is a nonparametric way to detect a trend in a series of values regardless of whether the trend is linear. The *p* value on the basis of the Mann-Kendall test indicates the significance of the trend. We used the Sen's slope estimator on the

Mann-Kendall method to estimate the absolute slope of each variable in each pixel. Sen's slope estimator could effectively reduce the influences from outliers by using the median of all linear slopes. In order to directly compare the magnitude of trends in different variables, all annual estimates of each variable were transformed to relative changes (%, ratio of anomalies to mean values of each pixel) before trend analysis as previous studies suggested (Keenan et al. 2013; Wang et al. 2018). Thus, the trends (%/yr) estimated for different variables could be compared.

5.3 Results

5.3.1 Modelled sited-level ET

Biome-level UWUE estimated from the calibration flux dataset is shown in Figure 5.1. $GPP \cdot VPD^{0.5}$ showed the strongest linear relationship with ET in comparison with the relationship between GPP (or GPP·VPD) and ET (Table 5.2). Among all biomes, CSH, OSH, WSA, and SAV sites showed the strongest linear regression between $GPP \cdot VPD^{0.5}$ and ET with RMSE<11. While WET and CRO sites showed the weakest linear regression between $GPP \cdot VPD^{0.5}$ and ET with RMSE>18. In addition, all forests and CRO showed higher UWUE than other biomes, e.g. the UWUE in DBF was 2.74 $gC \cdot kPa^{0.5}/kg\ H_2O$; the UWUE in CRO was 2.26 $gC \cdot kPa^{0.5}/kg\ H_2O$.

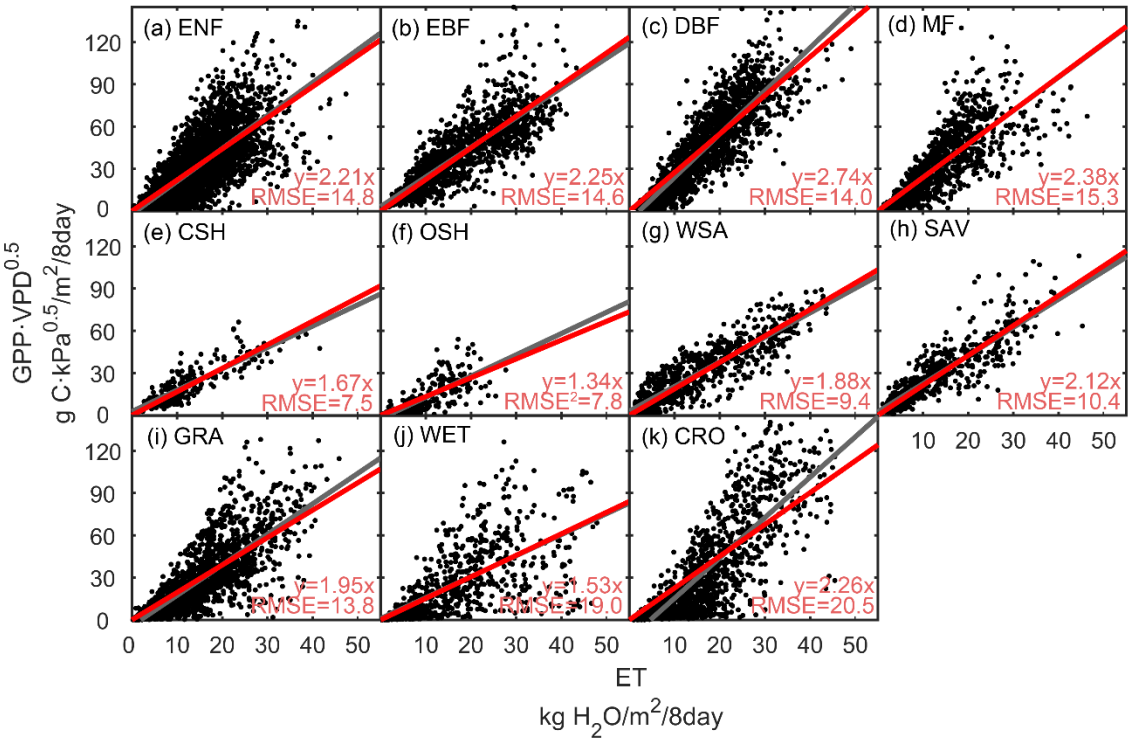

Figure 5.1 Biome-level UWUE estimated from the calibration dataset from FLUXNET2015. Each point represents the 8-day estimate of GPP×VPD0.5 and ET in each site year. Gray line is the linear regression with intercept. Red line is the linear regression by forcing the intercept to 0. Red texts showed the absolute value of the slope without intercept and corresponding RMSE.

Table 5.2 Biome-specific water use efficiency (WUE; g C/kg H_2O), inherent water-use efficiency (IWUE; g C·kPa/kg H_2O), and underlying water-use efficiency (UWUE; g C·kPa$^{0.5}$/kg H_2O) from calibration flux dataset. The slope and RMSE were estimated from the linear regression by forcing the intercept to 0.

Biome type	WUE (ET vs GPP)		IWUE (ET vs GPP×VPD)		UWUE (ET vs GPP×VPD$^{0.5}$)	
	Slope	RMSE	Slope	RMSE	Slope	RMSE
ENF	2.85	16.58	1.86	17.73	2.21	14.80
EBF	2.80	15.40	1.91	19.54	2.25	14.59
DBF	3.40	16.82	2.32	17.51	2.74	14.03
MF	3.11	17.47	1.92	17.64	2.38	15.28
CSH	2.06	9.80	1.40	7.70	1.67	7.47
OSH	1.51	9.32	1.27	8.33	1.34	7.79
WSA	1.79	9.10	2.05	14.64	1.88	9.36
SAV	1.85	9.60	2.53	15.88	2.12	10.36
GRA	2.57	19.59	1.63	14.49	1.95	13.78
WET	1.82	22.86	1.35	18.37	1.53	18.95
CRO	2.69	24.09	1.99	21.41	2.26	20.52
ALL	2.69	19.60	1.91	18.10	2.187	15.90

To validate the performance of ET, we compared the 8-day, 500m ET estimated in our study and ET_{MOD16} against flux tower measurements (Figure 5.2, Table S5.1). Overall, ET estimated in our study explained 48% of tower measured ET in validation dataset and 49% of tower measured ET in calibration dataset. As a reference data for ET validation, ET_{MOD16} could explained 42%, and 43% of tower-measured ET in validation and calibration dataset, respectively. In comparison with ET estimated in our study, ET_{MOD16} has an underestimation in ET_{EC} (Figure 5.2, Table S5.1).

Since ET estimation in this study largely relies on the accuracy of GPP input, we also compared the 8-day, 500m GPP_{VPM} and GPP_{MOD17} against GPP_{EC} (Figure 5.3, Table S5.2). Overall, GPP_{VPM} explained 60% and 61% of GPP_{EC} in validation and calibration dataset, respectively. GPP_{MOD17} explained 54% of GPP_{EC} in both validation and calibration datasets. In comparison with GPP_{VPM}, GPP_{MOD17} also has an underestimation in GPP_{EC} (Figure 5.3, Table S5.2).

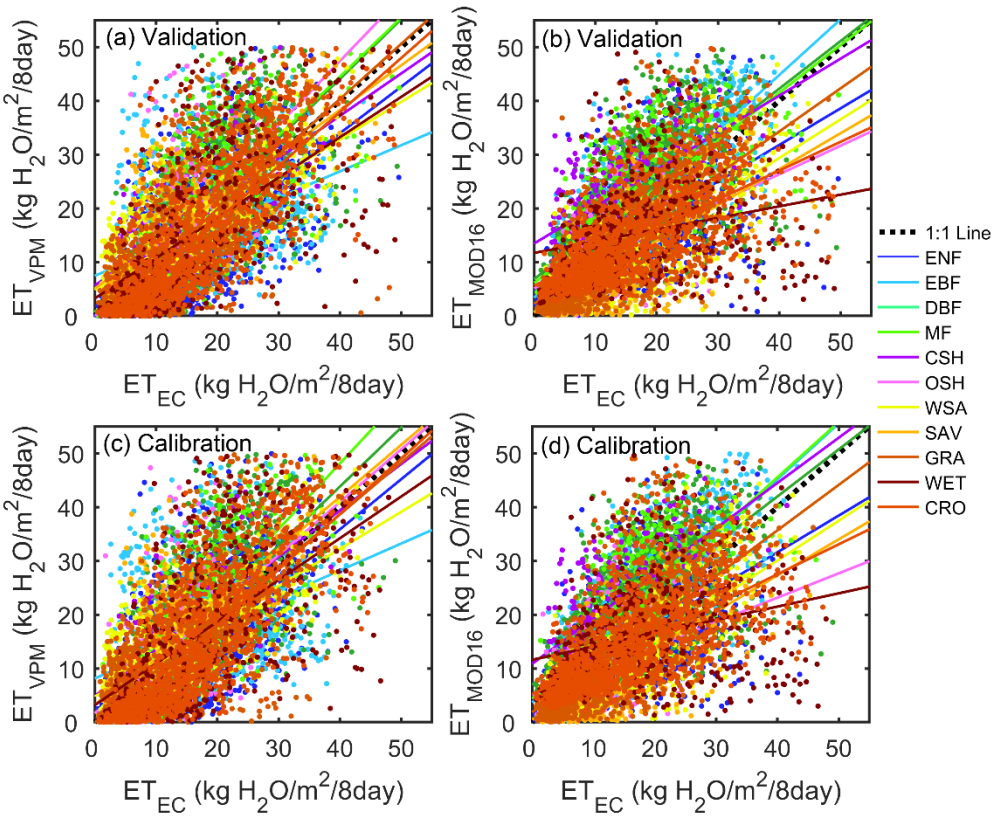

Figure 5.2 Comparison of ET estimated at 8-day, 500m resolution against flux tower measured ET. a and b are results for the validation dataset, and c and d are results for calibration dataset.

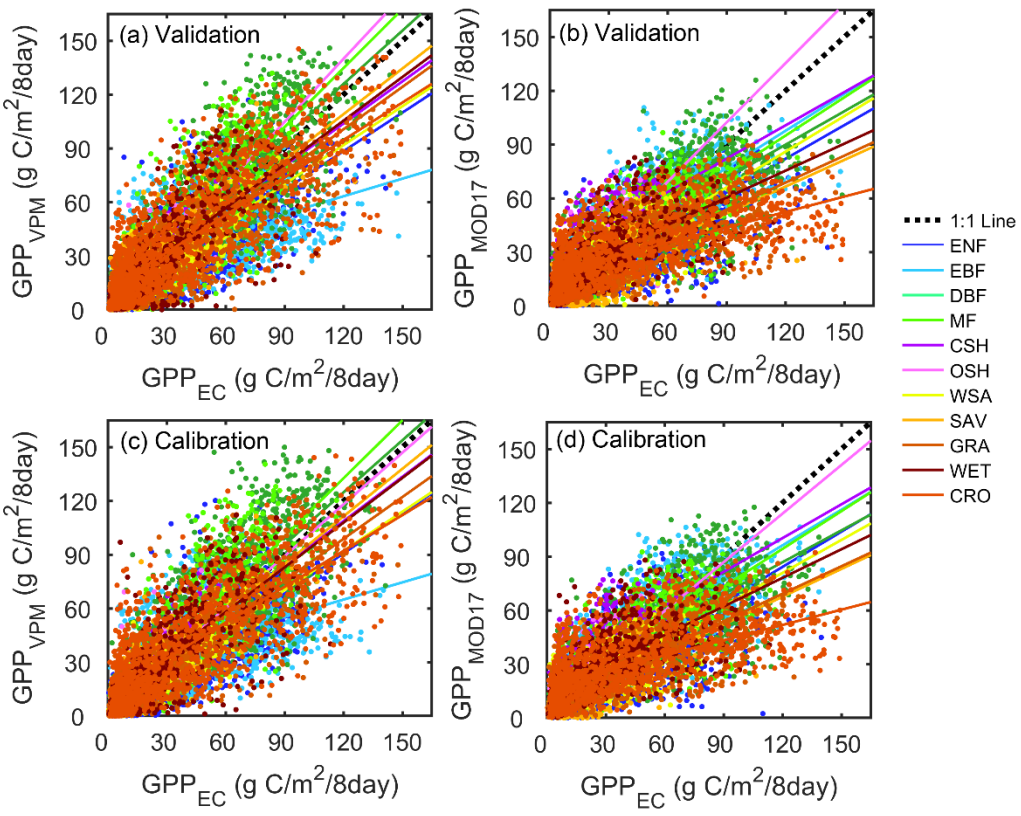

Figure 5.3 Comparison of VPM GPP at 8-day, 500m resolution against flux tower measured GPP. a and b are results for the validation dataset, and c and d are results for calibration dataset.

5.3.2 Modeled global ET

The total global ET over vegetated land was 545±8 mm/yr in this study. The spatial variation of annual mean ET was very similar to the distribution of GPP (Figure 5.4). Annual ET estimated in this study showed high values in tropical zones, especially in the Amazon regions, and low values in arid and semiarid regions, e.g. central Australia, and high latitude regions, which matches the annual GPP patterns. In summer, e.g. during 2015/7/12-2015/07/19, high ET values and GPP values both occurred in those crop zones and boreal forests in the Northern Hemisphere (Figure 5.5). The Highest annual mean

VPD was located in Sahara desert, and central Australia. Lowest mean annual VPD were found in high latitude areas and Tibetan plateau (Figure 5.4b).

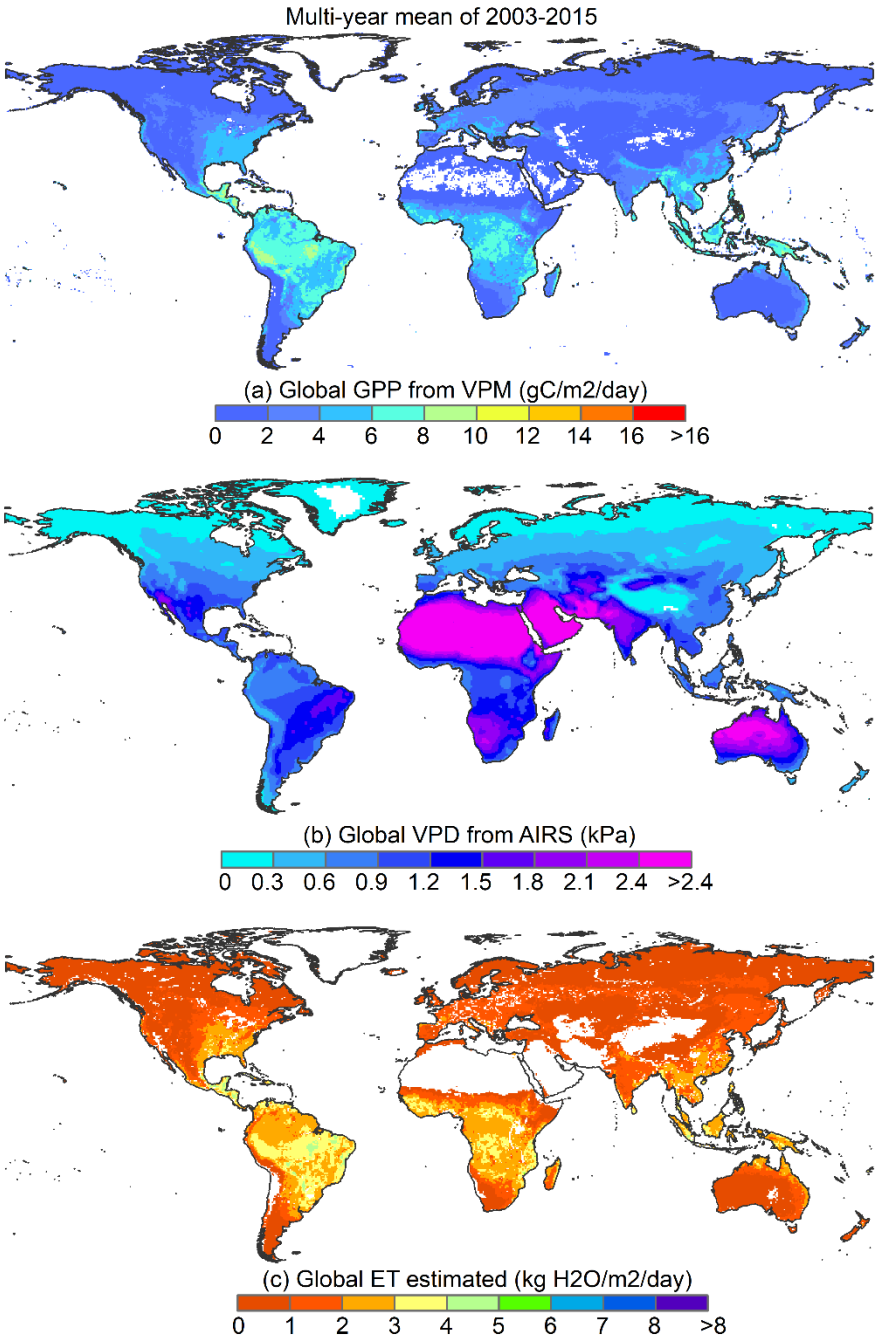

Figure 5.4 Global distribution of mean annual GPP, VPD, and ET during 2003-2015.

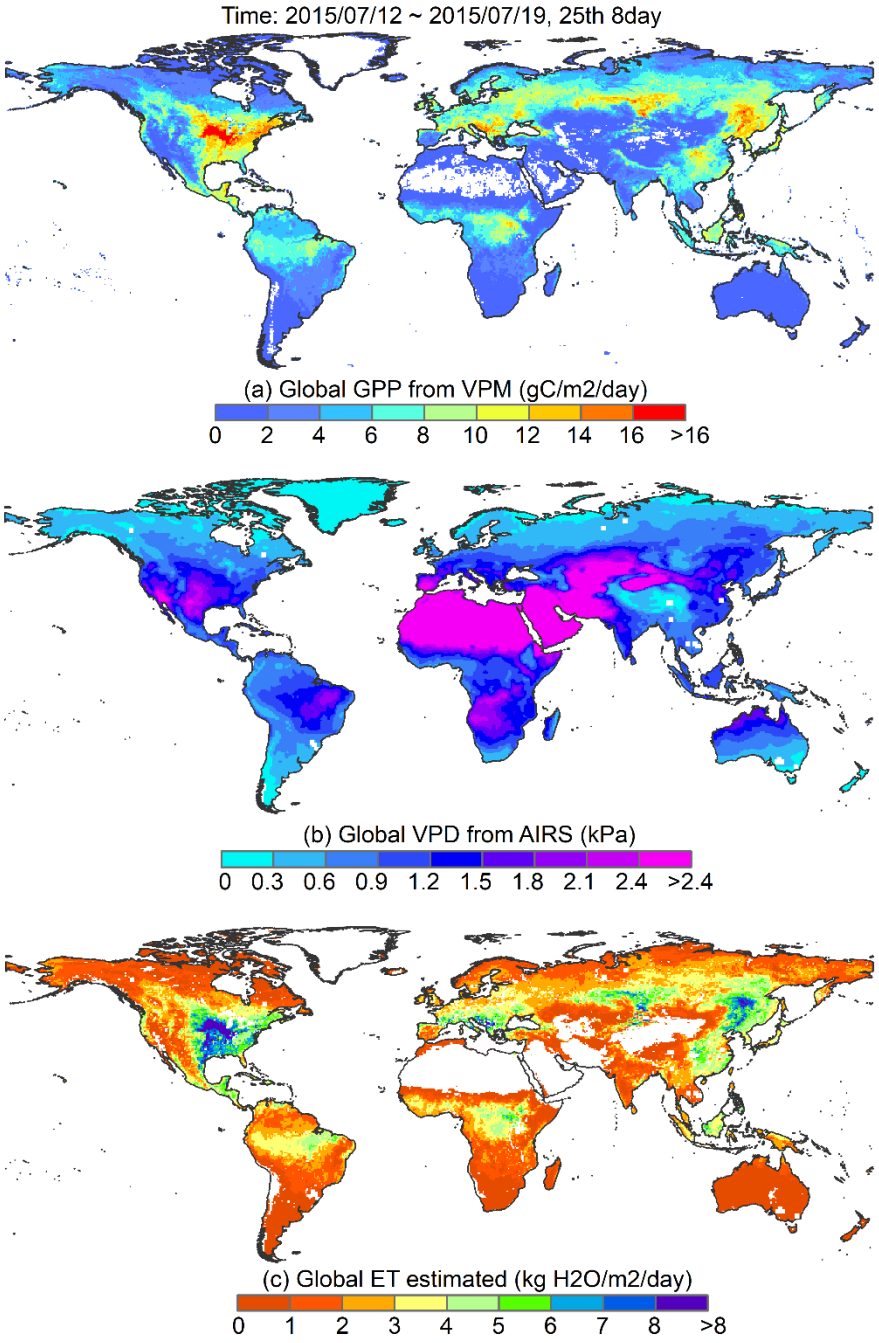

Figure 5.5 Global distribution of GPP, VPD and ET on 25th 8-day in 2015 at 0.5° resolution. Each pixel represents the 8-day mean in 2015/7/12-2015/07/19.

5.3.3 Trend in global ET

Overall, the annual ET estimated over the global vegetated area showed an increasing trend at 1.47 mm/yr or 1.47 kg $H_2O/m^2/yr$) over the study period (Figure 5.6). The interannual trends in GPP, VPD, and ET for each pixel were shown in Figure 5.6 by absolute values and in Figure 5.7 by relative changes. Generally, the spatial variation in trend of ET was also consistent with that of GPP. Most regions in the Northern Hemisphere showed an increasing trend in GPP and ET, e.g., central Europe, northern North America, and eastern Asia (Figure 5.7-5.8). The tropical regions in central Africa also showed increasing GPP and ET. However, Amazon regions showed a significant decreasing trend in both GPP and ET. For the VPD, it also showed increasing trend in central Europe and eastern Asia except India. Generally, it showed a decreasing trend in deserts in Africa and Australia, and India.

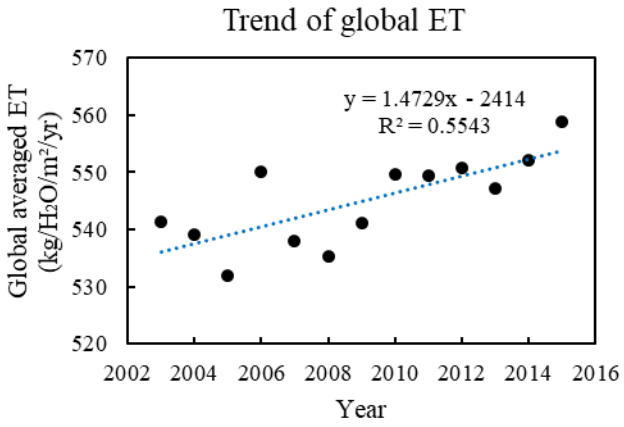

Figure 5.6 Interannual trend of global averaged ET estimated during 2003-2015 in this study.

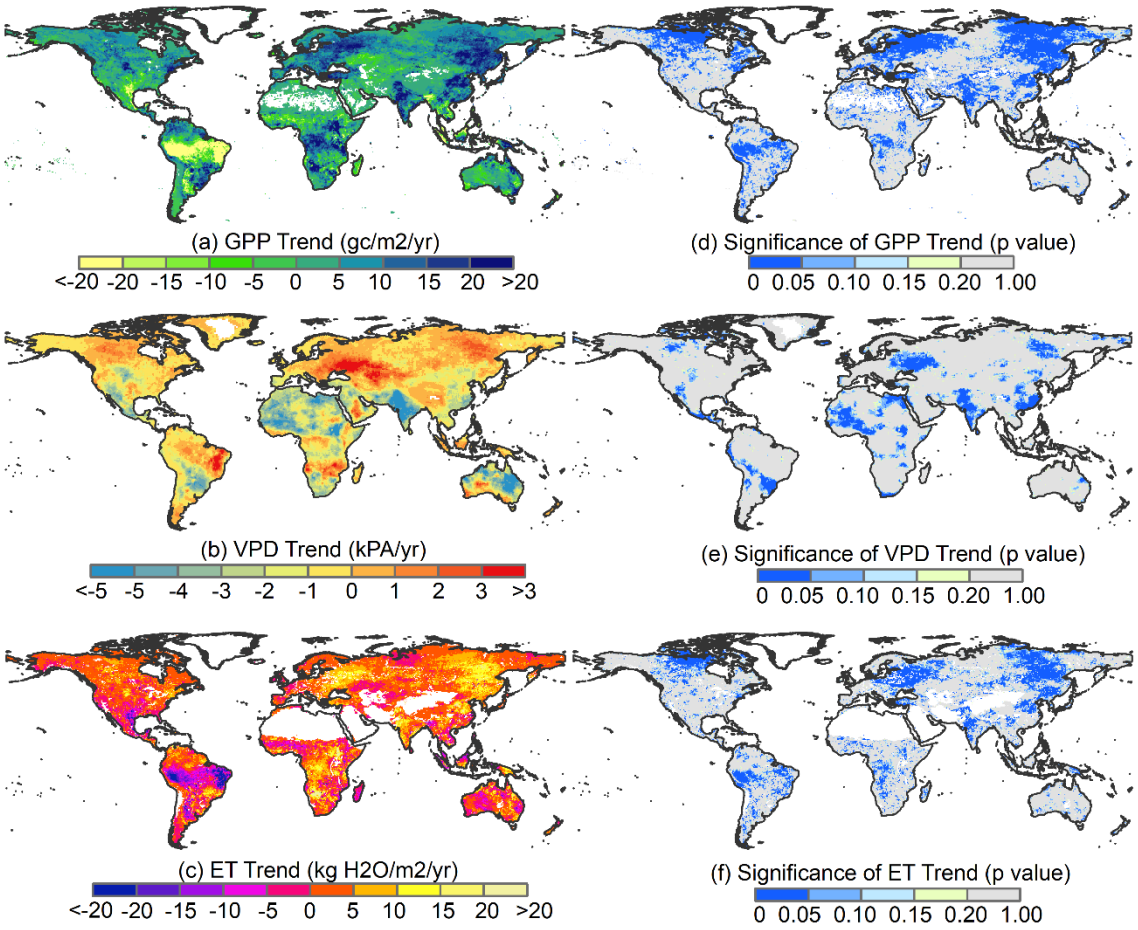

Figure 5.7 Interannual trend in absolute GPP, VPD and ET for 2003-2015 at global scale. Left panels showed the trend of each variable derived from Sen's Slope. Right panels showed the significance of the trend on the basis of Mann-kendall test.

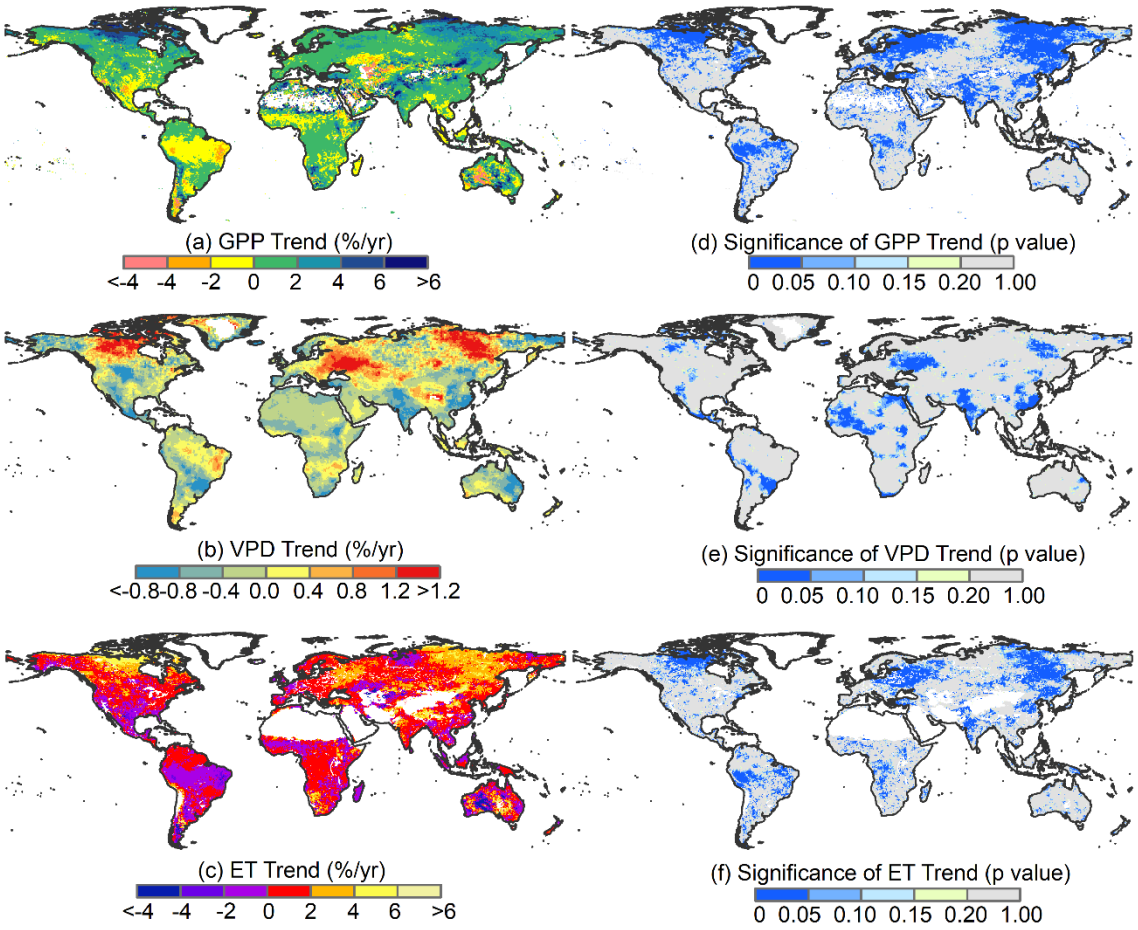

Figure 5.8 Interannual trend (%) in GPP, VPD and ET anomalies for 2003-2015 at global scale. Left panels showed the trend of each variable derived from Sen's Slope. Right panels showed the significance of the trend on the basis of Mann-kendall test.

5.4 Discussion

5.4.1 Model performances

Our results showed that ET estimated through this carbon-centric approach performed better relative to tower-measured ET than ET_{MOD16}. This improvement was largely due to the improved GPP estimates from VPM compared to GPP_{MOD17}. The spatial variation in ET and its interannual trend match the spatial patterns of GPP_{VPM}. This study highlighted the potential and simplicity of estimating ET through ecosystem carbon-water

coupling (i.e. UWUE) when the remote sensing data and biome specific parameters are available.

The total global ET over vegetated land was 545±8 mm/yr in this study, which is similar to ET from MODIS (554±374 mm/yr) (Mu et al. 2011) and is lower than ET estimated from water balance equation (558-650 mm/yr) (Zeng et al. 2012). Global ET was found to increase at a rate of 1.47 mm/yr from 2003 to 2015 (Figure 5.6), which is slightly faster than the increase rate reported for 1982-2009 (1.1 mm/yr) (Zeng et al. 2012). The biome-level UWUE derived from 8-day records is consistent with that derived from monthly records using FLUXNET datasets during 2000-2007 (Zhang et al. 2016b), with high UWUE values in forests and croplands and low UWUE values in shrublands (Figure 5.1 and Table 5.2). In comparison with flux tower ET, ET estimated in this study explained ~48% of tower ET, which is lower than the ET performance from Zhang et al. (2016b) (R^2>0.60). However, the number of 8-day records we employed was nearly seven times bigger than those monthly records they used for the same biomes.

5.4.2 Model advantages and limitations

Currently, ET from flux tower sites have large uncertainties due to the lack of closure of the energy budget using the eddy covariance technique. In this study, we used the reported LE measurements without energy balance adjustment to estimate ET_{EC}. In addition, this carbon-centric model relies on the accuracy of GPP data. In our study, GPP_{VPM} showed better consistence with flux tower observations (R^2≈0.60), in comparison with GPP_{MOD17} (R^2=0.54) (Figure 5.3). The improvement in GPP_{VPM} was largely contributed by CRO in which the composition of C3/C4 species were considered. However, the GPP_{VPM} in EBF showed a large underestimation against the flux tower estimates with R^2=0.18 in

validation dataset, which further induced the underestimation in ET in EBF in this study (Figure 5.2, Table S5.1-S5.2). Because of the cloudy weather in tropical areas, optical remote sensing images and climate input usually have low quality, which may impact the quality of GPP derived from light use efficiency model (Anav et al. 2015). In addition, UWUE incorporated the VPD effect on both carbon uptake and transpiration. However, the VPD effect on GPP might not be captured by VPM due to the different water scaler (i.e. LSWI) used in VPM.

In this study, UWUE best described the relationship between GPP and ET by incorporating the VPD effect on carbon uptake and transpiration, which supported previous study by Zhang et al. (2016b) (Table 5.2). However, at the ecosystem scale, GPP is actually coupled with transpiration, not evaporation (E) produced from soil or canopy surface. In our study, we used the GPP to derive ET directly at ecosystem scale, which introduces inevitable uncertainties. However, we accounted for E during the calibration process and we can provide better ET estimates at site level than ET_{MOD16} which is derived from more complicated model. Zhou et al. (2015) also showed a much stronger relationship between $GPP \cdot VPD^{0.5}$ and ET at daily timescale (R^2=0.70). Thus this carbon-centric approach based on UWUE is still an effective way to estimate ET at ecosystem scale.

5.5 Conclusion

We developed an 8-day, 0.5° global ET datasets based on GPP from VPM and UWUE derived at biome level. Our ET results was calibrated and validated at site level against flux tower measurements and was also compared with MODIS ET products. Overall, the 8-day ET estimated in our study explained ~48% of tower-measured ET, which performs

better than MODIS ET (~42%). The spatial variation in ET matches well with the GPP. The global ET estimated in our study is 545±8 mm/yr and showed an increasing trend (1.47 mm/yr) over the study period. There was a significant increase in ET in the Northern Hemisphere, e.g. central Europe, eastern Asia and a significant decrease in ET in the amazon forests.

Supplementary materials

Table S5.1 Comparison of ET estimated in our study (i.e. ET_{VPM}) and ET from MODIS (i.e. ET_{MOD16}) with ET from eddy flux tower (i.e. ET_{EC}) for different biomes based on validation and calibration datasets.

Biome types	Validation dataset				Calibration dataset			
	ET_{EC} vs ET_{VPM}		ET_{EC} vs ET_{MOD16}		ET_{EC} vs ET_{VPM}		ET_{EC} vs ET_{MOD16}	
	Slope	R^2	Slope	R^2	Slope	R^2	Slope	R^2
ENF	0.87	0.48	0.68	0.38	0.93	0.51	0.68	0.38
EBF	0.49	0.18	1.04	0.71	0.50	0.18	1.04	0.69
DBF	1.11	0.62	0.89	0.50	1.10	0.62	0.88	0.51
MF	1.10	0.56	0.88	0.49	1.22	0.60	1.03	0.55
CSH	0.79	0.46	0.69	0.39	0.86	0.48	0.84	0.46
OSH	1.19	0.33	0.53	0.16	0.98	0.27	0.45	0.13
WSA	0.70	0.55	0.72	0.65	0.69	0.57	0.74	0.65
SAV	0.83	0.48	0.67	0.54	0.97	0.56	0.67	0.54
GRA	1.02	0.58	0.80	0.51	0.97	0.53	0.85	0.51
WET	0.75	0.36	0.22	0.06	0.78	0.37	0.25	0.08
CRO	1.00	0.64	0.54	0.42	1.03	0.65	0.56	0.42
ALL	0.89	0.48	0.73	0.42	0.91	0.49	0.75	0.43

Table S5.2 Comparison of GPP from VPM (i.e. GPP_{VPM}) and GPP from MODIS (i.e. GPP_{MOD17}) with GPP from eddy flux tower (i.e. GPP_{EC}) for different biomes based on validation and calibration datasets.

Biome types	Validation dataset				Calibration dataset			
	GPP_{EC} vs GPP_{VPM}		GPP_{EC} vs GPP_{MOD17}		GPP_{EC} vs GPP_{VPM}		GPP_{EC} vs GPP_{MOD17}	
	Slope	R^2	Slope	R^2	Slope	R^2	Slope	R^2
ENF	0.72	0.60	0.63	0.54	0.74	0.63	0.65	0.57
EBF	0.33	0.18	0.69	0.60	0.32	0.16	0.66	0.57
DBF	0.99	0.76	0.62	0.62	0.97	0.74	0.59	0.60
MF	1.10	0.66	0.71	0.62	1.08	0.68	0.70	0.62
CSH	0.78	0.55	0.62	0.33	0.82	0.56	0.63	0.30
OSH	1.17	0.70	1.10	0.58	0.96	0.59	0.90	0.55
WSA	0.72	0.69	0.66	0.60	0.73	0.73	0.61	0.57
SAV	0.85	0.59	0.50	0.41	0.88	0.61	0.52	0.43
GRA	0.79	0.68	0.50	0.61	0.78	0.69	0.51	0.62
WET	0.81	0.51	0.50	0.39	0.83	0.54	0.53	0.43
CRO	0.70	0.66	0.29	0.43	0.67	0.64	0.28	0.41
ALL	0.78	0.60	0.57	0.54	0.78	0.61	0.57	0.54

Chapter 6: Conclusions and perspectives

Ecosystem carbon and water cycles are tightly interconnected. The interaction of carbon and water exchanges is an important ecosystem function that could substantially influence the global carbon, water, and energy budgets. Thus, quantifying the carbon-water coupling of terrestrial ecosystems and understanding how climate change and climate variability affect the coupled processes are critical for predicting future ecosystem responses and evaluated the global carbon and water budgets.

As the atmospheric carbon fixed by vegetation through photosynthesis, terrestrial gross primary production (GPP) is a primary driver of global carbon cycle. It is driven by temperature and precipitation in most terrestrial ecosystems, but ecosystem carbon cycles are fully coupled with ecosystem water fluxes (evapotranspiration and transpiration). My dissertation 1) quantified the overall relationship of GPP to precipitation and water fluxes at the site and the global scales in Chapter 2; 2) explored the coupling of GPP and precipitation (i.e. rain-use efficiency) in responses to precipitation variability and extreme drought in Chapter 3; 3) explored the coupling of GPP and evapotranspiration (i.e. water use efficiency) in response to CO_2 fertilization and other climate factors in Chapter 4; and 4) developed global ET maps based on the strong coupling of GPP and ET in Chapter 5.

Major findings in my dissertation include: 1) ecosystem GPP was more strongly coupled with evapotranspiration or transpiration than precipitation. This strong coupling relationship was further improved by incorporating the effect of vapor pressure deficit (VPD) on carbon uptake and transpiration; 2) extreme drought impacts on terrestrial ecosystems were identified by using the relationship between rain use efficiency and precipitation. Ecosystem rain use efficiency increased during moderate drought but will

likely decline with further water shortage, leading to ecosystem function loss; 3) underlying water use efficiency incorporated VPD effects on carbon-water coupling and is better metric than other C:H_2O efficiency terms to explain the responses of ecosystem to increasing CO_2. Underlying water use efficiency showed increasing trend in forests and no obvious trend in grasslands in the Northern Hemisphere. The variation in underlying water use efficiency was strongly regulated by CO_2 fertilization, VPD, and soil moisture; 4) ecosystem underlying use efficiency can be utilized to provide a better estimate of evapotranspiration in comparison traditional approaches. Global ET showed increasing trend in past decades.

Future, efforts should address the following scientific questions: 1) what's the range of water use efficiency between biome types or plant species; 2) how does plant or ecosystem carbon-water coupling respond to extreme climate conditions; 3) given that plant or ecosystem water use efficiency has been consistently reported to increase with elevated atmospheric CO_2 concentration or during drought, what is the magnitude of CO_2 fertilization and drought impacts on water use efficiency; 4) tropical regions still have large uncertainties in GPP and water flux estimation through remote sensing methods. Advances in remote sensing technique are needed to solve this issue.

References

Ahlstrom, A., Canadell, J.G., Schurgers, G., Wu, M., Berry, J.A., Guan, K., & Jackson, R.B. (2017). Hydrologic resilience and Amazon productivity. *Nat Commun, 8*, 387

Allen, C.D., Macalady, A.K., Chenchouni, H., Bachelet, D., McDowell, N., Vennetier, M., Kitzberger, T., Rigling, A., Breshears, D.D., Hogg, E.H., Gonzalez, P., Fensham, R., Zhang, Z., Castro, J., Demidova, N., Lim, J.-H., Allard, G., Running, S.W., Semerci, A., & Cobb, N. (2010). A global overview of drought and heat-induced tree mortality reveals emerging climate change risks for forests. *Forest Ecology and Management, 259*, 660-684

Anav, A., Friedlingstein, P., Beer, C., Ciais, P., Harper, A., Jones, C., Murray-Tortarolo, G., Papale, D., Parazoo, N.C., Peylin, P., Piao, S., Sitch, S., Viovy, N., Wiltshire, A., & Zhao, M. (2015). Spatiotemporal patterns of terrestrial gross primary production: A review. *Reviews of Geophysics, 53*, 785-818

Bai, Y.F., Wu, J.G., Xing, Q., Pan, Q.M., Huang, J.H., Yang, D.L., & Han, X.G. (2008). Primary production and rain use efficiency across a precipitation gradient on the Mongolia plateau. *Ecology, 89*, 2140-2153

Baldocchi, D., Falge, E., Gu, L.H., Olson, R., Hollinger, D., Running, S., Anthoni, P., Bernhofer, C., Davis, K., Evans, R., Fuentes, J., Goldstein, A., Katul, G., Law, B., Lee, X.H., Malhi, Y., Meyers, T., Munger, W., Oechel, W., U, K.T.P., Pilegaard, K., Schmid, H.P., Valentini, R., Verma, S., Vesala, T., Wilson, K., & Wofsy, S. (2001). FLUXNET: A new tool to study the temporal and spatial variability of ecosystem-scale carbon dioxide, water vapor, and energy flux densities. *Bulletin of the American Meteorological Society, 82*, 2415-2434

Barriopedro, D., Fischer, E.M., Luterbacher, J., Trigo, R., & Garcia-Herrera, R. (2011). The Hot Summer of 2010: Redrawing the Temperature Record Map of Europe. *Science, 332*, 220-224

Beer, C., Ciais, P., Reichstein, M., Baldocchi, D., Law, B.E., Papale, D., Soussana, J.F., Ammann, C., Buchmann, N., Frank, D., Gianelle, D., Janssens, I.A., Knohl, A., Köstner, B., Moors, E., Roupsard, O., Verbeeck, H., Vesala, T., Williams, C.A., & Wohlfahrt, G. (2009). Temporal and among-site variability of inherent water use efficiency at the ecosystem level. *Global Biogeochemical Cycles, 23*, 1-13

Beer, C., Reichstein, M., Tomelleri, E., Ciais, P., Jung, M., Carvalhais, N., Rodenbeck, C., Arain, M.A., Baldocchi, D., Bonan, G.B., Bondeau, A., Cescatti, A., Lasslop, G.,

Lindroth, A., Lomas, M., Luyssaert, S., Margolis, H., Oleson, K.W., Roupsard, O., Veenendaal, E., Viovy, N., Williams, C., Woodward, F.I., & Papale, D. (2010). Terrestrial gross carbon dioxide uptake: global distribution and covariation with climate. *Science, 329*, 834-838

Biederman, J.A., Scott, R.L., Goulden, M.L., Vargas, R., Litvak, M.E., Kolb, T.E., Yepez, E.A., Oechel, W.C., Blanken, P.D., Bell, T.W., Garatuza-Payan, J., Maurer, G.E., Dore, S., & Burns, S.P. (2016). Terrestrial carbon balance in a drier world: the effects of water availability in southwestern North America. *Glob Chang Biol, 22*, 1867-1879

Breshears, D.D., Cobb, N.S., Rich, P.M., Price, K.P., Allen, C.D., Balice, R.G., Romme, W.H., Kastens, J.H., Floyd, M.L., Belnap, J., Anderson, J.J., Myers, O.B., & Meyer, C.W. (2005). Regional vegetation die-off in response to global-change-type drought. *Proc Natl Acad Sci U S A, 102*, 15144-15148

Brett, M.T. (2004). When is a correlation between non-independent variables "spurious"? *Oikos, 105*, 647-656

Chapin, F.S., Matson, P.A., & Vitousek, P.M. (2011). *Principles of terrestrial ecosystem ecology*. (2nd ed. ed.). New York: Springer

Cheng, L., Zhang, L., Wang, Y.P., Canadell, J.G., Chiew, F.H.S., Beringer, J., Li, L., Miralles, D.G., Piao, S., & Zhang, Y. (2017). Recent increases in terrestrial carbon uptake at little cost to the water cycle. *Nat Commun, 8*, 110

Choat, B., Jansen, S., Brodribb, T.J., Cochard, H., Delzon, S., Bhaskar, R., Bucci, S.J., Feild, T.S., Gleason, S.M., Hacke, U.G., Jacobsen, A.L., Lens, F., Maherali, H., Martinez-Vilalta, J., Mayr, S., Mencuccini, M., Mitchell, P.J., Nardini, A., Pittermann, J., Pratt, R.B., Sperry, J.S., Westoby, M., Wright, I.J., & Zanne, A.E. (2012). Global convergence in the vulnerability of forests to drought. *Nature, 491*, 752-755

Ciais, P., Reichstein, M., Viovy, N., Granier, A., Ogee, J., Allard, V., Aubinet, M., Buchmann, N., Bernhofer, C., Carrara, A., Chevallier, F., De Noblet, N., Friend, A.D., Friedlingstein, P., Grunwald, T., Heinesch, B., Keronen, P., Knohl, A., Krinner, G., Loustau, D., Manca, G., Matteucci, G., Miglietta, F., Ourcival, J.M., Papale, D., Pilegaard, K., Rambal, S., Seufert, G., Soussana, J.F., Sanz, M.J., Schulze, E.D., Vesala, T., & Valentini, R. (2005). Europe-wide reduction in primary productivity caused by the heat and drought in 2003. *Nature, 437*, 529-533

de Jong, R., Schaepman, M.E., Furrer, R., de Bruin, S., & Verburg, P.H. (2013). Spatial relationship between climatologies and changes in global vegetation activity. *Global Change Biology, 19*, 1953-1964

Donat, M.G., Alexander, L.V., Yang, H., Durre, I., Vose, R., & Caesar, J. (2013). Global Land-Based Datasets for Monitoring Climatic Extremes. *Bulletin of the American Meteorological Society, 94*, 997-1006

Doughty, C.E., Metcalfe, D.B., Girardin, C.A., Amezquita, F.F., Cabrera, D.G., Huasco, W.H., Silva-Espejo, J.E., Araujo-Murakami, A., da Costa, M.C., Rocha, W., Feldpausch, T.R., Mendoza, A.L., da Costa, A.C., Meir, P., Phillips, O.L., & Malhi, Y. (2015). Drought impact on forest carbon dynamics and fluxes in Amazonia. *Nature, 519*, 78-82

Du, L., Mikle, N., Zou, Z., Huang, Y., Shi, Z., Jiang, L., McCarthy, H.R., Liang, J., & Luo, Y. (2018). Global patterns of extreme drought-induced loss in land primary production: Identifying ecological extremes from rain-use efficiency. *Sci Total Environ, 628-629*, 611-620

Estiarte, M., Vicca, S., Penuelas, J., Bahn, M., Beier, C., Emmett, B.A., Fay, P.A., Hanson, P.J., Hasibeder, R., Kigel, J., Kroel-Dulay, G., Larsen, K.S., Lellei-Kovacs, E., Limousin, J.M., Ogaya, R., Ourcival, J.M., Reinsch, S., Sala, O.E., Schmidt, I.K., Sternberg, M., Tielborger, K., Tietema, A., & Janssens, I.A. (2016). Few multiyear precipitation-reduction experiments find a shift in the productivity-precipitation relationship. *Glob Chang Biol, 22*, 2570-2581

Fisher, J.B., Whittaker, R.J., & Malhi, Y. (2011). ET come home: potential evapotranspiration in geographical ecology. *Global Ecology and Biogeography, 20*, 1-18

Fleischer, K., Rebel, K.T., van der Molen, M.K., Erisman, J.W., Wassen, M.J., van Loon, E.E., Montagnani, L., Gough, C.M., Herbst, M., Janssens, I.A., Gianelle, D., & Dolman, A.J. (2013). The contribution of nitrogen deposition to the photosynthetic capacity of forests. *Global Biogeochemical Cycles, 27*, 187-199

Frank, D., Reichstein, M., Bahn, M., Thonicke, K., Frank, D., Mahecha, M.D., Smith, P., van der Velde, M., Vicca, S., Babst, F., Beer, C., Buchmann, N., Canadell, J.G., Ciais, P., Cramer, W., Ibrom, A., Miglietta, F., Poulter, B., Rammig, A., Seneviratne, S.I., Walz, A., Wattenbach, M., Zavala, M.A., & Zscheischler, J. (2015a). Effects of climate extremes on the terrestrial carbon cycle: concepts, processes and potential future impacts. *Glob Chang Biol, 21*, 2861-2880

Frank, D.C., Poulter, B., Saurer, M., Esper, J., Huntingford, C., Helle, G., Treydte, K., Zimmermann, N.E., Schleser, G.H., Ahlström, A., Ciais, P., Friedlingstein, P., Levis, S., Lomas, M., Sitch, S., Viovy, N., Andreu-Hayles, L., Bednarz, Z., Berninger, F., Boettger, T., D'Alessandro, C.M., Daux, V., Filot, M., Grabner, M., Gutierrez, E., Haupt, M., Hilasvuori, E., Jungner, H., Kalela-Brundin, M., Krapiec, M., Leuenberger, M., Loader, N.J., Marah, H., Masson-Delmotte, V., Pazdur, A., Pawelczyk, S., Pierre, M., Planells, O., Pukiene, R., Reynolds-Henne, C.E., Rinne, K.T., Saracino, A., Sonninen, E., Stievenard, M., Switsur, V.R., Szczepanek, M., Szychowska-Krapiec, E., Todaro, L., Waterhouse, J.S., & Weigl, M. (2015b). Water-use efficiency and transpiration across European forests during the Anthropocene. *Nature Climate Change, 5*, 579-583

Frankenberg, C., Fisher, J.B., Worden, J., Badgley, G., Saatchi, S.S., Lee, J.-E., Toon, G.C., Butz, A., Jung, M., Kuze, A., & Yokota, T. (2011). New global observations of the terrestrial carbon cycle from GOSAT: Patterns of plant fluorescence with gross primary productivity. *Geophysical Research Letters, 38*, L17706

Friedl, M., & Sulla-Menashe, D. (2015). MCD12C1 MODIS/Terra+Aqua Land Cover Type Yearly L3 Global 0.05Deg CMG V006 [Data set]. In: NASA EOSDIS Land Processes DAAC

Harris, I., Jones, P.D., Osborn, T.J., & Lister, D.H. (2014). Updated high-resolution grids of monthly climatic observations - the CRU TS3.10 Dataset. *International Journal of Climatology, 34*, 623-642

Hoover, D.L., Knapp, A.K., & Smith, M.D. (2014). Resistance and resilience of a grassland ecosystem to climate extremes. *Ecology, 95*, 2646-2656

Hsu, J.S., & Adler, P.B. (2014). Anticipating changes in variability of grassland production due to increases in interannual precipitation variability. *Ecosphere, 5*, 1-15

Hsu, J.S., Powell, J., & Adler, P.B. (2012). Sensitivity of mean annual primary production to precipitation. *Global Change Biology, 18*, 2246-2255

Hu, Z., Yu, G., Fu, Y., Sun, X., Li, Y., Shi, P., Wang, Y., & Zheng, Z. (2008). Effects of vegetation control on ecosystem water use efficiency within and among four grassland ecosystems in China. *Global Change Biology, 14*, 1609-1619

Huang, J., Yu, H., Guan, X., Wang, G., & Guo, R. (2015). Accelerated dryland expansion under climate change. *Nature Climate Change, 6*, 166

Huang, L., He, B., Chen, A., Wang, H., Liu, J., Lu, A., & Chen, Z. (2016). Drought dominates the interannual variability in global terrestrial net primary production by controlling semi-arid ecosystems. *Sci Rep, 6*, 24639

Huxman, T.E., Smith, M.D., & Fay, P.A. (2004). Convergence across biomes to a common rain-use efficiency. *Nature, 429*, 651-654

Ionita, M., Tallaksen, L.M., Kingston, D.G., Stagge, J.H., Laaha, G., Van Lanen, H.A.J., Scholz, P., Chelcea, S.M., & Haslinger, K. (2017). The European 2015 drought from a climatological perspective. *Hydrology and Earth System Sciences, 21*, 1397-1419

Jentsch, A., Kreyling, J., Elmer, M., Gellesch, E., Glaser, B., Grant, K., Hein, R., Lara, M., Mirzae, H., Nadler, S.E., Nagy, L., Otieno, D., Pritsch, K., Rascher, U., Schädler, M., Schloter, M., Singh, B.K., Stadler, J., Walter, J., Wellstein, C., Wöllecke, J., & Beierkuhnlein, C. (2011). Climate extremes initiate ecosystem-regulating functions while maintaining productivity. *Journal of Ecology, 99*, 689-702

Jiang, C., & Ryu, Y. (2016). Multi-scale evaluation of global gross primary productivity and evapotranspiration products derived from Breathing Earth System Simulator (BESS). *Remote Sensing of Environment, 186*, 528-547

Joiner, J., Guanter, L., Lindstrot, R., Voigt, M., Vasilkov, A.P., Middleton, E.M., Huemmrich, K.F., Yoshida, Y., & Frankenberg, C. (2013). Global monitoring of terrestrial chlorophyll fluorescence from moderate-spectral-resolution near-infrared satellite measurements: methodology, simulations, and application to GOME-2. *Atmospheric Measurement Techniques, 6*, 2803-2823

Joiner, J., Yoshida, Y., Vasilkov, A.P., Schaefer, K., Jung, M., Guanter, L., Zhang, Y., Garrity, S., Middleton, E.M., Huemmrich, K.F., Gu, L., & Belelli Marchesini, L. (2014). The seasonal cycle of satellite chlorophyll fluorescence observations and its relationship to vegetation phenology and ecosystem atmosphere carbon exchange. *Remote Sensing of Environment, 152*, 375-391

Jung, M., Reichstein, M., Margolis, H.A., Cescatti, A., Richardson, A.D., Arain, M.A., Arneth, A., Bernhofer, C., Bonal, D., Chen, J., Gianelle, D., Gobron, N., Kiely, G., Kutsch, W., Lasslop, G., Law, B.E., Lindroth, A., Merbold, L., Montagnani, L., Moors, E.J., Papale, D., Sottocornola, M., Vaccari, F., & Williams, C. (2011). Global patterns of land-atmosphere fluxes of carbon dioxide, latent heat, and sensible heat derived from eddy covariance, satellite, and meteorological observations. *Journal of Geophysical Research, 116*, G00J07

Jung, M., Reichstein, M., Schwalm, C.R., Huntingford, C., Sitch, S., Ahlstrom, A., Arneth, A., Camps-Valls, G., Ciais, P., Friedlingstein, P., Gans, F., Ichii, K., Jain, A.K., Kato, E., Papale, D., Poulter, B., Raduly, B., Rodenbeck, C., Tramontana, G., Viovy, N., Wang, Y.P., Weber, U., Zaehle, S., & Zeng, N. (2017). Compensatory water effects link yearly global land CO2 sink changes to temperature. *Nature, 541*, 516-520

Keenan, T.F., Hollinger, D.Y., Bohrer, G., Dragoni, D., Munger, J.W., Schmid, H.P., & Richardson, A.D. (2013). Increase in forest water-use efficiency as atmospheric carbon dioxide concentrations rise. *Nature, 499*, 324-327

Keenan, T.F., Prentice, I.C., Canadell, J.G., Williams, C.A., Wang, H., Raupach, M., & Collatz, G.J. (2016). Recent pause in the growth rate of atmospheric CO2 due to enhanced terrestrial carbon uptake. *Nat Commun, 7*, 13428

Knapp, A.K., Ciais, P., & Smith, M.D. (2017). Reconciling inconsistencies in precipitation-productivity relationships: implications for climate change. *New Phytologist, 214*, 41-47

Knauer, J., Zaehle, S., Reichstein, M., Medlyn, B.E., Forkel, M., Hagemann, S., & Werner, C. (2017). The response of ecosystem water-use efficiency to rising atmospheric CO2 concentrations: sensitivity and large-scale biogeochemical implications. *New Phytologist, 213*, 1654-1666

Kumar, J., Hoffman, F.M., Hargrove, W.W., & Collier, N. (2016). Understanding the representativeness of FLUXNET for upscaling carbon flux from eddy covariance measurements. *Earth System Science Data Discussions*, 1-25

Law, B.E., Falge, E., Gu, L., Baldocchi, D.D., Bakwin, P., Berbigier, P., Davis, K., Dolman, A.J., Falk, M., Fuentes, J.D., Goldstein, A., Granier, A., Grelle, A., Hollinger, D., Janssens, I.A., Jarvis, P., Jensen, N.O., Katul, G., Mahli, Y., Matteucci, G., Meyers, T., Monson, R., Munger, W., Oechel, W., Olson, R., Pilegaard, K., Paw, K.T., Thorgeirsson, H., Valentini, R., Verma, S., Vesala, T., Wilson, K., & Wofsy, S. (2002). Environmental controls over carbon dioxide and water vapor exchange of terrestrial vegetation. *Agricultural and Forest Meteorology, 113*, 97-120

Le Quéré, C., Moriarty, R., Andrew, R.M., Canadell, J.G., Sitch, S., Korsbakken, J.I., Friedlingstein, P., Peters, G.P., Andres, R.J., Boden, T.A., Houghton, R.A., House, J.I., Keeling, R.F., Tans, P., Arneth, A., Bakker, D.C.E., Barbero, L., Bopp, L., Chang, J., Chevallier, F., Chini, L.P., Ciais, P., Fader, M., Feely, R.A., Gkritzalis, T., Harris, I., Hauck, J., Ilyina, T., Jain, A.K., Kato, E., Kitidis, V., Klein Goldewijk, K., Koven, C., Landschützer, P., Lauvset, S.K., Lefèvre, N., Lenton, A., Lima, I.D., Metzl, N., Millero,

F., Munro, D.R., Murata, A., Nabel, J.E.M.S., Nakaoka, S., Nojiri, Y., O'Brien, K., Olsen, A., Ono, T., Pérez, F.F., Pfeil, B., Pierrot, D., Poulter, B., Rehder, G., Rödenbeck, C., Saito, S., Schuster, U., Schwinger, J., Séférian, R., Steinhoff, T., Stocker, B.D., Sutton, A.J., Takahashi, T., Tilbrook, B., van der Laan-Luijkx, I.T., van der Werf, G.R., van Heuven, S., Vandemark, D., Viovy, N., Wiltshire, A., Zaehle, S., & Zeng, N. (2015). Global Carbon Budget 2015. *Earth System Science Data, 7*, 349-396

Li, X., Gentine, P., Lin, C., Zhou, S., Sun, Z., Zheng, Y., Liu, J., & Zheng, C. (2019). A simple and objective method to partition evapotranspiration into transpiration and evaporation at eddy-covariance sites. *Agricultural and Forest Meteorology, 265*, 171-182

Liu, G., Liu, H., & Yin, Y. (2013). Global patterns of NDVI-indicated vegetation extremes and their sensitivity to climate extremes. *Environmental Research Letters, 8*, 025009

Liu, Y., Zhou, Y., Ju, W., Wang, S., Wu, X., He, M., & Zhu, G. (2014). Impacts of droughts on carbon sequestration by China's terrestrial ecosystems from 2000 to 2011. *Biogeosciences, 11*, 2583-2599

Lloyd, J.G.D.F., G. D. (1994). 3C discrimination during CO2 assimilation by the terrestrial biosphere, *99*, 201-215

Luo, Y.Q., Jiang, L.F., Niu, S.L., & Zhou, X.H. (2017). Nonlinear responses of land ecosystems to variation in precipitation. *New Phytologist, 214*, 5-7

Ma, J., Xiao, X., Zhang, Y., Doughty, R., Chen, B., & Zhao, B. (2018). Spatial-temporal consistency between gross primary productivity and solar-induced chlorophyll fluorescence of vegetation in China during 2007-2014. *Sci Total Environ, 639*, 1241-1253

Mack, M.C., Bret-Harte, M.S., Hollingsworth, T.N., Jandt, R.R., Schuur, E.A.G., Shaver, G.R., & Verbyla, D.L. (2011). Carbon loss from an unprecedented Arctic tundra wildfire. *Nature, 475*, 489-492

Mariotte, P., Vandenberghe, C., Kardol, P., Hagedorn, F., Buttler, A., & Schwinning, S. (2013). Subordinate plant species enhance community resistance against drought in semi-natural grasslands. *Journal of Ecology, 101*, 763-773

Martens, B., Miralles, D.G., Lievens, H., van der Schalie, R., de Jeu, R.A.M., Fernández-Prieto, D., Beck, H.E., Dorigo, W.A., & Verhoest, N.E.C. (2017). GLEAM v3: satellite-based land evaporation and root-zone soil moisture. *Geoscientific Model Development, 10*, 1903-1925

Martens, H., & Næs, T. (1989). *Muitivariate Calibration*. New York: Chichester: Wiley

Mazdiyasni, O., & AghaKouchak, A. (2015). Substantial increase in concurrent droughts and heatwaves in the United States. *Proc Natl Acad Sci U S A, 112*, 11484-11489

McDowell, N., Pockman, W.T., Allen, C.D., Breshears, D.D., Cobb, N., Kolb, T., Plaut, J., Sperry, J., West, A., Williams, D.G., & Yepez, E.A. (2008). Mechanisms of plant survival and mortality during drought: why do some plants survive while others succumb to drought? *New Phytologist, 178*, 719-739

Medlyn, B.E., De Kauwe, M.G., Lin, Y.S., Knauer, J., Duursma, R.A., Williams, C.A., Arneth, A., Clement, R., Isaac, P., Limousin, J.M., Linderson, M.L., Meir, P., Martin-StPaul, N., & Wingate, L. (2017). How do leaf and ecosystem measures of water-use efficiency compare? *New Phytologist, 216*, 758-770

Medlyn, B.E., Duursma, R.A., Eamus, D., Ellsworth, D.S., Prentice, I.C., Barton, C.V.M., Crous, K.Y., De Angelis, P., Freeman, M., & Wingate, L. (2011). Reconciling the optimal and empirical approaches to modelling stomatal conductance. *Global Change Biology, 17*, 2134-2144

Meyer, W.S. (2018). Increasing water productivity in agriculture: an overview, 497-519

Michaelian, M., Hogg, E.H., Hall, R.J., & Arsenault, E. (2011). Massive mortality of aspen following severe drought along the southern edge of the Canadian boreal forest. *Global Change Biology, 17*, 2084-2094

Miralles, D.G., Holmes, T.R.H., De Jeu, R.A.M., Gash, J.H., Meesters, A.G.C.A., & Dolman, A.J. (2011). Global land-surface evaporation estimated from satellite-based observations. *Hydrology and Earth System Sciences, 15*, 453-469

Mu, Q., Zhao, M., & Running, S.W. (2011). Improvements to a MODIS global terrestrial evapotranspiration algorithm. *Remote Sensing of Environment, 115*, 1781-1800

Myneni, R., Knyazikhin, Y., & Park, T. (2015). MOD15A2H MODIS/Terra Leaf Area Index/FPAR 8-Day L4 Global 500m SIN Grid V006 [Data set]. In: NASA EOSDIS Land Processes DAAC

Niu, S., Xing, X., Zhang, Z.H.E., Xia, J., Zhou, X., Song, B., Li, L., & Wan, S. (2011). Water-use efficiency in response to climate change: from leaf to ecosystem in a temperate steppe. *Global Change Biology, 17*, 1073-1082

Oki, T., & Kanae, S. (2006). Global hydrological cycles and world water resources. *Science, 313*, 1068-1072

Paruelo, J.M., Lauenroth, W.K., Burke, I.C., & Sala, O.E. (1999). Grassland precipitation-use efficiency varies across a resource gradient. *Ecosystems, 2*, 64-68

Peng, C.H., Ma, Z.H., Lei, X.D., Zhu, Q., Chen, H., Wang, W.F., Liu, S.R., Li, W.Z., Fang, X.Q., & Zhou, X.L. (2011). A drought-induced pervasive increase in tree mortality across Canada's boreal forests. *Nature Climate Change, 1*, 467-471

Peters, W., van der Velde, I.R., van Schaik, E., Miller, J.B., Ciais, P., Duarte, H.F., van der Laan-Luijkx, I.T., van der Molen, M.K., Scholze, M., Schaefer, K., Vidale, P.L., Verhoef, A., Warlind, D., Zhu, D., Tans, P.P., Vaughn, B., & White, J.W.C. (2018). Increased water-use efficiency and reduced CO2 uptake by plants during droughts at a continental-scale. *Nat Geosci, 11*, 744-748

Piao, S., Sitch, S., Ciais, P., Friedlingstein, P., Peylin, P., Wang, X., Ahlström, A., Anav, A., Canadell, J.G., Cong, N., Huntingford, C., Jung, M., Levis, S., Levy, P.E., Li, J., Lin, X., Lomas, M.R., Lu, M., Luo, Y., Ma, Y., Myneni, R.B., Poulter, B., Sun, Z., Wang, T., Viovy, N., Zaehle, S., & Zeng, N. (2013). Evaluation of terrestrial carbon cycle models for their response to climate variability and to CO2trends. *Global Change Biology, 19*, 2117-2132

Ponce Campos, G.E., Moran, M.S., Huete, A., Zhang, Y., Bresloff, C., Huxman, T.E., Eamus, D., Bosch, D.D., Buda, A.R., Gunter, S.A., Scalley, T.H., Kitchen, S.G., McClaran, M.P., McNab, W.H., Montoya, D.S., Morgan, J.A., Peters, D.P., Sadler, E.J., Seyfried, M.S., & Starks, P.J. (2013). Ecosystem resilience despite large-scale altered hydroclimatic conditions. *Nature, 494*, 349-352

Reichstein, M., Bahn, M., Ciais, P., Frank, D., Mahecha, M.D., Seneviratne, S.I., Zscheischler, J., Beer, C., Buchmann, N., Frank, D.C., Papale, D., Rammig, A., Smith, P., Thonicke, K., van der Velde, M., Vicca, S., Walz, A., & Wattenbach, M. (2013). Climate extremes and the carbon cycle. *Nature, 500*, 287-295

Reyer, C.P., Leuzinger, S., Rammig, A., Wolf, A., Bartholomeus, R.P., Bonfante, A., de Lorenzi, F., Dury, M., Gloning, P., Abou Jaoude, R., Klein, T., Kuster, T.M., Martins, M., Niedrist, G., Riccardi, M., Wohlfahrt, G., de Angelis, P., de Dato, G., Francois, L., Menzel, A., & Pereira, M. (2013). A plant's perspective of extremes: terrestrial plant responses to changing climatic variability. *Glob Chang Biol, 19*, 75-89

Running, S., Mu, Q., & Zhao, M. (2017). MOD16A2 MODIS/Terra Net Evapotranspiration 8-Day L4 Global 500m SIN Grid V006 [Data set]. In: NASA EOSDIS Land Processes DAAC

Schneider, U., Becker, A., Finger, P., Meyer-Christoffer, A., Ziese, M., & Rudolf, B. (2013). GPCC's new land surface precipitation climatology based on quality-controlled in situ data and its role in quantifying the global water cycle. *Theoretical and Applied Climatology, 115*, 15-40

Schwalm, C.R., Williams, C.A., Schaefer, K., Baldocchi, D., Black, T.A., Goldstein, A.H., Law, B.E., Oechel, W.C., Paw U, K.T., & Scott, R.L. (2012). Reduction in carbon uptake during turn of the century drought in western North America. *Nature Geoscience, 5*, 551-556

Seddon, A.W.R., Macias-Fauria, M., Long, P.R., Benz, D., & Willis, K.J. (2016). Sensitivity of global terrestrial ecosystems to climate variability. *Nature, 531*, 229-232

Serneels, S., Croux, C., Filzmoser, P., & Van Espen, P.J. (2005). Partial robust M-regression. *Chemometrics and Intelligent Laboratory Systems, 79*, 55-64

Sitch, S., Huntingford, C., Gedney, N., Levy, P.E., Lomas, M., Piao, S.L., Betts, R., Ciais, P., Cox, P., Friedlingstein, P., Jones, C.D., Prentice, I.C., & Woodward, F.I. (2008). Evaluation of the terrestrial carbon cycle, future plant geography and climate-carbon cycle feedbacks using five Dynamic Global Vegetation Models (DGVMs). *Global Change Biology, 14*, 2015-2039

Smith, M.D. (2011). An ecological perspective on extreme climatic events: a synthetic definition and framework to guide future research. *Journal of Ecology, 99*, 656-663

Stocker, T.F., Qin, D., Plattner, G., Tignor, M., Allen, S., Boschung, J., Nauels, A., Xia, Y., Bex, V., & Midgley, P. (2013). Climate change 2013: the physical science basis. Intergovernmental panel on climate change, working group I contribution to the IPCC fifth assessment report (AR5). In. New York

Sun, G., Alstad, K., Chen, J., Chen, S., Ford, C.R., Lin, G., Liu, C., Lu, N., McNulty, S.G., Miao, H., Noormets, A., Vose, J.M., Wilske, B., Zeppel, M., Zhang, Y., & Zhang, Z. (2011a). A general predictive model for estimating monthly ecosystem evapotranspiration. *Ecohydrology, 4*, 245-255

Sun, G., Caldwell, P., Noormets, A., McNulty, S.G., Cohen, E., Moore Myers, J., Domec, J.-C., Treasure, E., Mu, Q., Xiao, J., John, R., & Chen, J. (2011b). Upscaling key ecosystem functions across the conterminous United States by a water-centric ecosystem model. *Journal of Geophysical Research, 116*, G00J05

Sun, Y., Frankenberg, C., Jung, M., Joiner, J., Guanter, L., Köhler, P., & Magney, T. (2018). Overview of Solar-Induced chlorophyll Fluorescence (SIF) from the Orbiting Carbon Observatory-2: Retrieval, cross-mission comparison, and global monitoring for GPP. *Remote Sensing of Environment, 209*, 808-823

Sun, Y., Frankenberg, C., Wood, J.D., Schimel, D.S., Jung, M., Guanter, L., Drewry, D.T., Verma, M., Porcar-Castell, A., Griffis, T.J., Gu, L., Magney, T.S., Kohler, P., Evans, B., & Yuen, K. (2017). OCO-2 advances photosynthesis observation from space via solar-induced chlorophyll fluorescence. *Science, 358*, eaam5747

Sun, Y., Piao, S., Huang, M., Ciais, P., Zeng, Z., Cheng, L., Li, X., Zhang, X., Mao, J., Peng, S., Poulter, B., Shi, X., Wang, X., Wang, Y.-P., & Zeng, H. (2016). Global patterns and climate drivers of water-use efficiency in terrestrial ecosystems deduced from satellite-based datasets and carbon cycle models. *Global Ecology and Biogeography, 25*, 311-323

Tadesse, T., Wardlow, B.D., Brown, J.F., Svoboda, M.D., Hayes, M.J., Fuchs, B., & Gutzmer, D. (2015). Assessing the Vegetation Condition Impacts of the 2011 Drought across the U.S. Southern Great Plains Using the Vegetation Drought Response Index (VegDRI). *Journal of Applied Meteorology and Climatology, 54*, 153-169

Tang, X., Li, H., Desai, A.R., Nagy, Z., Luo, J., Kolb, T.E., Olioso, A., Xu, X., Yao, L., Kutsch, W., Pilegaard, K., Köstner, B., & Ammann, C. (2014). How is water-use efficiency of terrestrial ecosystems distributed and changing on Earth? *Scientific Reports, 4*, 7483

Turetsky, M.R., Benscoter, B., Page, S., Rein, G., van der Werf, G.R., & Watts, A. (2014). Global vulnerability of peatlands to fire and carbon loss. *Nature Geoscience, 8*, 11-14

van der Sleen, P., Groenendijk, P., Vlam, M., Anten, N.P.R., Boom, A., Bongers, F., Pons, T.L., Terburg, G., & Zuidema, P.A. (2014). No growth stimulation of tropical trees by 150 years of CO2 fertilization but water-use efficiency increased. *Nature Geoscience, 8*, 24-28

Verbesselt, J., Umlauf, N., Hirota, M., Holmgren, M., Van Nes, E.H., Herold, M., Zeileis, A., & Scheffer, M. (2016). Remotely sensed resilience of tropical forests. *Nature Climate Change, 6*, 1028-1031

Veron, S.R., Oesterheld, M., & Paruelo, J.M. (2005). Production as a function of resource availability: Slopes and efficiencies are different. *Journal of Vegetation Science, 16*, 351-354

Wang, L., Good, S.P., & Caylor, K.K. (2014). Global synthesis of vegetation control on evapotranspiration partitioning. *Geophysical Research Letters, 41*, 6753-6757

Wang, M., Chen, Y., Wu, X., & Bai, Y. (2018). Forest-Type-Dependent Water Use Efficiency Trends Across the Northern Hemisphere. *Geophysical Research Letters, 45*, 8283-8293

Wei, Z.W., Yoshimura, K., Wang, L.X., Miralles, D.G., Jasechko, S., & Lee, X.H. (2017). Revisiting the contribution of transpiration to global terrestrial evapotranspiration. *Geophysical Research Letters, 44*, 2792-2801

Wilcox, K.R., Shi, Z., Gherardi, L.A., Lemoine, N.P., Koerner, S.E., Hoover, D.L., Bork, E., Byrne, K.M., Cahill, J., Jr., Collins, S.L., Evans, S., Gilgen, A.K., Holub, P., Jiang, L., Knapp, A.K., LeCain, D., Liang, J., Garcia-Palacios, P., Penuelas, J., Pockman, W.T., Smith, M.D., Sun, S., White, S.R., Yahdjian, L., Zhu, K., & Luo, Y. (2017). Asymmetric responses of primary productivity to precipitation extremes: A synthesis of grassland precipitation manipulation experiments. *Glob Chang Biol, 23*, 4376-4385

Wu, D., Zhao, X., Liang, S., Zhou, T., Huang, K., Tang, B., & Zhao, W. (2015). Time-lag effects of global vegetation responses to climate change. *Glob Chang Biol, 21*, 3520-3531

Wu, Z., Ahlstroem, A., Smith, B., Ardo, J., Eklundh, L., Fensholt, R., & Lehsten, V. (2017). Climate data induced uncertainty in model based estimations of terrestrial primary productivity. *Environmental Research Letters, 12*, 064013

Xiao, X.M., Hollinger, D., Aber, J., Goltz, M., Davidson, E.A., Zhang, Q.Y., & Moore, B. (2004). Satellite-based modeling of gross primary production in an evergreen needleleaf forest. *Remote Sensing of Environment, 89*, 519-534

Xiao, X.M., Zhang, Q.Y., Hollinger, D., Aber, J., & Moore, B. (2005). Modeling gross primary production of an evergreen needleleaf forest using modis and climate data. *Ecological Applications, 15*, 954-969

Yan, K., Park, T., Yan, G., Liu, Z., Yang, B., Chen, C., Nemani, R., Knyazikhin, Y., & Myneni, R. (2016). Evaluation of MODIS LAI/FPAR Product Collection 6. Part 2: Validation and Intercomparison. *Remote Sensing, 8*, 460

Yan, L., Luo, Y., Sherry, R.A., Bell, J.E., Zhou, X., & Xia, J. (2014). Rain use efficiency as affected by climate warming and biofuel harvest: results from a 12-year field experiment. *GCB Bioenergy, 6*, 556-565

Yang, K., Ryu, Y., Dechant, B., Berry, J.A., Hwang, Y., Jiang, C., Kang, M., Kim, J., Kimm, H., Kornfeld, A., & Yang, X. (2018). Sun-induced chlorophyll fluorescence is more strongly related to absorbed light than to photosynthesis at half-hourly resolution in a rice paddy. *Remote Sensing of Environment, 216*, 658-673

Yang, X., Tang, J.W., Mustard, J.F., Lee, J.E., Rossini, M., Joiner, J., Munger, J.W., Kornfeld, A., & Richardson, A.D. (2015). Solar-induced chlorophyll fluorescence that correlates with canopy photosynthesis on diurnal and seasonal scales in a temperate deciduous forest. *Geophysical Research Letters, 42*, 2977-2987

Yang, Y., Guan, H., Batelaan, O., McVicar, T.R., Long, D., Piao, S., Liang, W., Liu, B., Jin, Z., & Simmons, C.T. (2016). Contrasting responses of water use efficiency to drought across global terrestrial ecosystems. *Sci Rep, 6*, 23284

Yang, Y.H., Fang, J.Y., Fay, P.A., Bell, J.E., & Ji, C.J. (2010). Rain use efficiency across a precipitation gradient on the Tibetan Plateau. *Geophysical Research Letters, 37*, L15702

Yu, Z., Wang, J., Liu, S., Rentch, J.S., Sun, P., & Lu, C. (2017). Global gross primary productivity and water use efficiency changes under drought stress. *Environmental Research Letters, 12*, 014016

Zeng, Z., Piao, S., Lin, X., Yin, G., Peng, S., Ciais, P., & Myneni, R.B. (2012). Global evapotranspiration over the past three decades: estimation based on the water balance equation combined with empirical models. *Environmental Research Letters, 7*, 014026

Zhang, K., Kimball, J.S., & Running, S.W. (2016a). A review of remote sensing based actual evapotranspiration estimation. *Wiley Interdisciplinary Reviews: Water, 3*, 834-853

Zhang, T., Niinemets, U., Sheffield, J., & Lichstein, J.W. (2018a). Shifts in tree functional composition amplify the response of forest biomass to climate. *Nature, 556*, 99-102

Zhang, Y., Joiner, J., Alemohammad, S.H., Zhou, S., & Gentine, P. (2018b). A global spatially Continuous Solar Induced Fluorescence (CSIF) dataset using neural networks. *Biogeosciences Discussions, 15*, 5779-5800

Zhang, Y., Joiner, J., Gentine, P., & Zhou, S. (2018c). Reduced solar-induced chlorophyll fluorescence from GOME-2 during Amazon drought caused by dataset artifacts. *Glob Chang Biol, 24*, 2229-2230

Zhang, Y., Song, C., Sun, G., Band, L.E., McNulty, S., Noormets, A., Zhang, Q., & Zhang, Z. (2016b). Development of a coupled carbon and water model for estimating global gross primary productivity and evapotranspiration based on eddy flux and remote sensing data. *Agricultural and Forest Meteorology, 223*, 116-131

Zhang, Y., Xiao, X., Guanter, L., Zhou, S., Ciais, P., Joiner, J., Sitch, S., Wu, X., Nabel, J., Dong, J., Kato, E., Jain, A.K., Wiltshire, A., & Stocker, B.D. (2016c). Precipitation and carbon-water coupling jointly control the interannual variability of global land gross primary production. *Sci Rep, 6*, 39748

Zhang, Y., Xiao, X., Wu, X., Zhou, S., Zhang, G., Qin, Y., & Dong, J. (2017). A global moderate resolution dataset of gross primary production of vegetation for 2000-2016. *Sci Data, 4*, 170165

Zhao, M., & Running, S.W. (2010). Drought-induced reduction in global terrestrial net primary production from 2000 through 2009. *Science, 329*, 940-943

Zhongmin, H., Guirui, Y., Jiangwen, F., Huaping, Z., Shaoqiang, W., & Shenggong, L. (2010). Precipitation-use efficiency along a 4500-km grassland transect. *Global Ecology and Biogeography, 19*, 842-851

Zhou, S., Yu, B., Huang, Y., & Wang, G. (2014). The effect of vapor pressure deficit on water use efficiency at the subdaily time scale. *Geophysical Research Letters, 41*, 5005-5013

Zhou, S., Yu, B., Huang, Y., & Wang, G. (2015). Daily underlying water use efficiency for AmeriFlux sites. *Journal of Geophysical Research: Biogeosciences, 120*, 887-902

Zhou, S., Yu, B., Schwalm, C.R., Ciais, P., Zhang, Y., Fisher, J.B., Michalak, A.M., Wang, W., Poulter, B., Huntzinger, D.N., Niu, S., Mao, J., Jain, A., Ricciuto, D.M., Shi, X., Ito, A., Wei, Y., Huang, Y., & Wang, G. (2017). Response of water use efficiency to global environmental change based on output from terrestrial biosphere models. *Global Biogeochemical Cycles, 31*, 1639-1655

Zhou, S., Yu, B., Zhang, Y., Huang, Y., & Wang, G. (2016). Partitioning evapotranspiration based on the concept of underlying water use efficiency. *Water Resources Research, 52*, 1160-1175

Zhu, Z., Piao, S., Myneni, R.B., Huang, M., Zeng, Z., Canadell, J.G., Ciais, P., Sitch, S., Friedlingstein, P., Arneth, A., Cao, C., Cheng, L., Kato, E., Koven, C., Li, Y., Lian, X., Liu, Y., Liu, R., Mao, J., Pan, Y., Peng, S., Peñuelas, J., Poulter, B., Pugh, T.A.M., Stocker, B.D., Viovy, N., Wang, X., Wang, Y., Xiao, Z., Yang, H., Zaehle, S., & Zeng, N. (2016). Greening of the Earth and its drivers. *Nature Climate Change, 6*, 791-795

Zscheischler, J., Mahecha, M.D., von Buttlar, J., Harmeling, S., Jung, M., Rammig, A., Randerson, J.T., Schölkopf, B., Seneviratne, S.I., Tomelleri, E., Zaehle, S., & Reichstein, M. (2014). A few extreme events dominate global interannual variability in gross primary production. *Environmental Research Letters, 9*, 035001